

American University in Cairo

AUC Knowledge Fountain

Theses and Dissertations

Student Research

2-1-2014

Numerical study of film cooling influence on performance of transonic vane cascade

Ahmad M. Alameldin

Follow this and additional works at: <https://fount.aucegypt.edu/etds>

Recommended Citation

APA Citation

Alameldin, A. (2014). *Numerical study of film cooling influence on performance of transonic vane cascade* [Master's Thesis, the American University in Cairo]. AUC Knowledge Fountain.

<https://fount.aucegypt.edu/etds/1263>

MLA Citation

Alameldin, Ahmad M.. *Numerical study of film cooling influence on performance of transonic vane cascade*. 2014. American University in Cairo, Master's Thesis. *AUC Knowledge Fountain*.

<https://fount.aucegypt.edu/etds/1263>

This Master's Thesis is brought to you for free and open access by the Student Research at AUC Knowledge Fountain. It has been accepted for inclusion in Theses and Dissertations by an authorized administrator of AUC Knowledge Fountain. For more information, please contact thesisadmin@aucegypt.edu.



THE AMERICAN UNIVERSITY IN CAIRO
SCHOOL OF SCIENCES AND ENGINEERING

**NUMERICAL STUDY OF FILM COOLING INFLUENCE ON
PERFORMANCE OF TRANSONIC VANE CASCADE**

BY

Ahmad M. Alameldin

A thesis submitted in partial fulfillment of the requirements for the degree
of

Master of Science in Mechanical Engineering

Under the supervision of:

Dr. Lamyaa El-Gabry

Associate Professor, Department of Mechanical and Engineering

The American university in Cairo

January, 2014

To my parents, for their unconditional love and support...

Abstract

Gas turbines are a major contributor to world power generation with applications ranging from electricity production to aircrafts propulsion. Their efficiency is subject to continuous research. A gas turbine's overall efficiency is directly proportional to flow inlet temperature. Various methods are implemented to protect hot gas path components from mainstream flow well above their melting temperature, namely, heat resistant coatings, internal cooling and film cooling. The latter is the subject of this work. A 3-D Computational Fluid Dynamics (CFD) model is solved using ANSYS CFX software and compared to experimental measurements of film cooled transonic vane cascade operating at a Mach number of 0.89; the experimental data used for validation is provided by Heat and Power Technology Department of the Royal Institute of Technology (Kungliga Tekniska Högskolan, KTH) of Stockholm, Sweden.

A new approach was used to model the film cooling holes, omitting the need to model both the coolant plenum and cooling tubes, resulting in 180% reduction in grid size and attributed computational cost interpreted in 300% saving in computation time. The new approach was validated on a basic flow problem (flat plate film cooling) and was found to give good agreement with experimental measurements of velocity and temperature at a blowing ratio (BR) of 1 and 2; the experimental data for the flat plate was provided by NASA's Glenn Research Center. The numerical simulation of the cooled vane cascade was compared to experimental measurements for different cooling configurations and different BRs. a) One row on pressure side at BR = 0.8, 0.96 and 2.5. b) Two rows on suction side (location 1) at BR = 0.8, 1.4 and 2.5. c) Two rows on suction side (location 2) at BR = 0.8. And d) Showerhead cooled vane at BR ranges between 1.98 and 5.84. The coolant was applied at the same temperature as the mainstream, to match experimental conditions. A good agreement with the experimental measurements was obtained for exit flow angle, vorticity downstream of the vane, pressure coefficients and aerodynamic loss.

The proposed approach of coolant injection modeling is shown to yield reliable results, within the uncertainty of the measurements in most cases. Along with lower computational cost compared to conventional film cooling modeling approach, the new approach is recommended for further analysis for aero and thermal vane cascade flows.

Keywords

CFD, Gas turbines, annular sector cascade, turbine guide vanes, secondary flow losses, film cooling.

Preface

The following paper publications were derived from this thesis work:

- Ahmad Alameldin and L. El-Gabry, "CFD Analysis of Secondary Flow Losses in an Annular Sector Cascade", ICFD11-EG-4059, Eleventh International Conference of Fluid Dynamics, ICFD11.
- Ahmad Alameldin ,L. El-Gabry, Jens Fridh and Ranjan Saha, "CFD Analysis of Suction and Pressure Side Film Cooling Influence on Vane Aero Performance in a Transonic Annular Cascade", GT2014-26617, ASME Turbo Expo 2014 (draft paper accepted).
- Ahmad Alameldin, Karim M. Shalash and L. El-Gabry, "Assessment of Different Techniques of CFD Film Cooling Modeling", GT2014-26848, ASME Turbo Expo 2014 (draft paper accepted).

Acknowledgment

I would like to start by praising Allah, for his guiding hand has always pointed me in the right direction and lead me through times of uncertainty, query and ambiguity.

Then my sincerest thanks are for my supervisor, Dr. Lamyaa El-Gabry, for the continuous guidance and support she provided throughout the time of this work. Her intellect and erudition make her one of the most versed professors I have met in my educational life, which was interpreted in clearer and paved path for me in my work.

And thanks to Dr. Jens Fridh and Ranjan Saha of the Energy department at KTH Royal Institute of Technology who made this research possible through providing data and guidance. And the very informative and enlightening online meetings we had. Also I would like to thank Siemens AG for gracefully agreeing on disclosure of data in this work.

Also, special thanks to my colleagues at Optumatics. Amr Sami, Karim Shalash, Mohammad Bahaa-Eldin, Alaa' Khalaf and Karim Shehata, the conversations we had were always fruitful and enriching. Hossam Samir, your help with ANSYS ICEM software has saved me precious time and effort.

And last but not least, my sincerest gratitude is for Dr. Sherif El-Tahry, Optumatics COO, for his understanding and patience through critical times of this work and for motivating and inspiring me in ways no one else could.

Nomenclature

Symbols

c	Chord length [mm]
C_p	Total pressure coefficient [-]
C_μ	Closure coefficient
D	Diameter [mm]
h	Heat transfer coefficient [W/m^2K]
H	enthalpy
k	Turbulence kinetic energy [J/kg]
K	von Karman's constant ($K = 0.41$)
L	Length
L_i	Leonard stress tensor
\dot{m}	Mass flow rate [kg/s]
M	Mach number [-]
P	Pressure [kPa]
P_k	Rate of turbulent kinetic energy production
q''	Heat transfer rate [W/m^2]
r	Radius [mm]
Re	Reynolds number [-]
s	Pitch [mm]
S_{ij}	Mean strain-rate tensor
T	Temperature [K]
t_{ij}	Viscous stress tensor
u	Velocity in x-direction
U	Velocity [m/s]
u_τ	Shear (friction) velocity
v	Velocity in y-direction
w	Velocity in z-direction

x, y, z	Axial, pitchwise and spanwise distance respectively [mm]
y	Cooling hole spacing
Y	Mass flux ratio [%]
y^+	Normalized wall distance
α	Tangential flow angle or yaw angle [°]
β	Turbulence model constant
β^*	Turbulence model constant
γ_2	Turbulence model constant
δ_{ij}	Kronecker delta ($\delta_{ij} = 1$ if $i = j$ and $\delta_{ij} = 0$ if $i \neq j$)
μ_t	Eddy viscosity
σ_k	Total stress tensor
ω_x	Vorticity [1/s]
\emptyset	Fuel equivalence ratio [-]
Δ	Difference [-]
ε	Rate of viscous dissipation [m^2/s^2]
ζ	Energy loss coefficient [-]
η	Film cooling effectiveness [-]
θ	Normalized temperature [-]
κ	Specific heat ratio [-]
μ	Viscosity
ρ	Density [kg/m^3]
ω	Specific turbulence energy dissipation [m^2/s^2]
Γ	Diffusivity

Subscripts

1	Upstream Plane Position
2	Downstream Plane Position
3	Downstream Hub Static Pressure Tap Plane Position
ave	Average

ax	Axial Reference
c	Coolant
exit	Exit
f	Film cooling
g	Coolant and mainstream mix
hi	High
hub	Hub
in	Inlet
iso	Isentropic
low	Low
m	Mainstream
max	Maximum
mid	Midspan
nom	Nominal
pr	Primary
s	Static
w	Wall
i, j, k	x, y and z-components
∞	Mainstream

Abbreviations

ASC	Annular Sector Cascade
atm	Atmospheric
BC	Boundary Condition
BR	Blowing Ratio
CAD	Computer Aided Design
CFD	Computational Fluid Dynamics
CV	Corner Vortex
grad	Gradient

HPT	High Pressure Turbine
HS	Horseshoe vortex
KE	Kinetic Energy
KTH	Kungliga Tekniska Högskolan, Royal Institute of Technology (in Swedish)
LE	Leading Edge
MS	Mainstream
MW	Mega Watt
NGV	Nozzle Guide Vane
PS	Pressure Side
PV	Passage Vortex
SH	Showerhead
SS	Suction Side
SST	Shear Stress Transport
TE	Trailing Edge

Contents

Abstract	iii
Nomenclature.....	vii
1. Introduction.....	1
1.1. Gas turbines.....	1
1.2. Flow in vane cascades	4
1.3. Film cooling.....	8
1.3.1. Experimental investigation of film cooling in literature	8
1.3.2. Numerical investigation of film cooling in literature.....	11
2. Research motivation and outline	14
3. Research methodology.....	15
3.1. Experimental benchmark	15
3.1.1. Annular Sector Cascade (ASC)	15
3.1.2. Flat plate film cooling	19
3.2. Numerical analysis.....	21
3.2.1. Introduction to CFX	21
3.2.2. Governing equations	21
3.2.3. Numerical domain	24
4. Results and discussion.....	34
4.1. Uncooled vane.....	34
4.1.1. Inlet flow total pressure	34
4.1.2. Vane loading	35
4.1.3. Exit flow angle distribution.....	35
4.1.4. Vorticity and total pressure distribution	36
4.1.5. Aerodynamic loss	41
4.2. Flat plate film cooling	44
4.2.1. Normalized flow velocity.....	44
4.2.2. Flow field temperature along centerline.....	45
4.2.3. Film cooling effectiveness	48
4.3. Cooled vane.....	51
4.3.1. Configuration 1 (Pressure side and suction side).....	51
4.3.2. Configuration 2 (Showerhead)	59
5. Conclusion and future work	66
Appendices	67
Bibliography.....	68

Index of figures

Figure 1-1 Siemens SGT-700 gas turbine (courtesy of Siemens).....	1
Figure 1-2 Turbine performance map (Boyce 2001)	1
Figure 1-3 Adiabatic flame temperature of various fuels (Law et al. 2006).....	2
Figure 1-4 a) Horseshow vortex formation around a cylinder (Eckerle 1985), b) Leading edge- Endwall separation (Mahmood et al. 2005)	4
Figure 1-5 Flow in a cascade passage (Klein 1966).....	5
Figure 1-6 Secondary flow formation in linear cascade (Langston 1980)	5
Figure 1-7 Laminar flow evolution in low speed air flow as visualized by smoke (Sieverding and Bosche 1983)	6
Figure 1-8 Secondary flow model (Sharma and Butler 1987)	7
Figure 1-9 Static pressure distribution on airfoil surface (Langston et al. 1977)	7
Figure 1-10 Film cooled HPT (Hill and Peterson 1992).....	8
Figure 1-11 Film cooled HPT (Gritsch et al. 1998).....	8
Figure 1-12 Jet in a crossflow (Roshko and Fric 1994)	10
Figure 1-13 2-D view of numerical grid (Bohn and Kusterer 1999).....	12
Figure 1-14 Source terms representation of effusion cooling holes (Andreini et al. 2013)	13
Figure 3-1 ASC arrangement (Bartl 2010)	15
Figure 3-2 Fence (up) and parallel bar (down) turbulence grids (Saha 2012).....	16
Figure 3-3 NGVs test section cutaway (El- Gabry et al. 2012).....	16
Figure 3-4 NGVs test section (Saha et al. 2013)	17
Figure 3-5 NGV cross-section (Saha et al. 2013)	17
Figure 3-6 5-hole and 3-hole probes (Saha 2012)	18
Figure 3-7 Flat plate wind tunnel schematic drawing (El-Gabry et al. 2011)	19
Figure 3-8 Flat plate film cooling holes (El-Gabry et al. 2011)	20
Figure 3-9 Turbulent Boundary Layer.....	23
Figure 3-10 ICEM blocking strategy	24
Figure 3-11 NGV numerical domain	25
Figure 3-12 CFD grid for NGVs test section	25
Figure 3-13 Periodic vanes grid	26
Figure 3-14 Data extraction points (Saha et al. 2013).....	27
Figure 3-15 Total pressure at 107.1% Cax-hub and 50% span	28
Figure 3-16 CFD grid for single vane.....	28
Figure 3-17 Grid independence check.....	29
Figure 3-18 Flat plate with pipe CFD domain	30
Figure 3-19 CFD grid domain	30
Figure 3-20 Flat plate grid independence check	31
Figure 3-21 Film cooling hole new model	32
Figure 3-22 Cooling hole extrusion.....	32
Figure 3-23 Velocity at coolant hole exit.....	32
Figure 3-24 Normalized temperature for truncated case (up) and hole case (bottom)	33

Figure 4-1 CFD calculation of inlet boundary layer	34
Figure 4-2 M_{iso} at 50% span	35
Figure 4-3 Uncooled (Reference) vane exit flow angle	36
Figure 4-4 Ref. case vorticity at 107.1% $C_{ax, hub}$	37
Figure 4-5 Vortex formation and evolution in vane passage	38
Figure 4-6 Vortex structure at LE.....	39
Figure 4-7 Vortex upstream at casing	39
Figure 4-8 Total pressure coefficient.....	40
Figure 4-9 Normalized mass averaged kinetic energy loss at 107.1% $C_{ax, hub}$	41
Figure 4-10 Mass averaged static pressure trend line at 107.1% $C_{ax, hub}$	42
Figure 4-11 Flow development in vane passage (Povey et al. 2007)	43
Figure 4-12 u-velocity normalized contours (BR=1 and BR=2).....	44
Figure 4-13 Theta contours (BR=1 and BR=2)	46
Figure 4-14 Theta contours (BR=1).....	47
Figure 4-15 Mainstream entrainment in the coolant jet wake	47
Figure 4-16 Theta contours (BR=2).....	48
Figure 4-17 η at centerline downstream of the coolant hole (BR=1).....	49
Figure 4-18 η at centerline downstream of the coolant hole (BR=2).....	49
Figure 4-19 Normalized u-velocity downstream cooling hole	50
Figure 4-20 Film cooling holes locations (Saha et al. 2013)	51
Figure 4-21 Film cooling holes.....	52
Figure 4-22 Pitch-averaged exit flow angle (Experimental data from Saha et al. 2013).....	53
Figure 4-23 SS1 high BR case vorticity at 107.1% $C_{ax, hub}$ downstream	54
Figure 4-24 Total pressure distribution, SS1 Y_{high} case	55
Figure 4-25 Normalized reference primary loss, different cooled cases (Experimental data from Saha et al. 2013)	57
Figure 4-26 Normalized KE loss, different cooled cases (Experimental data from Saha et al. 2013)	58
Figure 4-27 Showerhead cooling locations	59
Figure 4-28 α for SH cooling at various Y, 107.1% $C_{ax, hub}$ (Experimental data from Saha et al. 2014)	60
Figure 4-29 Total pressure coefficient reference case, 107.1% $C_{ax, hub}$	61
Figure 4-30 Total pressure coefficient SH cooled case Y_{high} , 107.1% $C_{ax, hub}$	62
Figure 4-31 Vorticity at TE for SH cooled case at Y_{high}	63
Figure 4-32 Showerhead Y_{high} PS vortex structure	64
Figure 4-33 Showerhead Y_{high} SS vortex structure.....	64
Figure 4-34 Normalized ζ_{pr} for SH cooling at various Y, 107.1% $C_{ax, hub}$ (Experimental data from Saha et al. 2014)	65
Figure 4-35 Normalized ζ for SH cooling at various Y, 107.1% $C_{ax, hub}$ (Experimental data from Saha et al. 2014).....	65

1. Introduction

1.1. Gas turbines

With a contribution of 17% to the total global energy production (Saha 2012) and providing thrust for most modern aircrafts, At least 2504 jet engines were delivered in 2012¹, gas turbines' (Figure 1-1) efficiency improvement is an imperative demand for better use of critically limited fossil fuels supply. And lowering human footprint on an already burdened environmental system. Saha (2012) reports from Mamaev (2011) that a 1% increase in efficiency for a gas turbine of 50MW of power will yield fuel saving of 750 tons a year. In the strive for more efficient, less pollutant and more economical gas turbines, the understanding of efficiency limitations and sources of losses is a key parameter.

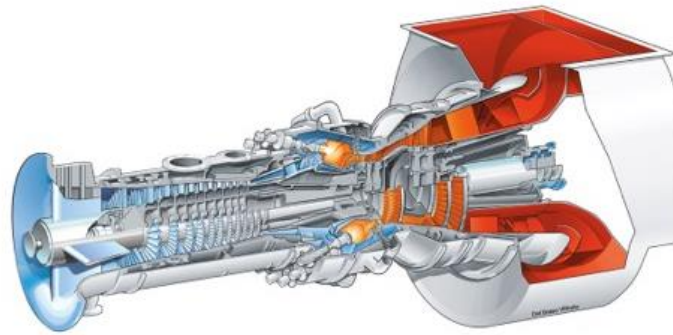


Figure 1-1 Siemens SGT-700 gas turbine (courtesy of Siemens)

An example of gas turbine performance map is shown in figure 1-2. And is shows clearly the dependency of efficiency on inlet gas temperature for a given flow rate.

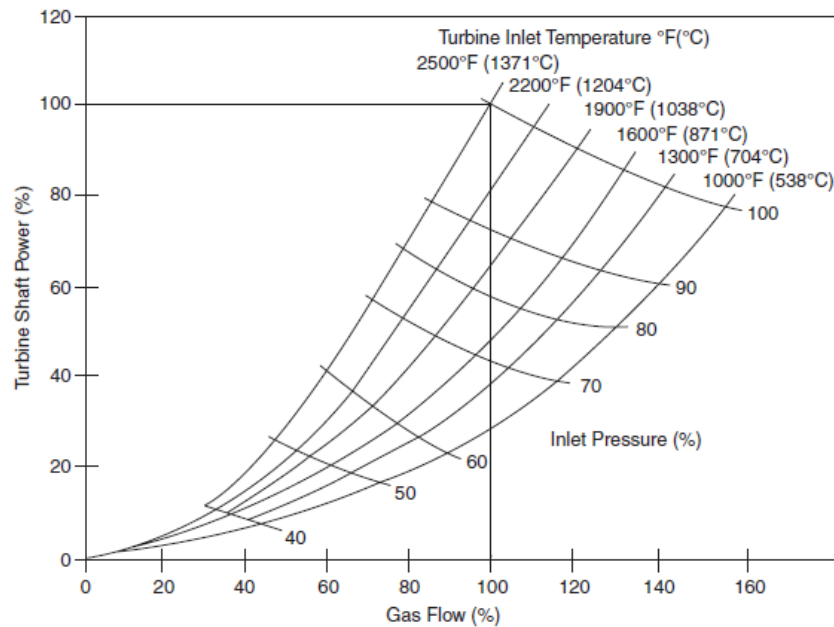


Figure 1-2 Turbine performance map (Boyce 2001)

¹ PwC Aerospace & defense report "2012 year in review and 2013 forecast"

While a high inlet temperature is appealing from a performance prospective, the life time of the turbine components is impacted negatively with application of such high temperatures. This applies specially to vanes. Vanes are the first component of a High Pressure Turbine (HPT), being closest to combustion chamber flue gas; it is the component subject to highest thermal loads, requiring intense cooling on its surface specifically. In a modern gas turbine, inlet temperature is in fact very high it is well above melting temperature of HPT components. Figure 1-3 shows the adiabatic flame temperature of various fuels plotted against equivalence ratio.

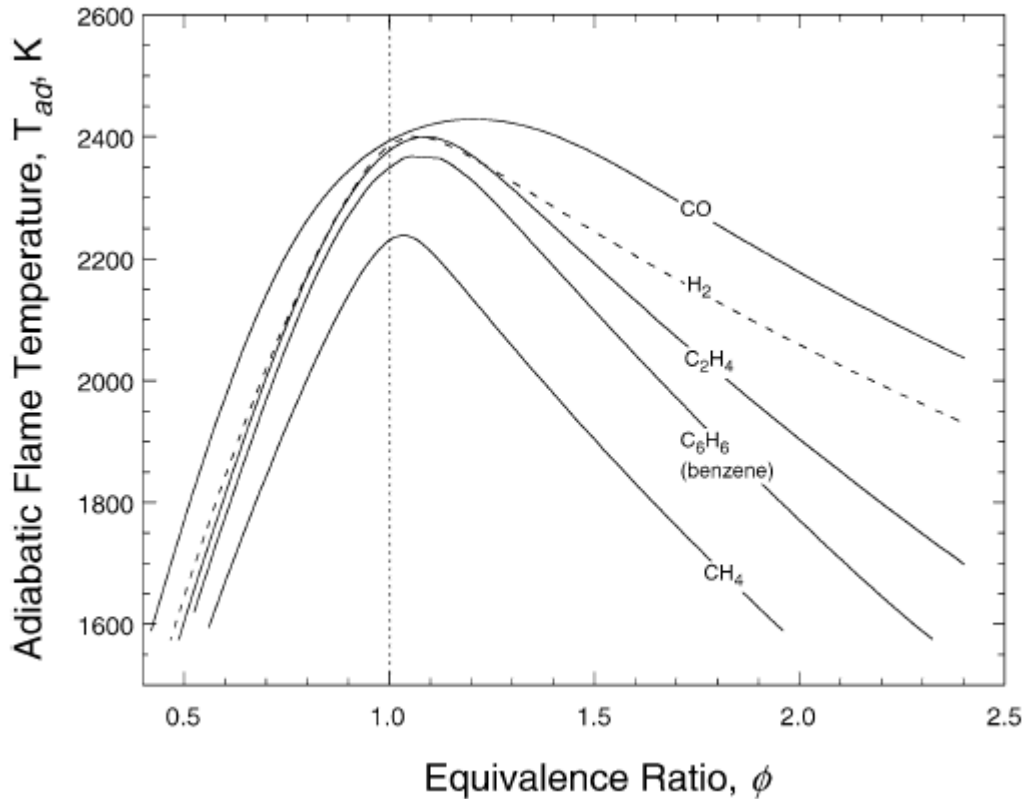


Figure 1-3 Adiabatic flame temperature of various fuels (Law et al. 2006)

The figure shows clearly flame temperatures of orders way higher than melting temperatures of turbine components as shown in Table 1-1 (components materials are adopted from Giampaolo (2006) and melting temperatures are from various materials manufacturers). The only way to do so while keeping these components intact is by providing protection to parts in direct contact with very high temperature mainstream flow. Various techniques are used commonly to do so, namely, the use of high temperature resisting coatings, internal cooling passages and film cooling, which is in the heart of this work.

Table 1-1 Melting temperature of various gas turbine components (Giampaolo 2006 and various materials manufacturers)

Turbine Component	Material	Industrial Nomenclature	Melting Temperature
Stator Vanes	Aluminum	RR 58	660 °C
	Titanium	6A1-4V	1660 °C
	Stainless Steel	A286, Chromally, Jethete M. 152, Greek Ascoloy, FV 535, FV500, 18/8,	1500 °C
	Precipitation Hardening Super Alloy	Nimonic 75, Nimonic 105	1550 °C
Rotor Blades	Aluminum	RR 58	660 °C
	Titanium	6A1-4V, TBB	1660 °C
	Stainless Steel	A286, Greek Ascoloy, FV 535, FV520, 17-4 Ph, 403	1500 °C
	Precipitation Hardening Super Alloy	Inco 718, Nimonic 901	1550 °C
Discs, Spool, Drum	Titanium	6A1-4V, TBA (IMI 679), IMI 381	1660 °C
	Steel	4340, FV 448, B5-F5, 9310	1427 °C
	Stainless Steel	410, 17-4 Ph, Jethete M. 152, Chromally (FV 535)	1500 °C
	Precipitation Hardening Super Alloy	Incoloy 901, Inco 718, Nimonic 901	1550 °C
Shafts, Hubs	Steel	Hykoro, 4340, 9310, B5-F5	1427 °C
	Precipitation Hardening Super Alloy	Inco 718	1336 °C

Before we incur to the film cooling injection into vane cascade, an inevitable introduction to the complex flow phenomena of vane cascades must be made, and that is what the next section will discuss.

1.2. Flow in vane cascades

Flow losses in a turbine stage are contributed to three main sources:

a) Profile loss: is the loss generated at the vane boundary layer and away from endwalls (hub and casing).

b) Leakage loss: tip leakage for rotors.

c) Endwall loss (secondary loss): is formed near end walls and is linked to profile loss.

Each of the three is accounted for one third of the total aerodynamic loss (Denton 1993) and the secondary losses in some cases accounts solely for 50% of it (Sharma and Butler 1987). This work is concerned only with the secondary loss.

One of the sources of complex flows in a turbine cascade is the horseshoe (HS) vortex. When the inlet flow reaches the stagnation point on a cylindrical shaped leading edge as

Figure 1-4 is showing, a static pressure gradient occurs, with lower pressure existing near endwall causing a downward rotational motion and a separation into two arms (Eckerle 1985).

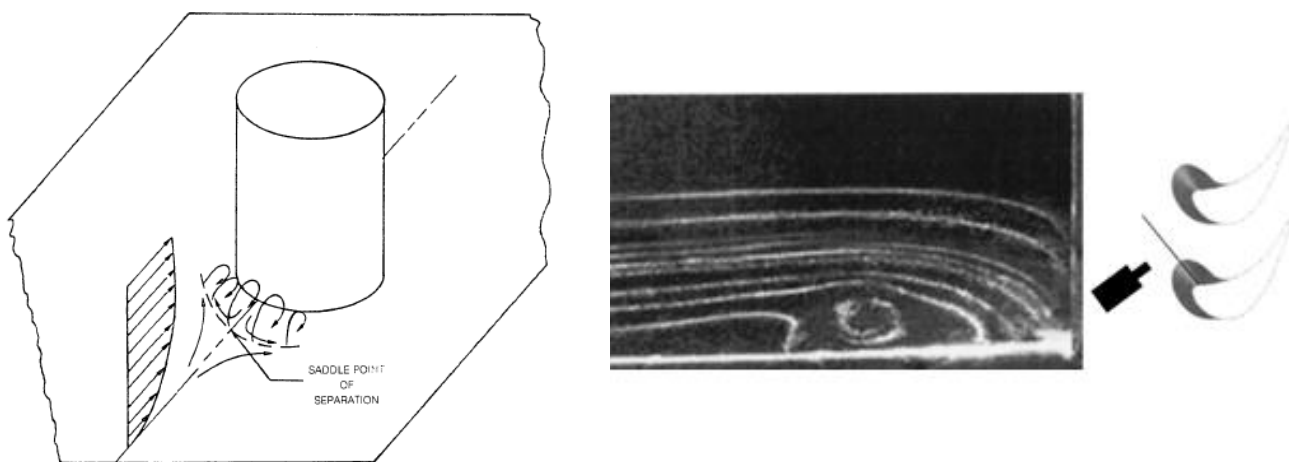


Figure 1-4 a) Horseshow vortex formation around a cylinder (Eckerle 1985), b) Leading edge-Endwall separation (Mahmood et al. 2005)

Very early attempts were made to fully understand the different flow phenomena occurring through the vane passage. In early seventies, aerodynamicists perceived that the secondary flow problem is in fact a boundary layer problem, meaning, a mere understanding of the flow up and downstream of the vanes is not nearly enough to interpret the performance of the vanes. Klein (1966) was pioneering in pointing out the leading edge role in generating cylinder body like flow pattern (Figure 1-5), he highlighted the horseshoe vortex calling it “stagnation point vortex”.

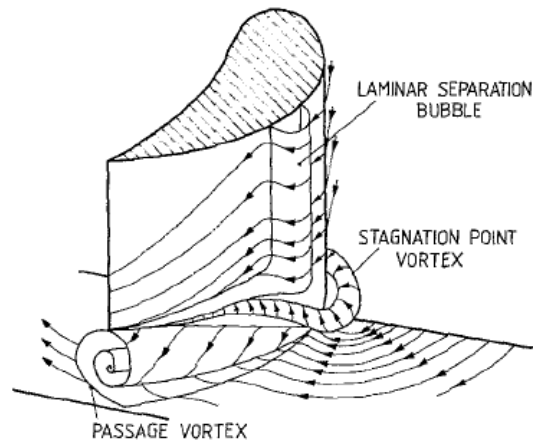


Figure 1-5 Flow in a cascade passage (Klein 1966)

Blair (1974) reported increased heat transfer rate at the leading edge and attributed it to the distortion of the end wall boundary layer by leading edge vortex. It was not until 1980 when Langston (1980) published his work, with a new interpretation of the flow in cascade passage, that the author believes the very first near complete secondary flow model.

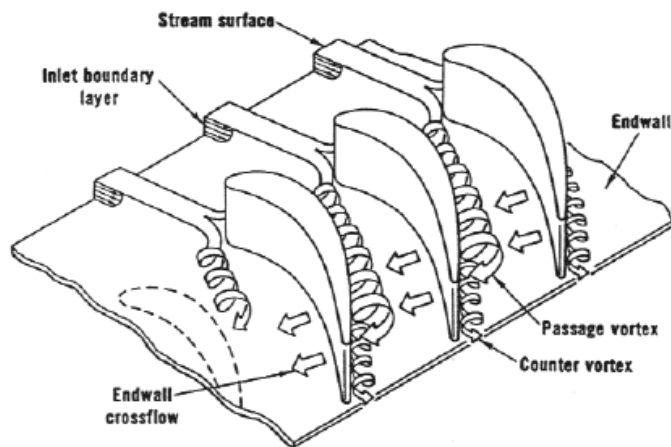


Figure 1-6 Secondary flow formation in linear cascade (Langston 1980)

He clearly stated that the pressure side horseshoe vortex leg gradually merges with the passage vortex, and the suction side leg remains attached to the suction side of the vane rotating in a counter direction to it (and at much smaller scale) forming what is called counter vortex (Figure 1-6). The work of Marchal and Sieverding (1977) disagrees with Langston's model on one thing, his measurements at different locations along the vane passage showed the counter vortex at midspan rather than at the corner as suggested by Langston.

A confirmation of Langston's model was made by Moore and Smith (1984), who injected ethylene at both the suction and pressure legs of the horseshoe vortex, and by tracing it he located the pressure side leg at the center of the passage vortex, while the suction side's was convected around the passage vortex core.

This dispute over the counter vortex location is due to the fact that it rotates at different speeds in different experimental setups as it is relevant to the inlet flow profile and passage shape and length.

A detailed explanation of the interaction and merge of the passage, suction and pressure side vortices was made by Sieverding and Bosche (1983) who used colored smoke to visualize flow evolution (Figure 1-7).

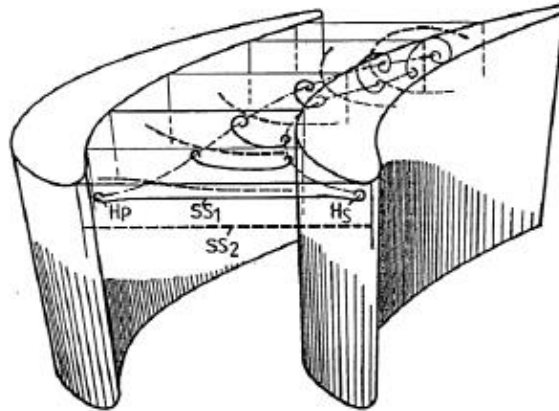


Figure 1-7 Laminar flow evolution in low speed air flow as visualized by smoke (Sieverding and Bosche 1983)

Their work resulted in a well-illustrated model of the flow, indicating two stream surfaces moving parallel to the end walls upstream of the vane SS1 and SS2. SS1 is bounded by the endwall boundary layer region while SS2 lies outside of the boundary layer, at the leading edges, both ends of the SS1 stream started to roll up rotating vertically at both ends of the passage, and as the flow moved further downstream, the vertical motion thickened, extending to the entire boundary layer and forming the passage vortex. The pressure side moved along with the passage vortex, while the suction side vortex started rotating around it, in a manner similar to what was previously described by Langston and Moore.

Although small in magnitude, hence hard to visualize, the existence of the corner vortex was made clear by measuring the turning angle near the endwall downstream of a high loading vane. The work of Gregory-Smith and Graves (1983) shows beyond any doubt the previously mentioned effect.

Langston (2001) describes the motion of the counter vortex around the axis of the passage vortex to be similar to the rotation of a planet around its sun. Sharma and Butler's (1987) measurements of the velocity, pressure and flow provided an evidence of this planet like rotational motion of the counter vortex. They were also able to prove the independence of the inlet flow profile from the overall turning of the flow at passage exit (Figure 1-8).

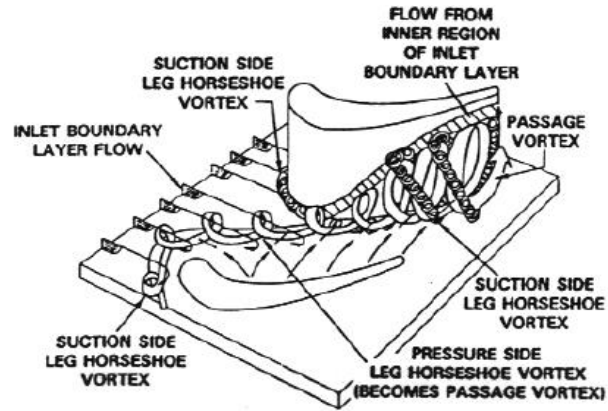


Figure 1-8 Secondary flow model (Sharma and Butler 1987)

Another loss attributed to secondary flows is the loss of lift; Langston et al. (1977) was able to show the effect by measuring static pressure at pressure and suction sides of the vane at different spanwise locations (2.3, 12.15, 25 and 50 percent). While the pressure side was showing relatively two-dimensional behavior, the severity of the secondary flow effect on lift loss was evident on the suction side of the airfoil near the endwalls (Figure 1-9).

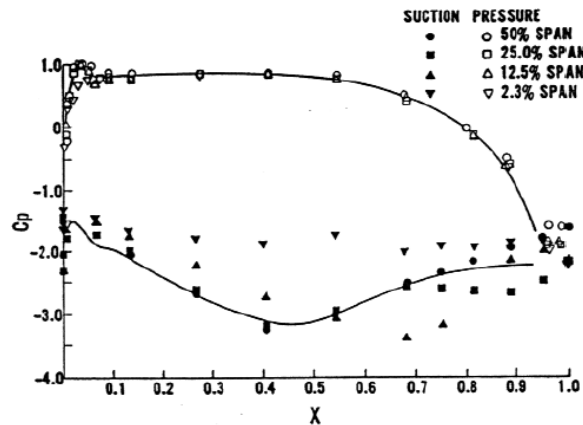


Figure 1-9 Static pressure distribution on airfoil surface (Langston et al. 1977)

Now with a thorough understanding of the formation and evolution of secondary flows, we can proceed to the next level of this work by illustrating how vane film cooling works.

1.3. Film cooling

Subjected to flue gas at temperatures higher than their melting temperatures, turbine components are vulnerable. Thus some means of protection is of necessity in order to keep them performing. Film cooling is a well-developed mean of cooling for turbines' components. It is a method in which penetrative holes are drilled in the profile and endwalls of a turbine vane, and through these holes a bleed of cool air delivered from the compressor and through internal cooling passages is provided at their surfaces.

1.3.1. Experimental investigation of film cooling in literature

Figure 1-10 shows a cascade vane with cooling holes on its surface and Figure 1-11 is a section view of the vane, showing bleeding from internal cooling passages through cooling holes.

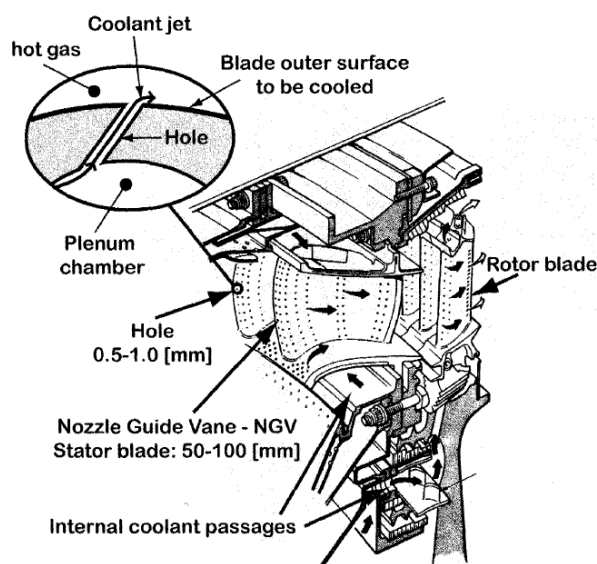


Figure 1-10 Film cooled HPT (Hill and Peterson 1992)

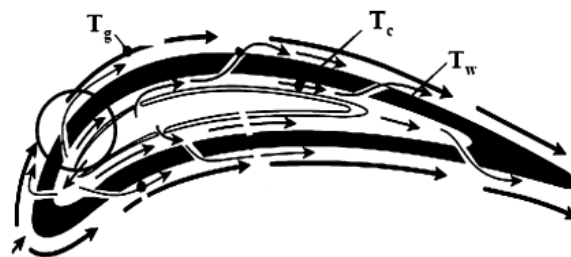


Figure 1-11 Film cooled HPT (Gritsch et al. 1998)

This helps in the protection of turbine components from exposure to hot mainstream by forming a layer of gas at much lower temperature (coolant temp. $\approx 800^\circ\text{C}$ while mainstream temp could be as high as 1300°C (Hill and Peterson 1992)), reducing the convection from hot mainstream flow to the metal surface, as the heat transfer rate to walls in the case of film cooling absence is defined as:

$$q'' = h(T_{\infty} - T_w) \quad \text{Eq. 1-1}$$

Where h is the heat transfer coefficient, T_{∞} is the mainstream temperature and T_w is the wall temperature. As film cooling is applied, restating equation 1-1 requires a new definition of the driving temperature of the heat transfer. In fact the driving temperature now is neither the mainstream nor the coolant. Simply because, downstream of the cooling hole, rapid variation in the boundary layer temperature is expected, due to mixing of the two flows. Thus equation 1-1 rather becomes

$$q''_f = h_f(T_g - T_w) \quad \text{Eq. 1-2}$$

Where T_g is the temperature of the gas in direct contact with the wall. The application of the film cooling contribution in heat transfer reduction can be assessed from the percentage change in the heat transfer rate which is translated into:

$$\Delta q = \frac{q'' - q''_f}{q''} = 1 - \frac{h_f(T_g - T_w)}{h(T_{\infty} - T_w)} \quad \text{Eq. 1-3}$$

As T_g goes down (better film cooling performance) one expects Δq to become higher, interpreting increased thermal benefit of film cooling.

A rather more common definition of the film cooling effectiveness in the literature is parameter η , where:

$$\eta = \frac{T_{\infty} - T_w}{T_{\infty} - T_c} \quad \text{Eq. 1-4}$$

A higher η is an indicator of better film cooling performance, which is why one expects η to peak at the trailing edge of cooling hole and decreases downstream of it. The factors influencing η are stated in Table 1-2.

Table 1-2 Factors affecting η (Thole and Bogard 2006)

Coolant/Mainstream conditions	Hole Geometry and configuration	Airfoil Geometry
Mass flux ratio	Shape of hole	Hole location - leading edge
Momentum flux ratio	Injection angle and compound angle of the coolant hole	- main body - blade tip - endwall
Mainstream turbulence	Spacing between holes P/d	Surface curvature
Coolant density ratio	Length of the hole, l/d	Surface roughness
Approach boundary layer	Spacing between rows of holes and number of rows	
Mainstream Mach number		
Rotation		

The injection of coolant into a mainstream flow is a compromise on more than one level. On one hand, implementing film cooling causes aerodynamic loss, but ideally the increase of the inlet temperature granted by it will make for that loss, resulting in a positive net effect on the cycle efficiency. A perfect film cooling design though will form total isolation of the turbine component surface while not mixing with the mainstream. On the other hand, the cold flow is bled from the compressor decreasing the mainstream flow rate; yet again the increase in the turbine inlet temperature represents an indemnity against that loss.

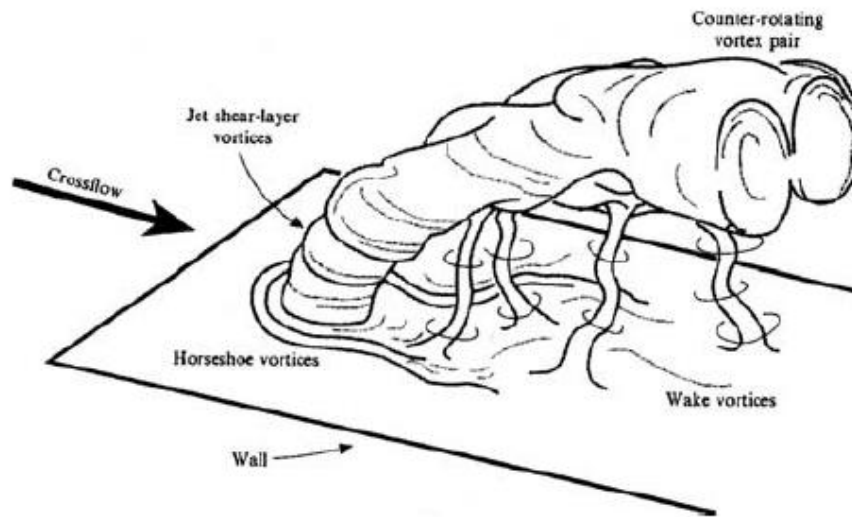


Figure 1-12 Jet in a crossflow (Roshko and Fric 1994)

Figure 1-12 is an illustration of different features associated with jet in crossflow. Scorer (1958) was one of the first to point out the formation of the counter rotating vortex. He associated this behavior to the rolling up of vorticity at the sides of the hole. While Andreopoulos and Rodi (1984), Sykes et al. (1986) and Fric (1990) agree with Scorer on how the counter rotating (kidney) vortex is formed. Sugiyama (1991) attributes it to the cross flow entrainment in the leeside of the jet.

Fearn and Weston (1974) investigated vorticity in the trajectory of a jet and found that the initial strength of the vortex pair is proportional to the jet velocity and its diameter and independent of the crossflow speed.

In their investigation of jet injection in crossflow Moussa et al. (1977) reported what they called negative vortex in the kidney-vortex and in an opposing direction it. They associated that so called “negative vortex” to the crossflow reaction to the “positive” kidney-vortex. It is worth noting that no one else in the literature points that negative vortex out.

Sugiyama (1995) investigated the pressure coefficient (C_p) distribution around the jet hole and concluded that the leading edge of the jet is not a stagnation point (unlike that of a solid cylinder). He also found that the C_p at the trailing edge is typically lower than that for solid cylinder.

As was previously mentioned, application of film cooling is promising to provide huge merit in turbine component thermal protection, its interaction with the secondary flows in the

mainstream is a cause of aerodynamic loss in the vane cascade. Extensive research was conducted on assessing that influence.

Day et al. (1999) have investigated this influence on aerodynamic efficiency in a large-scale transonic cascade vane, they used a foreign gas as coolant to mimic the density ratio of coolant to mainstream in actual turbines, and air in other runs. They concluded that while the coolant application resulted in merely an increase in the wake width and limited drawback on the loss (9% increase), increasing the flow rate of the coolant (in the foreign gas run) actually yielded less overall aerodynamic loss.

Nicklas and Kost (2001) and Nicklas (2001) conducted an experiment on a high pressure turbine nozzle guide vane (NGV) with cooling slot upstream of the vane and cooling holes on the endwall in the vane passage, they studied the interaction between the endwall flows and film cooling injection and concluded that film cooling resulted in a reduced endwall cross flow and consequently reduced passage vortex, the cooling slot placed in the saddle point region upstream of the vane increased the intensity of the horseshoe vortex driving the coolant away from the endwall and into the main flow region, they also noted rise in the turbulence intensity caused by the coolant injection. The effects of these flow phenomena resulted in a decrease in the pressure side heat transfer coefficient that was even lowered downstream. They suggested addition of cooling holes downstream of the vane passage to help boosting the heat transfer coefficient downstream.

In actual turbine conditions, the film cooling injection is generally not steady and rather of pulsating nature, Lalizel et al. (2012) carried out experiment on film cooling flat plate to analyze the effect of injected coolant pulsation, and concluded that for low blowing ratio (BR = 0.65) pulsation led to lowered η while for high BR (1.25) this behavior reversed where pulsating was better than steady coolant flow.

Tacina et al. (2003) investigated influence of mainstream turbulence intensity on film cooling effectiveness on a flat plate experimentally and found that increasing the turbulence intensity from 7 to 35% resulted in huge decrease in the film cooling effectiveness of 50%.

The effect of film cooling in a low aspect ratio ($h/C = 0.5$) vane was studied experimentally by Takeishi et al. (1990), who found that the secondary flows effect on heat transfer coefficient with no film cooling is more significant on the suction side than on the pressure side and also that the horseshoe vortex near the leading edge had a limiting effect on the film cooling effectiveness and even increased the heat transfer coefficient in that region. They also concluded that a 2-D heat transfer model was able to predict the heat transfer coefficient correctly except in the endwall regions.

1.3.2. Numerical investigation of film cooling in literature

Several numerical investigations of film cooling on flat plate and vanes are presented in the literature. Bohn and Kusterer (1999) investigated numerically the mixing of film coolant injection from inclined holes in the vicinity of the leading edge, with one of the holes on suction and another on pressure side as the Figure 1-13 shows. Their work did show mild agreement with experimental measurements in terms of general vortices behavior on the lee side of the jet but with some unexplained intense flows though.

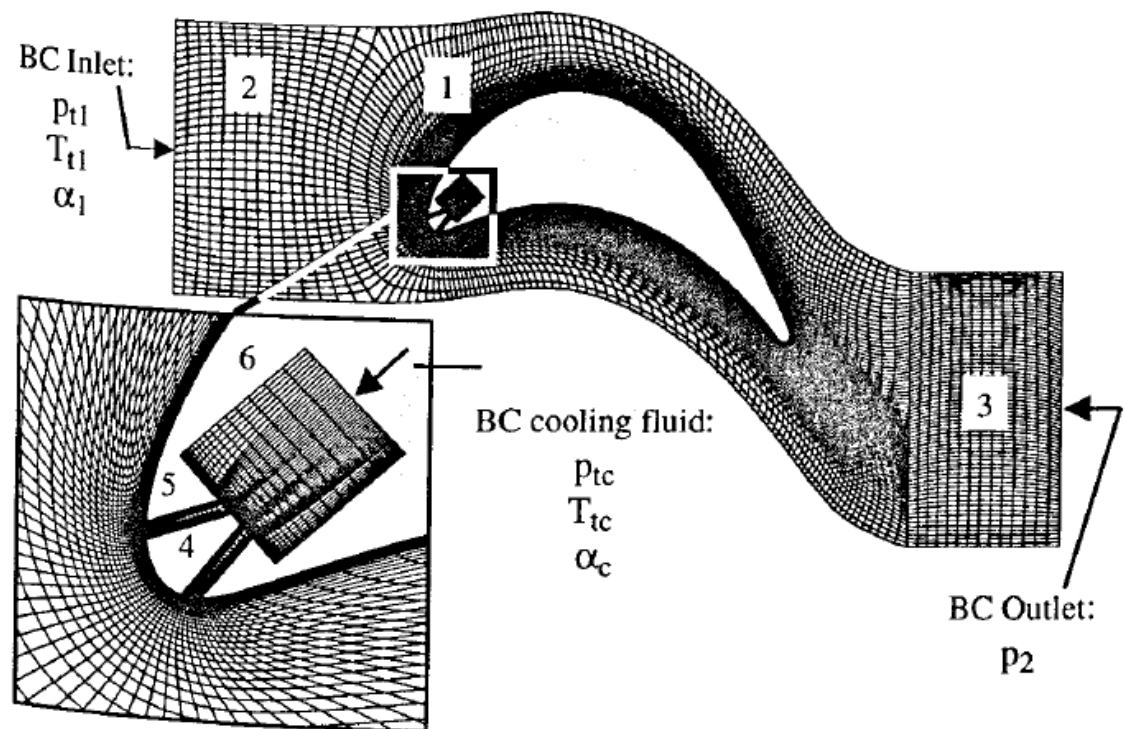


Figure 1-13 2-D view of numerical grid (Bohn and Kusterer 1999)

The numerical representation of film cooling injection by modeling discrete holes is a computationally expensive process; this is mainly due to the fact that film cooling injection affects the flow on a scale way smaller than that of the mainstream, e.g. secondary flow formation. This means that in order to represent the cooling holes accurately and sufficiently, grid refinement near the holes will lead to increased number of numerical cells hence almost defeating the purpose of using numerical analysis approach. Garg and Rigby (1995) modeled three staggered rows of film cooling holes on a vane using 3-D model of the coolant plenum, cooling tubes and mainstream domain, in their work a comparison was made with a previous study where coolant was applied at the vane surface as BC and with experimental measurements, they concluded that the complete modelling of the plenum and coolant holes was able to match the experimental measurements more accurately. Hildebrandt et al. (2006) went further in that context, comparing modeled discrete holes to source terms implementation. With a similar conclusion on the merit of discretized cooling plenum and tubes modeling and stating that the source term is more feasible in industrial day to day design tasks “but suffers not only from a lack of detailed flow information” they stated “but more important from an uncertainty in the specification of the correct boundary condition for the source terms.”. Their conclusion for the best practice in that regard is to first model the full discretized domain, i.e. with coolant plenum and tubes, and from it deduce the correct boundary conditions to be used for source terms for further analysis. But even then, they digress, the immediate vicinity of the cooling holes will not be captured accurately.

Andreini et al. (2013) used source terms to model the effusion cooling holes in a combustion chamber, effusion cooling is similar to film cooling in concept, with two difference, first is the smaller diameter of cooling holes and second is holes count across the surface. In their model, they used mass sink on the cold side of the plate, mass source on the hot side and heat sink to account for cooling as show in Figure 1-14.

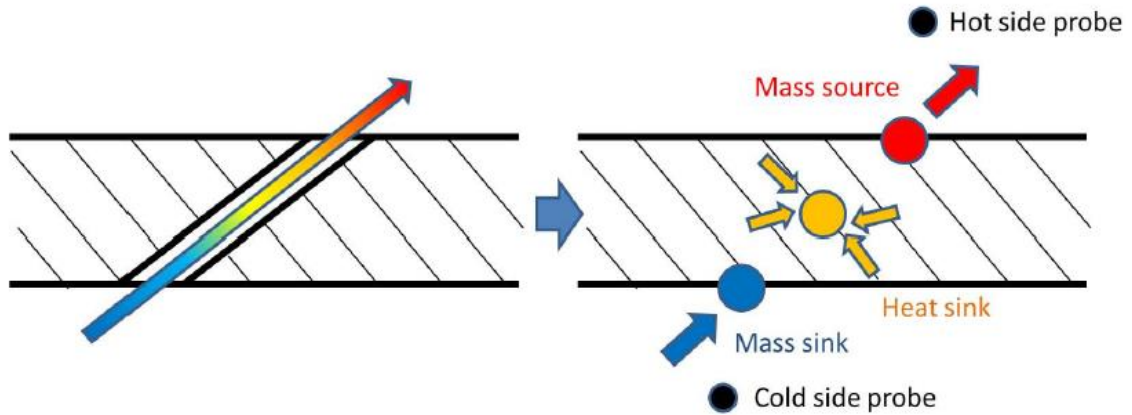


Figure 1-14 Source terms representation of effusion cooling holes (Andreini et al. 2013)

They concluded that source terms approach did obtain satisfying results, however great deal of sensitivity to surface mesh element size near the source location, recommending that the size if the elements doesn't exceed 50% of the hole diameter. They also found that the investigated approach works best with higher blowing ratios ($BR = 5$) and decreases as the blowing ratio decreases.

In the endeavour for a reliable and feasible numerical modeling of film cooling Heidmann and Hunter (2001) developed a volumetric source term to work with coarse grids and was able to achieve fair agreement with experimental data for flat plate film cooling.

2. Research motivation and outline

Considering their possible influence on gas turbines, vane cascade film cooling implementation has to be assessed properly in the design phase to avoid missing the point of having them in the first place. A proper design of film cooling will achieve a few goals, namely: sufficient protection of turbine components, limited influence on mainstream flow and providing uniform cooling avoiding formation of hotspots. The most common way to do so is by experimental measurements.

Although expensive and time consuming, experiments are considered to be very reliable and accurate for different fluid dynamical measurements. An alternative to the experimental approach is numerical simulation. With advancement in the physical and mathematical models as well as computational capabilities of modern computers, Computational Fluid Dynamics (CFD) is becoming more robust and reliable in flow phenomena calculations making it more commonly used for different turbomachinery components design. However, the modeling of film cooling domain and its integration with the mainstream domain remains to be unfeasible for industrial applications for the time and computational expense it implements. This work is intended to assess a new technique for applying film cooling into vane cascade domain without reconstructing the numerical grid of the cascade. This will not only save huge gridding time, but will also bring the computational time needed to solve discrete film cooling holes down as the domain only sees the film cooling injection as boundary condition at the vane surface.

In order to do so, the work is discretized into three main parts:

- A) Film cooling: a validation case of the proposed film cooling injection approach against experimental data of flat plate film cooling.
- B) Uncooled vane: simulation of uncooled vane cascade. The numerical simulation of the flow phenomena is compared to experimental measurements.
- C) Cooled vane: 9 runs at different cooling locations and under different flow conditions, i.e. blowing ratio, for the same vane geometry of the uncooled case. And are also compared to experimental measurements.

3. Research methodology

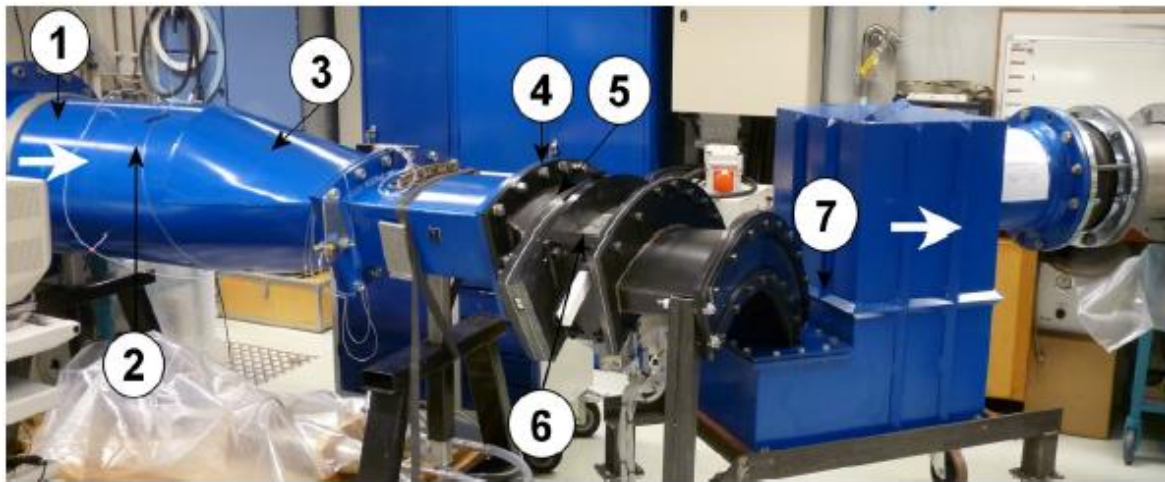
The present work is CFD simulation of the experimental measurements obtained at the testing facility at the Energy Technology Department in Royal Institute of Technology (Kungliga Tekniska Högskolan KTH, Stockholm, Sweden). Hence before proceeding to the numerical part of the analysis, the next section will briefly familiarize the reader with the experimental measurements facilities for both the vane cascade and flat plate film cooling.

3.1. Experimental benchmark

3.1.1. Annular Sector Cascade (ASC)

Figure 3-1 shows the testing facility of the annular sector cascade (ASC) and its components, the air flow is supplied by a twin screw compressor powered by a 1MW electric motor, capable of supplying a max flow rate of 4.7 kg/s at pressure 4 bars. The air exit temperature is 180°C, a cooler is used to cool the air temperature down to 30°C. The flow into the cascade is controlled by 2 inlet valves and two by-pass valves. The pressure at the outlet is drove by an exhaust fan.

The first part of the test facility is a settling chamber (2) that contains a honeycomb and 5 mesh screens in order to smoothen the flow. Then the flow starts to gradually go from a circular to annular section in a contraction part (3). Part (4) is where the turbulence grids (Figure 3-2) are placed to control the turbulence intensity of the mainstream flow.



1) Inflow. 2) Settling chamber. 3) First radial contraction. 4) Turbulence grid. 5) Second radial contraction. 6) Test section with NGVs. 7) Outflow.

Figure 3-1 ASC arrangement (Bartl 2010)



Figure 3-2 Fence (up) and parallel bar (down) turbulence grids (Saha 2012)

A second contraction section (5) is used to ensure the flow is entering the NGVs test section with no radial or tangential components. The NGVs test section (6) cutaway is shown in Figure 3-3 and a cross section of it is shown in Figure 3-4 highlighting locations where measurements were made. It is a replica of an old 5 passages vane test section, as it was found that the use of 4 passages was sufficient to generate periodicity of flow (Bartl 2010)

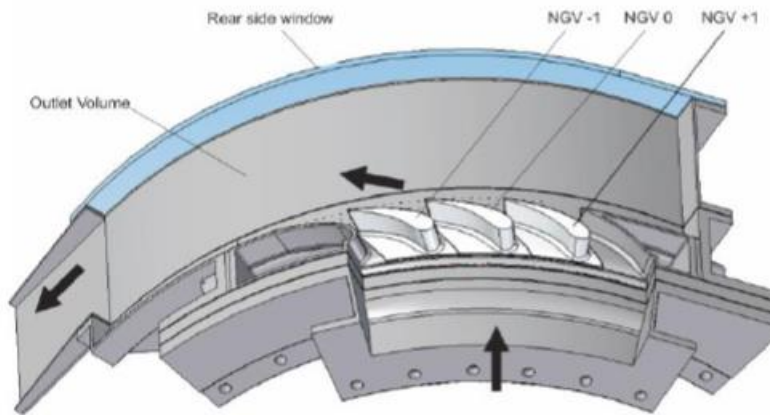


Figure 3-3 NGVs test section cutaway (El- Gabry et al. 2012)

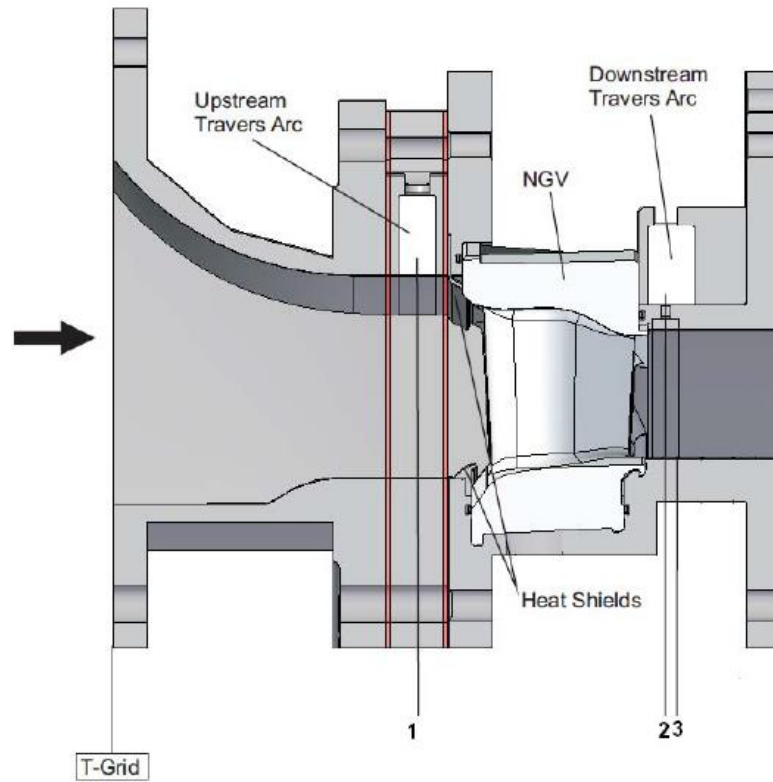


Figure 3-4 NGVs test section (Saha et al. 2013)

A cross-section view of the NGV can be seen in Figure 3-5 and the geometrical features of it are presented in Table 3-1.

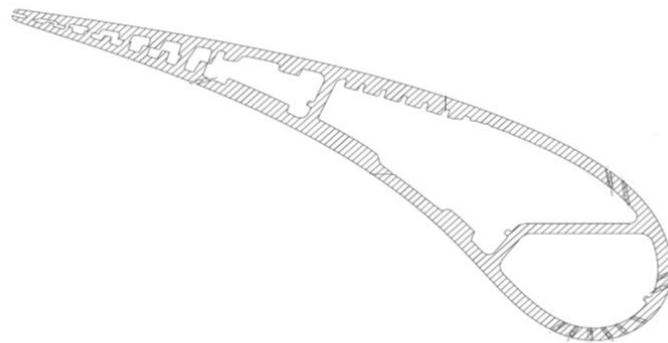


Figure 3-5 NGV cross-section (Saha et al. 2013)

Table 3-1 NGV geometric parameters (Saha 2012)

Design Parameter	Value
True chord (c)	129.2 mm
Axial chord at hub radius ($c_{ax, hub}$)	62.5 mm
Pitch-to-chord ratio at midspan	0.826
Hub radius at exit	615.3 mm
Tip-to-hub ratio at exit	1.097
Aspect ratio based on TE vane height ($h_{TE/c}$)	0.463
Average effective exit angle (α_{ef})	16.05°
LE radius	13.8 mm

The denoted location 1 in Figure 3-4 is $-55.7\% C_{ax, hub}$ and is where inlet pressure is measured. Location 2 is $107.1\% C_{ax, hub}$ with 5-hole L-probe of diameter 2.5mm (Figure 3-6 (a)) and 3-hole L-probe of diameter 0.6mm (Figure 3-6 (b)) calibrated for M ranges from 0.1 to 0.95 in a semi-open calibration rig are used for pressure measurements. While endwall pressure at $136.5\% C_{ax, hub}$ (location 3) is measured using 9 pressure taps.

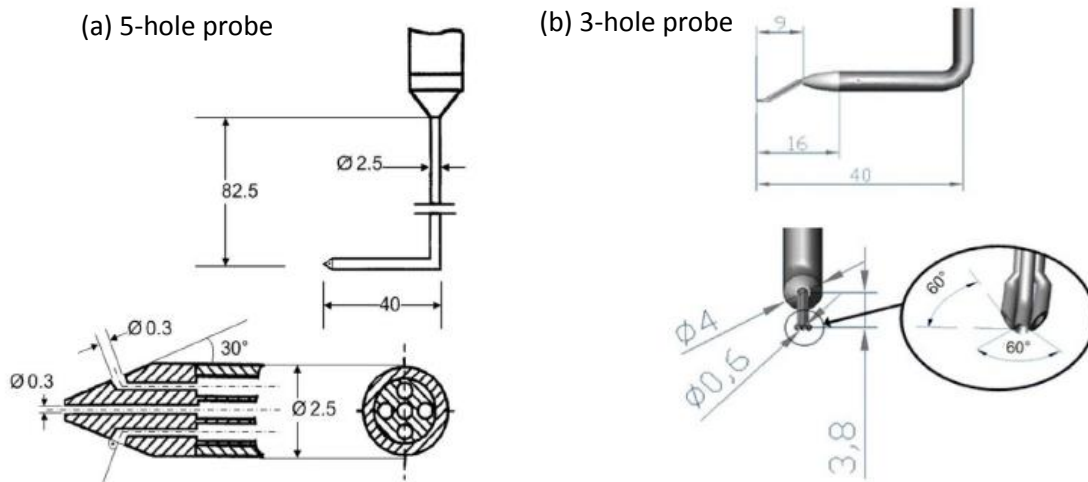


Figure 3-6 5-hole and 3-hole probes (Saha 2012)

Pressure taps of diameter 0.4mm are placed on the NGVs surfaces at 25%, 50% and 75% span locations. NGV0 is equipped with 45 taps, NGV-1 with 43 taps and NGV+1 with 29 taps. The pneumatic pressure is measured using 2 PSI scanners (PSI 9116) with accuracy of $\pm 0.05\%$ of its full range which corresponds to ± 51.75 Pa ± 103.5 Pa and its value is averaged from 60 subsequent scans. While the atmospheric pressure is measured using a Solartron barometer with accuracy of $\pm 0.01\%$ of its full range, corresponding to ± 11.5 Pa. The total uncertainty of the measured kinetic energy loss (ζ_{kin}) is $\pm 0.18\%$ and is equal to $\pm 0.06^\circ$ of the exit flow angle (α).

The experimental measurements obtained for comparison with CFD simulation are listed in Table 3-2.

Table 3-2 Vane cascade experimental data obtained

		Exit flow angle	Vorticity	Total pressure distribution	Aerodynamic loss
Uncooled		√	√	√	√
PS1	Y_{nom}	√	--	--	√
	Y_{hi}	√	--	--	√
	Y_{low}	√	--	--	√
SS1	Y_{nom}	√	--	--	√
	Y_{hi}	√	√	√	√
	Y_{low}	√	--	--	√
SS2		√	--	--	√
SH	Y_{nom}	√	--	--	√
	Y_{hi}	√	√	√	√

3.1.2. Flat plate film cooling

The flat plate film cooling measurements were made in a large scale (30X) model in an open loop suction type wind tunnel (Figure 3-7). The inlet flow is sucked through the square section tunnel 20.32x20.32 cm and 86.36 cm in length. The mainstream passes through screens, grid and filters to assure uniformity and 4% intensity turbulence level. The cooling holes are 1.9 cm in diameter and spaced at $Y/D=3$ with an inclination angle of 30° with the flat plate (Figure 3-8). The coolant flow goes through one manifold then into three different flow meters and to 45 cm hose and 30 cm acrylic tube, to guarantee a fully developed flow at the hole exit as the total length of the flow path from the manifold and to the hole exit is twice the required entrance length for the higher blowing ratios ($L/D > 23$) and is insulated.

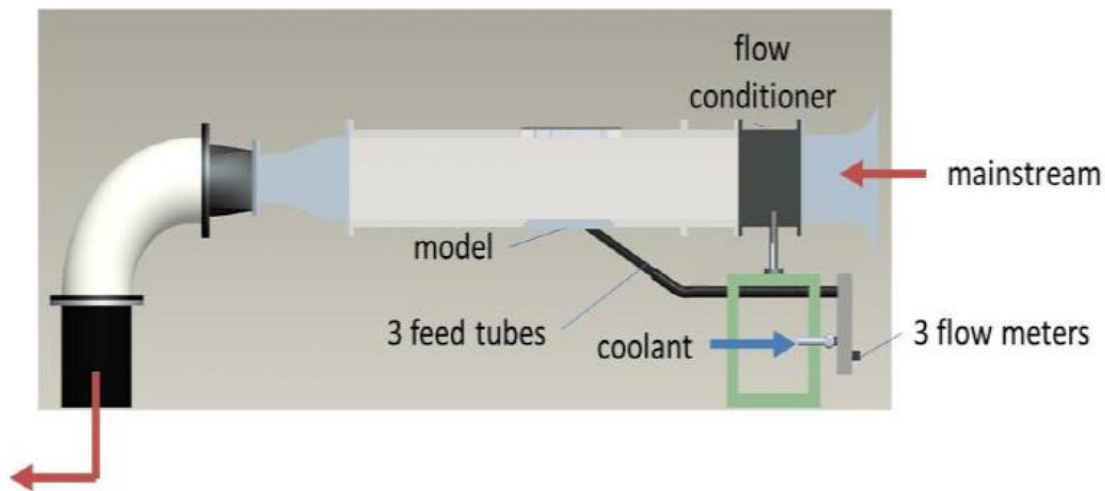


Figure 3-7 Flat plate wind tunnel schematic drawing (El-Gabry et al. 2011)

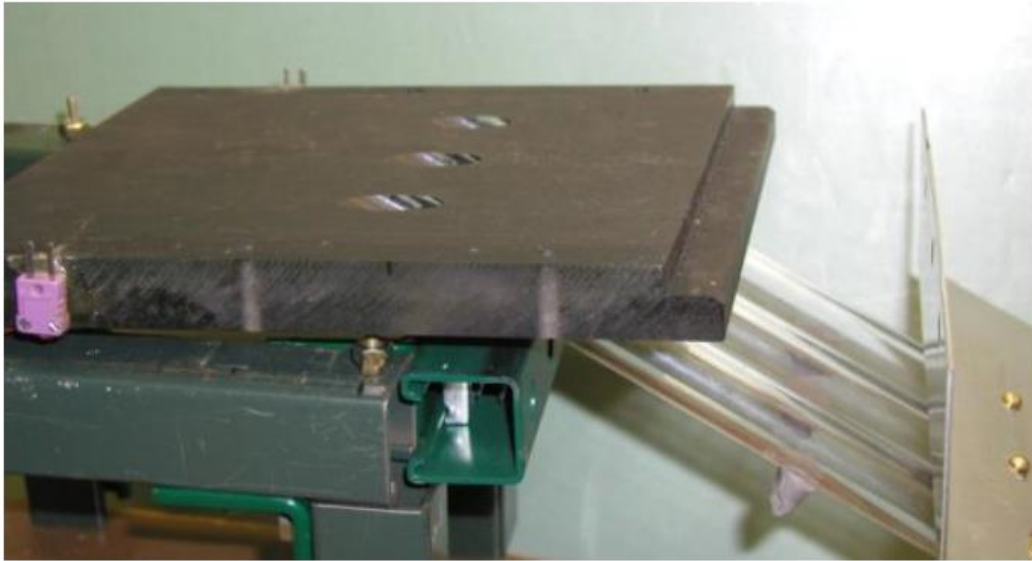


Figure 3-8 Flat plate film cooling holes (El-Gabry et al. 2011)

Mainstream velocity is measured using a pitot tube at the entrance of the tunnel and the temperatures are measured using thermocouples. While the velocity and turbulence measurements are conducted using single and two-wire hotwire system. The hotwire is powered by constant temperature anemometry system and the data is acquired at 50Hz rate for 3 seconds. The used hotwire system is calibrated in the wind tunnel test section with no coolant flow and the hotwire is positioned normal to the flow direction varying the velocity from 0 to 45.7 m/s while recording the voltage across the wire and relating it to the measured velocity using 4th polynomial.

The same procedures were followed with the two-wire (X-wire) probes, with one difference, that is, the wires were in position 45 ° with the mainstream flow direction, two X-wire probes were used, one to measure u & v components of velocity and fluctuations and one for u & w components. The uncertainty of the mean velocity measurements is 4%.

Table 3-3 lists the experimental data obtained for comparison from the film cooled flat plate.

Table 3-3 Flat plate film cooled experimental data obtained

	Centerline film cooling effectiveness	Normalized flow velocity along centerline	Normalized flow field temp along centerline	Normalized flow velocity downstream of the hole
BR1	√	√	√	--
BR2	√	√	√	√

3.2. Numerical analysis

In this work a Computational Fluid Dynamics (CFD) model is used to validate the results of experimental measurements of flow in a NGV. CFD provides the means to analyze flow in a gas turbine at substantially lower cost and virtually less time than experimental measurements. In this work the commercially available CFD software ANSYS CFX was used. The next section is an introduction to CFX.

3.2.1. Introduction to CFX

CFX is general purpose finite element based, control volume, implicit software² developed by ANSYS, Inc. It simulates the flow domain using the Reynolds Averaged Navier-Stokes (RANS) equations.

It can work either integrated with the ANSYS workbench or independently. For the present work the latter approach was chosen and the latest version (14.5) of the software was used. Creating the numerical domain with ICEM software and then importing it into CFX for analysis.

3.2.2. Governing equations

For CFD simulations, a set of mathematical equations describing the physical problem are solved (governing equations). The governing equations are a mathematical description complying with the three basic principles of fluid dynamics. Namely:

- 1- Mass is conserved.
- 2- Rate of change in momentum is equal to sum of forces (Newton's second law).
- 3- Rate of change of energy equals the sum of rate of heat addition to, and work done on fluid particle (first law of thermodynamics).

The RANS equations for steady-state 3-D compressible flow are listed herein.

Continuity

$$\text{div}(\bar{\rho}\tilde{\mathbf{U}}) = 0 \quad \text{Eq. 3-1}$$

x-momentum

$$\text{div}(\bar{\rho}\tilde{\mathbf{U}}\tilde{\mathbf{U}}) = -\frac{\partial \bar{P}}{\partial x} + \text{div}(\mu \text{grad } \tilde{\mathbf{U}}) + \left[-\frac{\partial(\bar{\rho} u'v')}{\partial x} - \frac{\partial(\bar{\rho} u'v')}{\partial y} - \frac{\partial(\bar{\rho} u'w')}{\partial z} \right] \quad \text{Eq. 3-2}$$

y-momentum

$$\text{div}(\bar{\rho}\tilde{\mathbf{V}}\tilde{\mathbf{U}}) = -\frac{\partial \bar{P}}{\partial x} + \text{div}(\mu \text{grad } \tilde{\mathbf{V}}) + \left[-\frac{\partial(\bar{\rho} u'v')}{\partial x} - \frac{\partial(\bar{\rho} v'^2)}{\partial y} - \frac{\partial(\bar{\rho} v'w')}{\partial z} \right] \quad \text{Eq. 3-3}$$

z-momentum

$$\text{div}(\bar{\rho}\tilde{\mathbf{W}}\tilde{\mathbf{U}}) = -\frac{\partial \bar{P}}{\partial x} + \text{div}(\mu \text{grad } \tilde{\mathbf{W}}) + \left[-\frac{\partial(\bar{\rho} u'w')}{\partial x} - \frac{\partial(\bar{\rho} v'w')}{\partial y} - \frac{\partial(\bar{\rho} w'^2)}{\partial z} \right] \quad \text{Eq. 3-4}$$

² ANSYS CFX Technical Specifications

Energy

$$\text{div} \left[\bar{\rho} \tilde{u}_j \left(\tilde{H} + \frac{\tilde{u}_i \tilde{u}_i}{2} \right) + \tilde{u}_j \frac{\overline{\rho u_i'' u_i''}}{2} \right] = \text{div} \left[-q L_i - \overline{\rho u_i'' h''} + \overline{t_{ji} u_i''} - \overline{\rho u_j'' \frac{1}{2} u_i'' u_i''} \right] + \text{div} \left[\tilde{u}_i (\tilde{t}_{ij} - \overline{\rho u_i'' u_j''}) \right] \quad \text{Eq. 3-5}$$

Where the overbar indicates time averaging and the tilde is a density weighted average.

Equation of state

$$\mathbf{P} = \bar{\rho} R \tilde{T} \quad \text{Eq. 3-6}$$

The turbulence model used in all the runs in this work is the Shear Stress Transport (SST) model. SST model is a 2-equation model introduced by Menter (1994) and is presented as having the strengths of both the k-ε and k-ω models and none of their weaknesses. On one hand it implements a transformation of the standard k-ε into Wilcox's (1988) k-ω model near the walls (in the viscous sub-layer regime) benefiting from its merit in handling adverse pressure gradient, while using the standard k-ε model in the free-stream and shear-free flows to benefit from k-ε insensitivity to inlet turbulence properties.

For the new model, the k-equation (Turbulence-energy equation) remains the same as in the original Wilcox (1988) k-ω model, which is:

$$\text{div} (\rho k \mathbf{U}) = \text{div} \left[\mu + \frac{\mu_t}{\sigma_k} \text{grad}(K) \right] + P_k - \beta^* \rho \omega k \quad \text{Eq. 3-7}$$

Where $P_k = \left(2\mu_t S_{ij} \cdot S_{ij} - \frac{2}{3} \rho K \frac{\partial U_i}{\partial x_j} \delta_{ij} \right)$ is the rate of turbulent kinetic energy production.

However the ε-equation (Turbulence-dissipation equation) is transformed into ω-equation by assuming ε = kω and becomes:

$$\text{div} (\rho \omega \mathbf{U}) = \text{div} \left[\mu + \frac{\mu_t}{\sigma_{\omega,1}} \text{grad}(\omega) \right] + \gamma_2 \left(2\rho S_{ij} \cdot S_{ij} - \frac{2}{3} \rho \omega \frac{\partial U_i}{\partial x_j} \delta_{ij} \right) - \beta_2 \rho \omega^2 + 2 \frac{\rho}{\sigma_{\omega,1} \omega} \frac{\partial k}{\partial x_k} \frac{\partial \omega}{\partial x_k} \quad \text{Eq. 3-8}$$

Near wall treatment is very sensitive to grid sizing at the wall, i.e. distance between the wall and nearest cell node in the vertical direction. The use of wall function in the viscous sublayer region (Figure 3-9) is good for coarser grids, while it shows bad flow predictions for finer grids. Generally, two approaches of the near wall flow are used, first is wall integration, that is simply sizing the grid whereas maximum y^+ doesn't exceed 2 for k-ω model and its derivatives and as low as 0.2 for k-ε model. Where:

$$y^+ = \frac{\rho \Delta y u_\tau}{\mu} \quad \text{Eq. 3-8}$$

The other approach is wall function, where the log-law of the wall (Schlichting 1955) is used to model the flow near the wall. The advantage of this approach is being able to model the flow

near the wall at relatively low grid sizes more feasible for analysis for industrial purposes. In order for the wall function to work correctly a y^+ value between 30 and 150 must be kept.

The used SST model switches between standard low-Re formulation and wall functions based on the grid spacing from the wall, the grids used in this work are intended to use the wall function by keeping y^+ above the critical value for switching (30) (Menter 2003) and are always kept below y^+ 150 (the upper bound for proper near wall solution).

More details on the SST turbulence model are provided in appendix A.

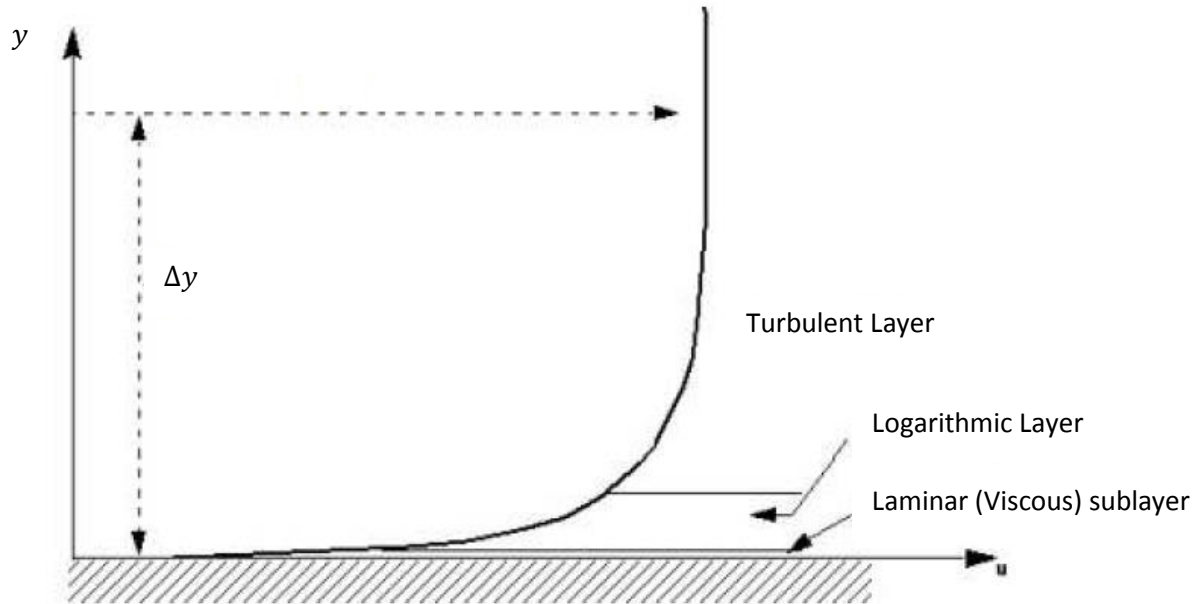


Figure 3-9 Turbulent Boundary Layer

3.2.3. Numerical domain

The CFD grid model is created using ICEM software. The approach used in ICEM to generate the mesh starts by discretizing the domain into smaller volumes called blocks. A good choice of blocking topology helps in later local refinement of the mesh at critical points where micro-level phenomena crucial for proper analysis are occurring.

3.2.3.1. Vane cascade numerical grid

The analysis of flow in vane cascade requires relatively fine grid at critical locations such as the trailing edge (TE) and near the walls for endwall flows capturing.

Figure 3-10 shows the blocking topology of the geometry in hand, as it can be seen; both the leading and trailing edges were given discretized blocks so that they can be more refined than their vicinity.

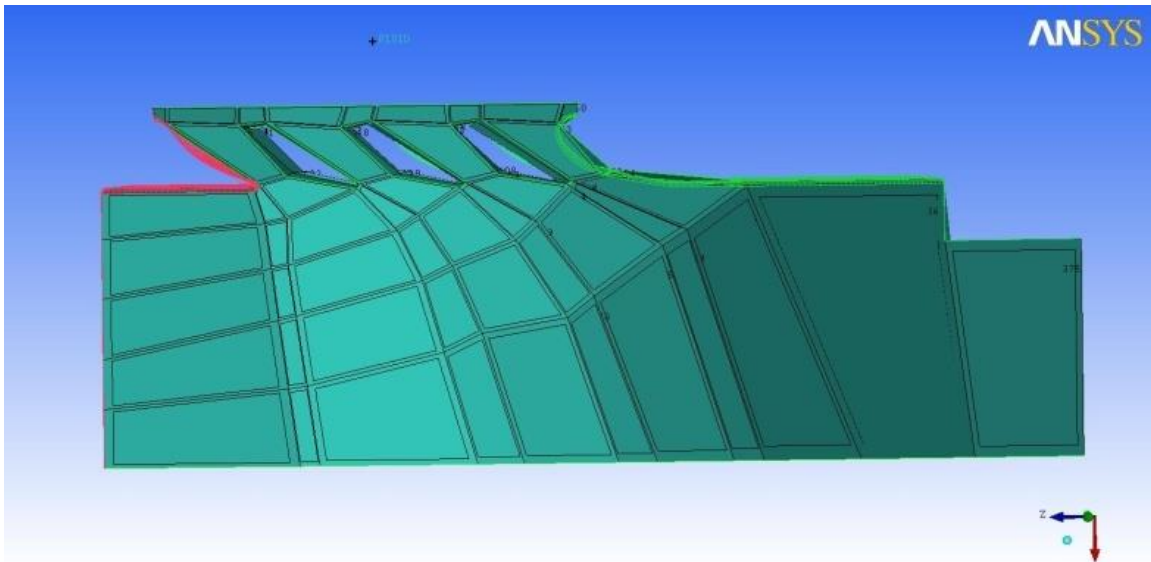


Figure 3-10 ICEM blocking strategy

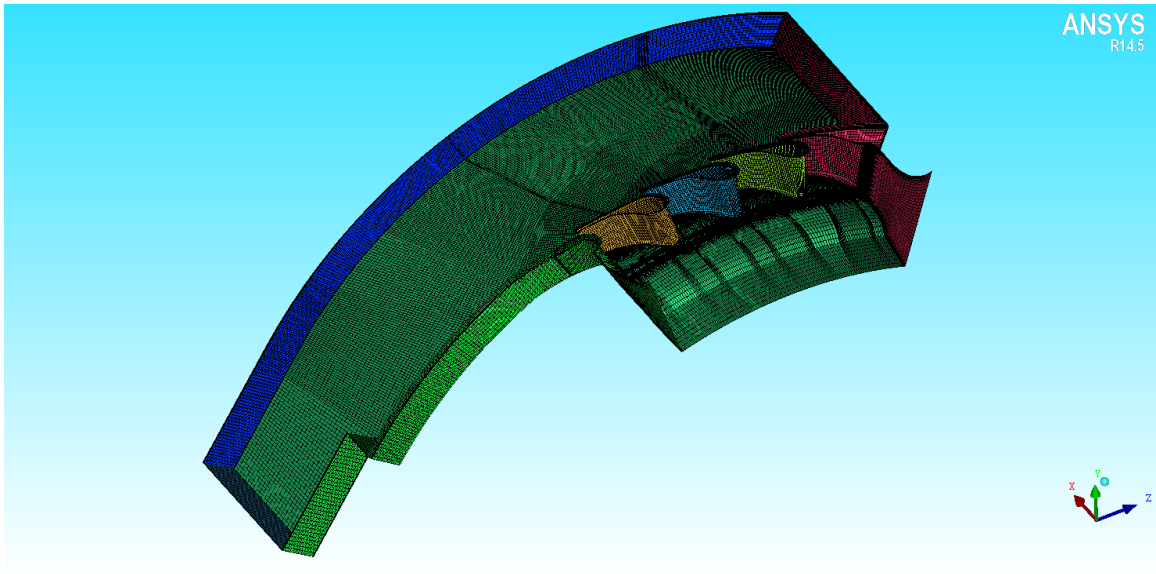


Figure 3-11 NGV numerical domain

Figure 3-11 shows an isometric view of the NGV numerical domain after the grid is generated. Close up shots of the same grid are shown in Figure 3-12 and Figure 3-13.

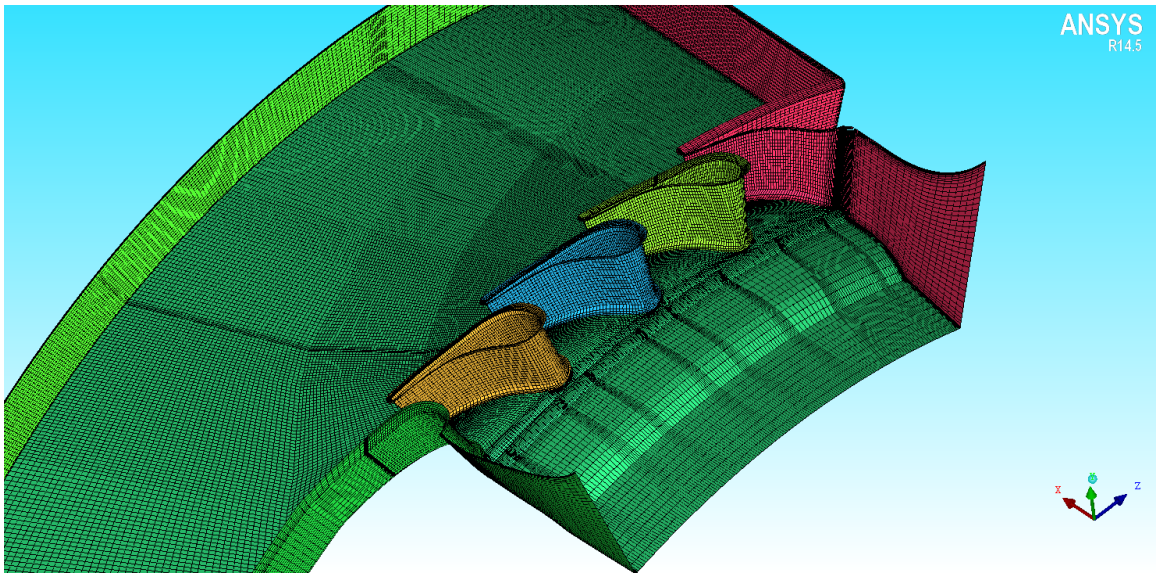


Figure 3-12 CFD grid for NGVs test section

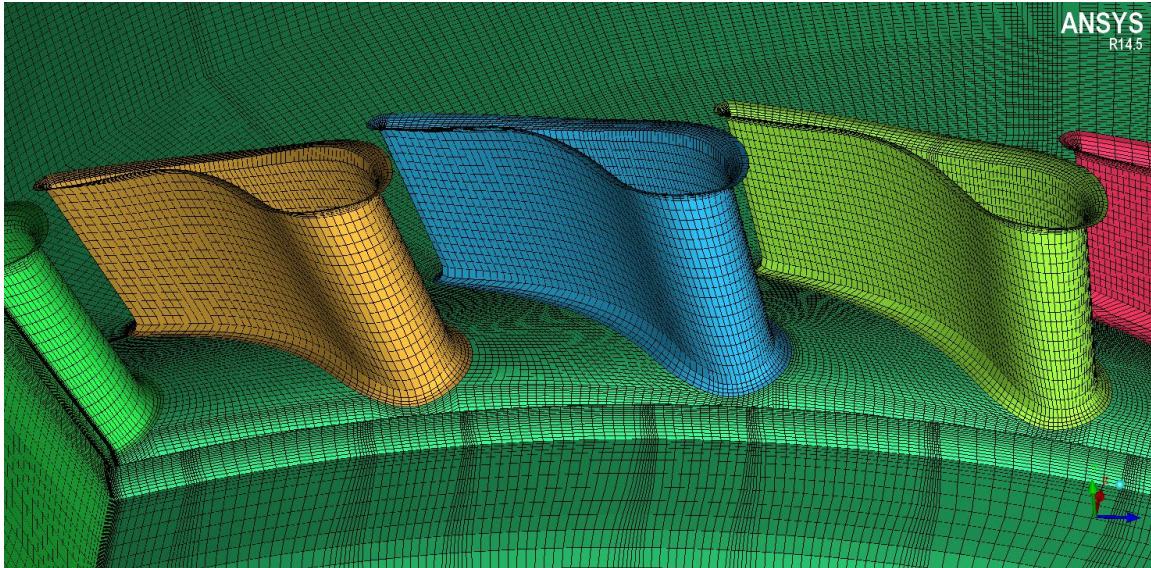


Figure 3-13 Periodic vanes grid

The boundary and initial conditions for the run setup are shown in Table 3-4. One must highlight here that the flow was treated as compressible fluid (air ideal gas) and second order advection scheme was used.

Table 3-4 Boundary and initial conditions for the CFX solver

Input	Value
Analysis Type	Steady state
Material	Air Ideal Gas
Reference pressure	0 kPa
Heat Transfer	Total Energy
Turbulence model	SST
Wall function	Automatic
Inlet	
Total pressure	170 kPa
Total temperature	303 K
Turbulence intensity	Medium (5%)
Outlet	
Static pressure	1 atm
Wall boundaries	
Mass and momentum	No slip wall
Wall roughness	Smooth wall
Heat transfer	Adiabatic
Advection scheme	High resolution
Timescale control	Auto timescale

The locations of data extraction points are shown in Figure 3-14 and the correspondent points are detailed in Table 3-5.

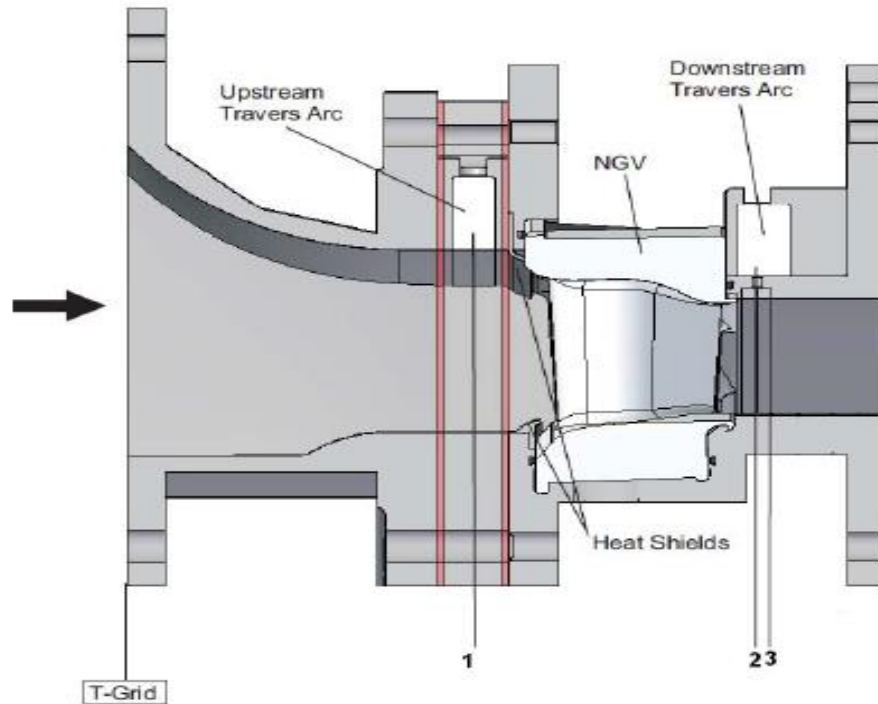


Figure 3-14 Data extraction points (Saha et al. 2013)

Table 3-5 Denomination and position of various locations

Nom.	Location	Note
T-Grid	-264% C_{ax} hub	Location of turbulence grid
1	-55.7% C_{ax} hub	Upstream traverse location
2	107.1% C_{ax} hub	Downstream traverse location
3	136.5% C_{ax} hub	Hub pressure taps

Two convergence criteria were used for all the runs. First is variation level in the flow domain below 0.01% and second is residual mean square (RMS) less than $1E-6$.

Figure 3-15 presents the pressure variation downstream of the vane trailing edge (location 2) at midspan plotted against normalized pitchwise location on the horizontal axis. The figure shows that the flow is periodic. This means that a single vane with periodic boundary conditions can be used in place of the four passage cascade model, thereby reducing associated

computational cost. The periodic model (Figure 3-16) is used for further analysis and computations.

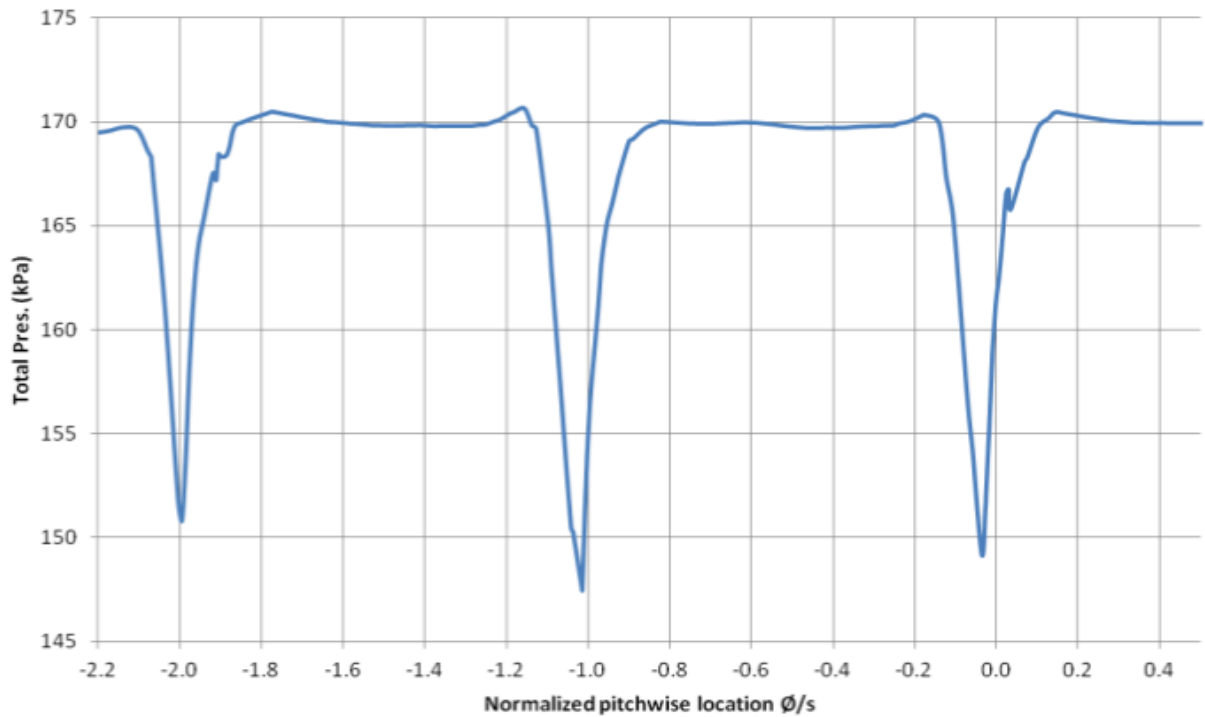


Figure 3-15 Total pressure at 107.1% Cax-hub and 50% span

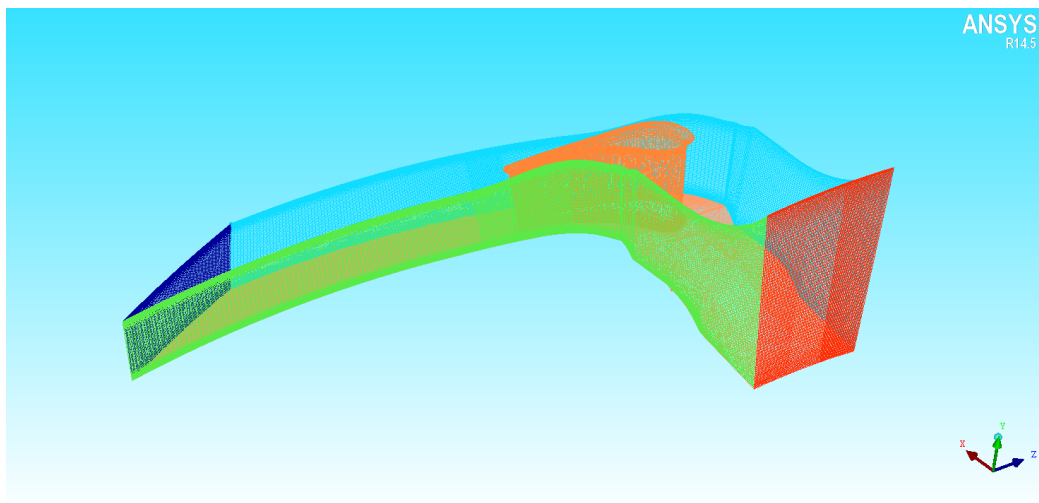


Figure 3-16 CFD grid for single vane

A grid independence check was conducted, using exit flow angle as the checking parameter. This is because exit flow angle is one of the experimental measurements made that will be studied in this numerical investigation. Different grids are described in Table 3-6. Figure 3-17 shows the outcome of the grid independence check; a grid of 2.4 million elements satisfies grid independence.

Table 3-6 single vane different grids

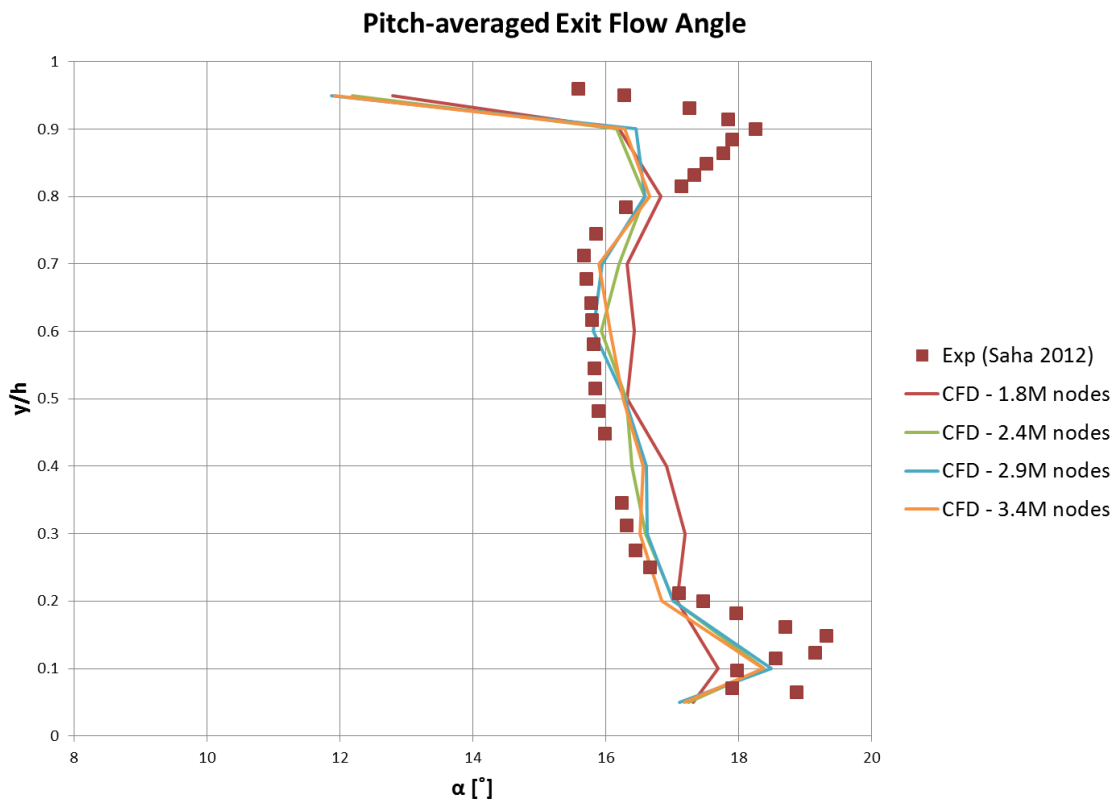
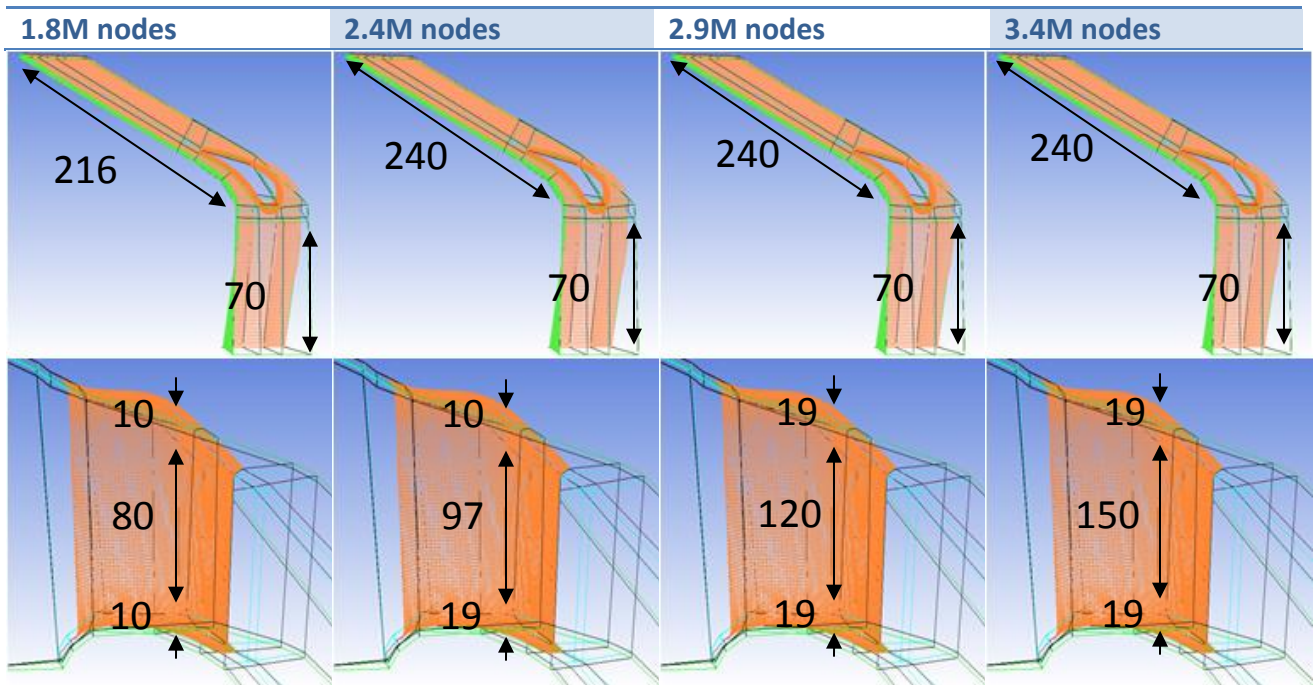


Figure 3-17 Grid independence check

3.2.3.2. Flat plate numerical grid

First, a CFD complete domain was used for original simulation (Figure 3-18). A pipe of $L/D = 30$ is used to feed the coolant to the flat plate surface to assure the flow is fully developed when it reaches the mainstream path. The grid points are shown in Figure 3-19.

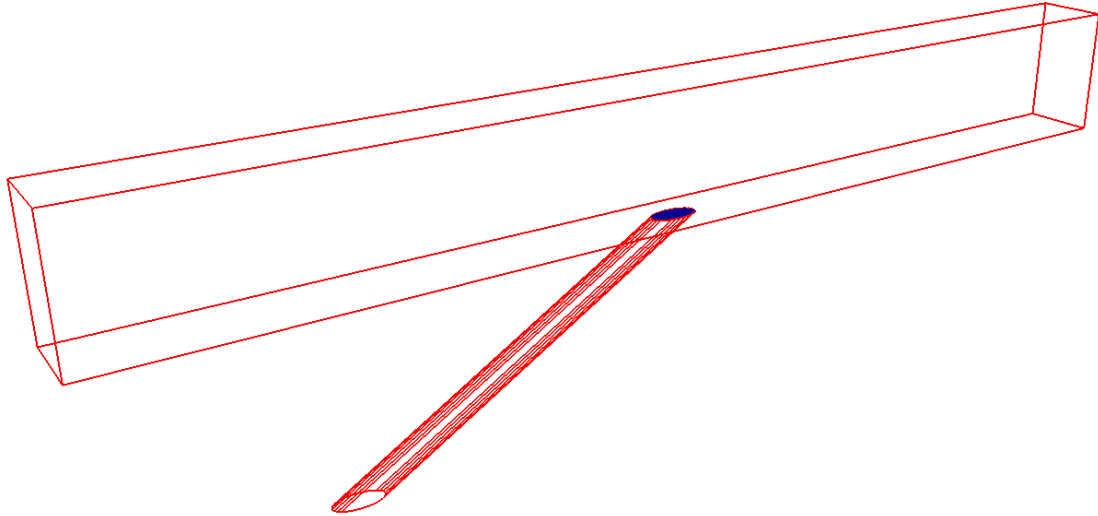


Figure 3-18 Flat plate with pipe CFD domain

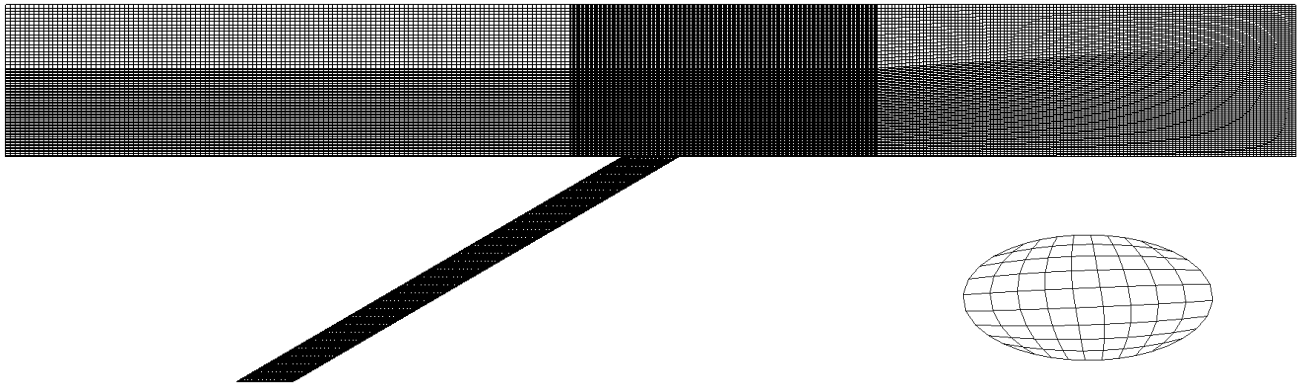
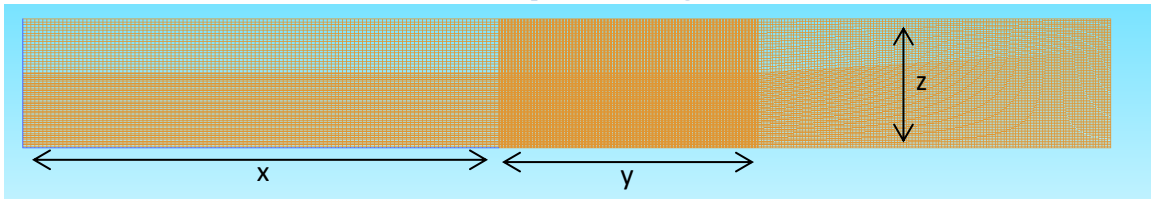


Figure 3-19 CFD grid domain

A grid dependence check was conducted on the grid using centerline η . The different grid sizes used for the check are elaborated in Table 3-7. A 2.0 million nodes grid was found to achieve independence (Figure 3-20) complying with the same convergence criteria of the vane cascade runs (less than 0.01% variation in the flow domain and RMS below $1E-6$).

Table 3-7 Flat plate different grid sizes



Grid size	x	y	z
1.7 M nodes	100	170	78
1.8 M nodes	120	244	63
2.0 M nodes	120	244	78
2.3 M nodes	120	244	86
2.4 M nodes	150	280	78

Film cooling effectiveness η

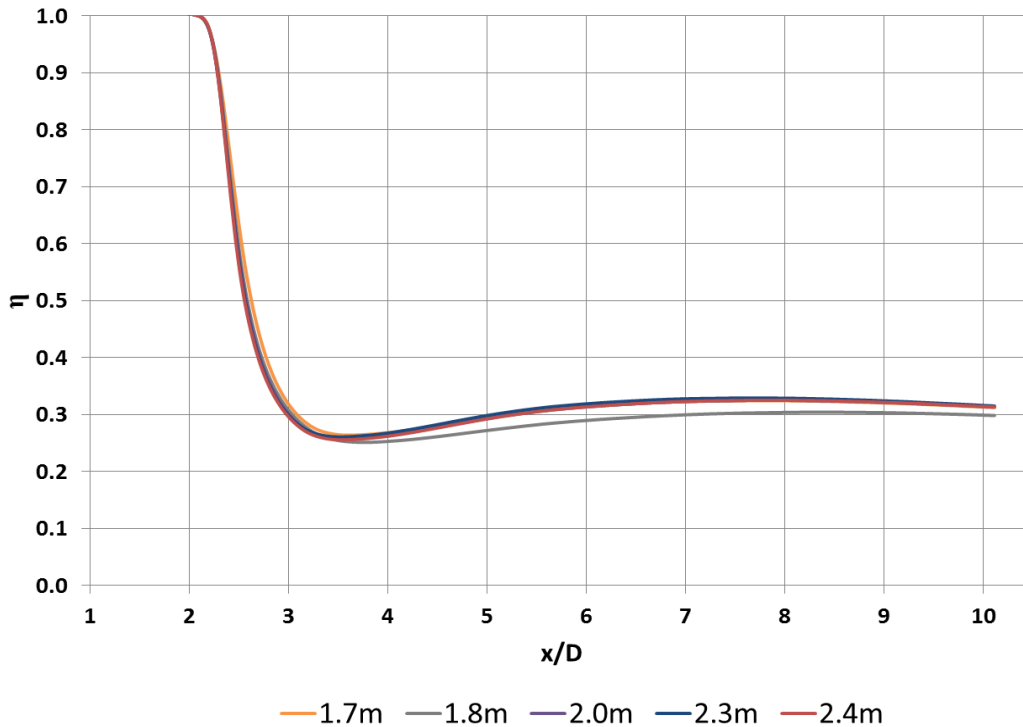


Figure 3-20 Flat plate grid independence check

The new approach was used for the second CFD simulation. In this case, the cooling pipe was spared and the coolant was intended to be fed directly at the flat plate surface. While that is easy to be done for one hole on the flat plate, it would be much harder to execute on the cooled vane. Given the number of holes needed to be modeled, the time will be taken to restructure and rebuild the grid with the holes will defeat the purpose of using the approach in the first place which is time and numerical cost reduction.

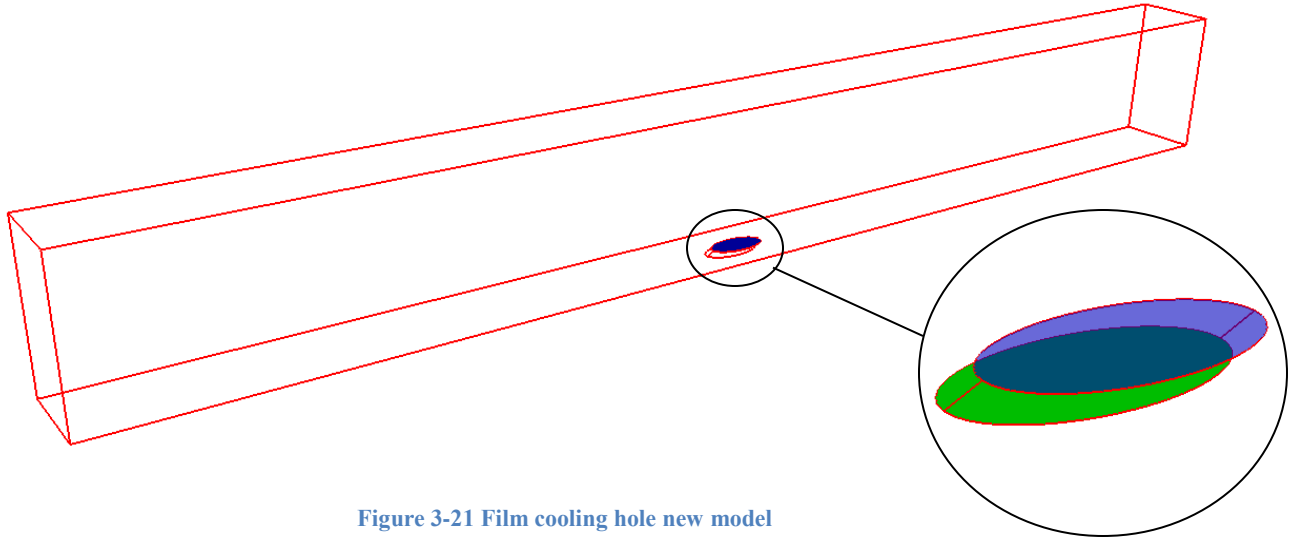


Figure 3-21 Film cooling hole new model

An autonomous CFD grid is built at the location of the hole. The new grid is in a way extrusion of the cooling hole and is one cell deep and has the same orientation of the cooling tube (Figure 3-22).



Figure 3-22 Cooling hole extrusion

Assigning the sides of the new grid a 'free slip wall' boundary condition and being very short in length (0.2 mm) it was fairly reasonable to assume that whatever BC was applied at the outer face of the domain will translate to the inner face (the hole). An assessment of that assumption was made by calculating the velocity at the cooling hole and it was found that a maximum deviation of only 8% occurred (Figure 3-23).

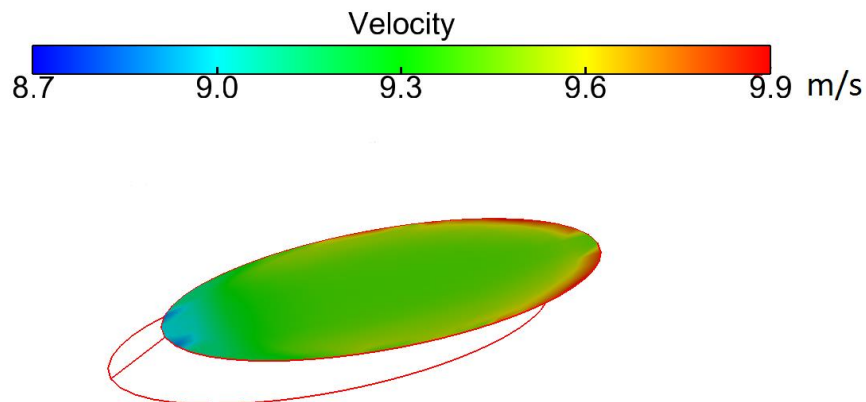


Figure 3-23 Velocity at coolant hole exit

This 8% deviation of velocity effect on the results of the simulation is shown in Figure 3-24 through a comparison of the normalized flow domain temperature contours for both new hole modeling approach (top) and velocity applied directly at the surface granting no deviation from the 9.1 m/s velocity value. It can be observed that merely any difference in the temperature domain is present.

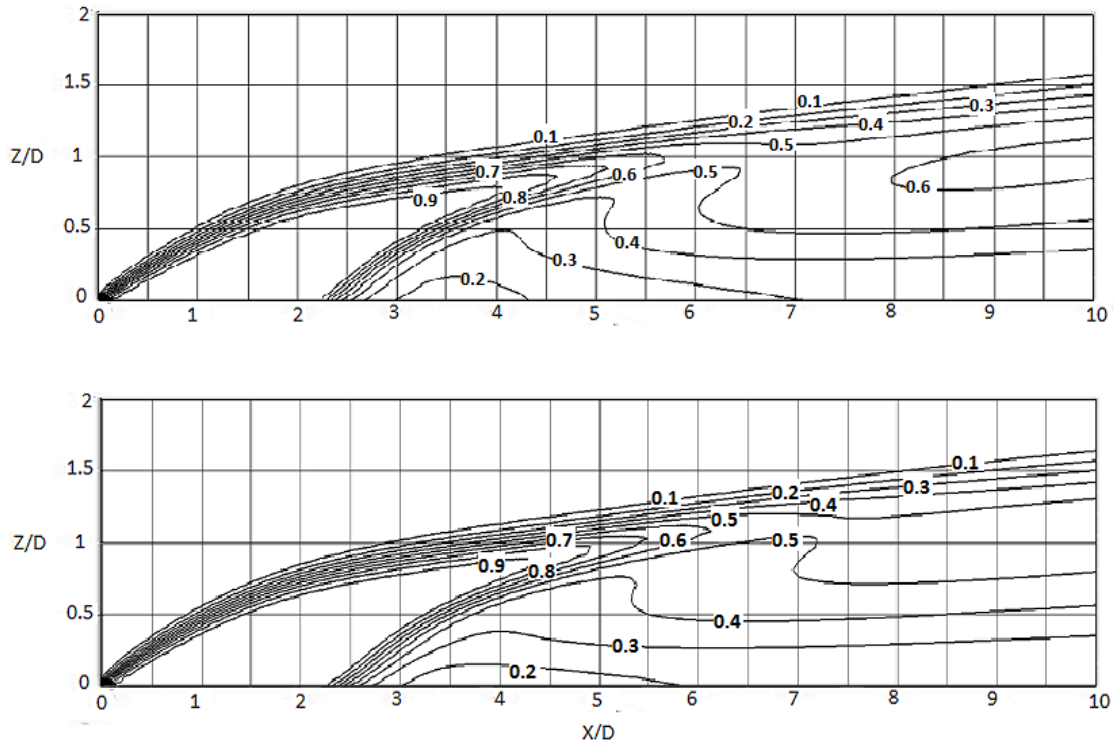


Figure 3-24 Normalized temperature for truncated case (up) and hole case (bottom)

Given its potential saving of gridding and computation time, the new approach was used for further analysis, and tested against experimental measurements of film cooled vane cascade, which will be discussed in details in the next chapter, to assess its validity for film cooling simulation.

4. Results and discussion

This section discusses the results of numerical simulation and compares the outcome to experimental measurements. It covers all parts of the work, namely, uncooled vane cascade, flat plate film cooling and cooled vane cascade with different configurations, in that order.

4.1. Uncooled vane

The uncooled vane analysis paves the way for cooled vane (the core of this work) and builds confidence in the chosen numerical models and grids.

4.1.1. Inlet flow total pressure

The total pressure distribution at the inlet (location 1 in Figure 3-14) presented in Figure 4-1 shows boundary layer thickness in the order of 10% normalized span; this is in agreement with the experimental measurements (Saha 2012) where the boundary layer thickness was found to be between 8-16% span.

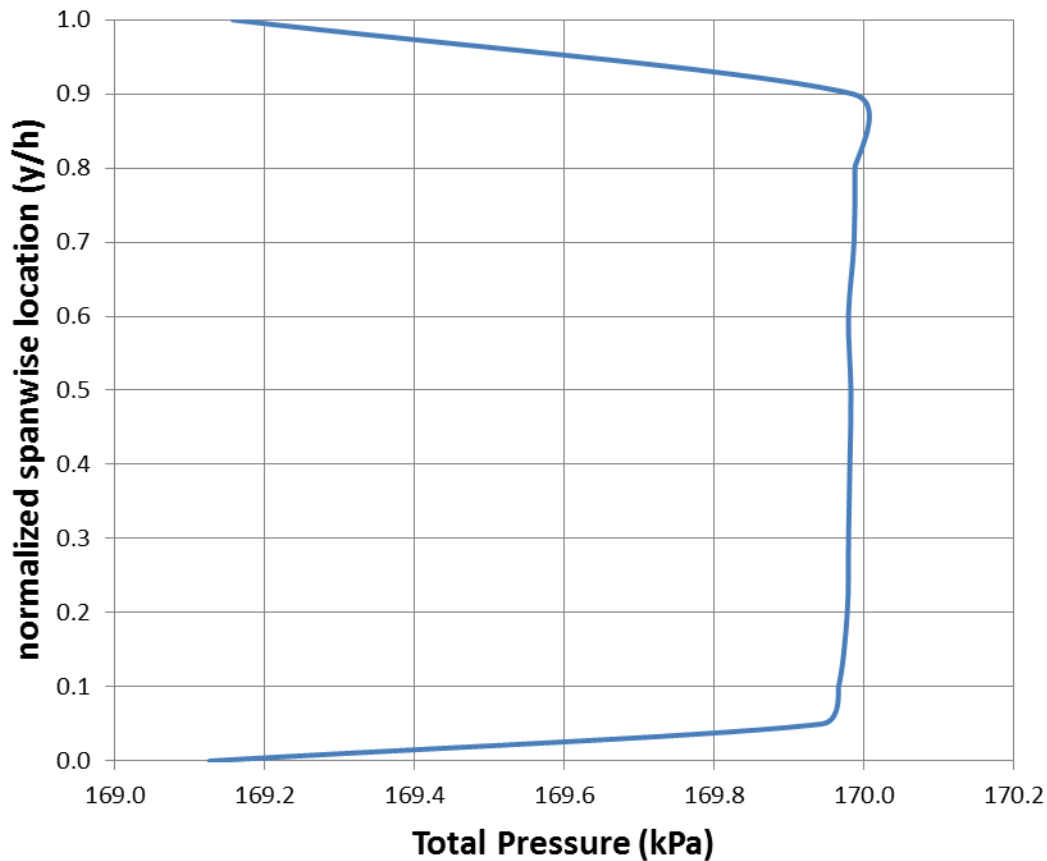


Figure 4-1 CFD calculation of inlet boundary layer

4.1.2. Vane loading

The isentropic Mach number on vane wall is an indication of the vane loading (Roux 2004), and is defined as

$$M_{iso} = \sqrt{\frac{2}{k-1} \left[\left(\frac{P_1}{P_s} \right)^{\frac{k-1}{k}} - 1 \right]} \quad \text{Eq. 4-1}$$

Where:

P_1 = Total pressure at inlet

P_s = Static pressure at vanes outlet (136.5% of C_{ax_hub})

Experiments were conducted at different Mach numbers. An operating point of 0.89 M was chosen for CFD analysis corresponding to a typical value of a transonic regime in nozzle guide vanes. The loading at midspan on the vane at $M_{iso}=0.89$ is shown in Figure 4-2. M_{iso} is plotted on the y-axis against the normalized axial vane location and is showing good agreement with experimental results.

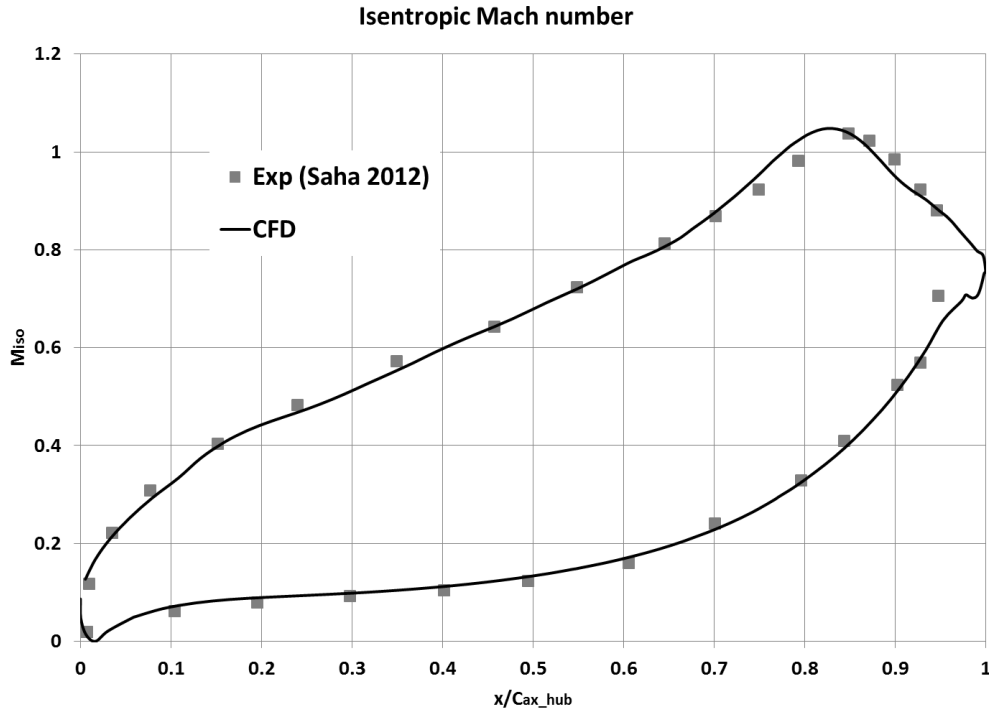


Figure 4-2 M_{iso} at 50% span

4.1.3. Exit flow angle distribution

The exit flow angle is a measure of turning of mainstream flow downstream of the vane, the geometry at hand has a reference turning angle of 16.05° at mid-span, higher values of exit flow angles indicates lower turning, and lower values indicates higher turning.

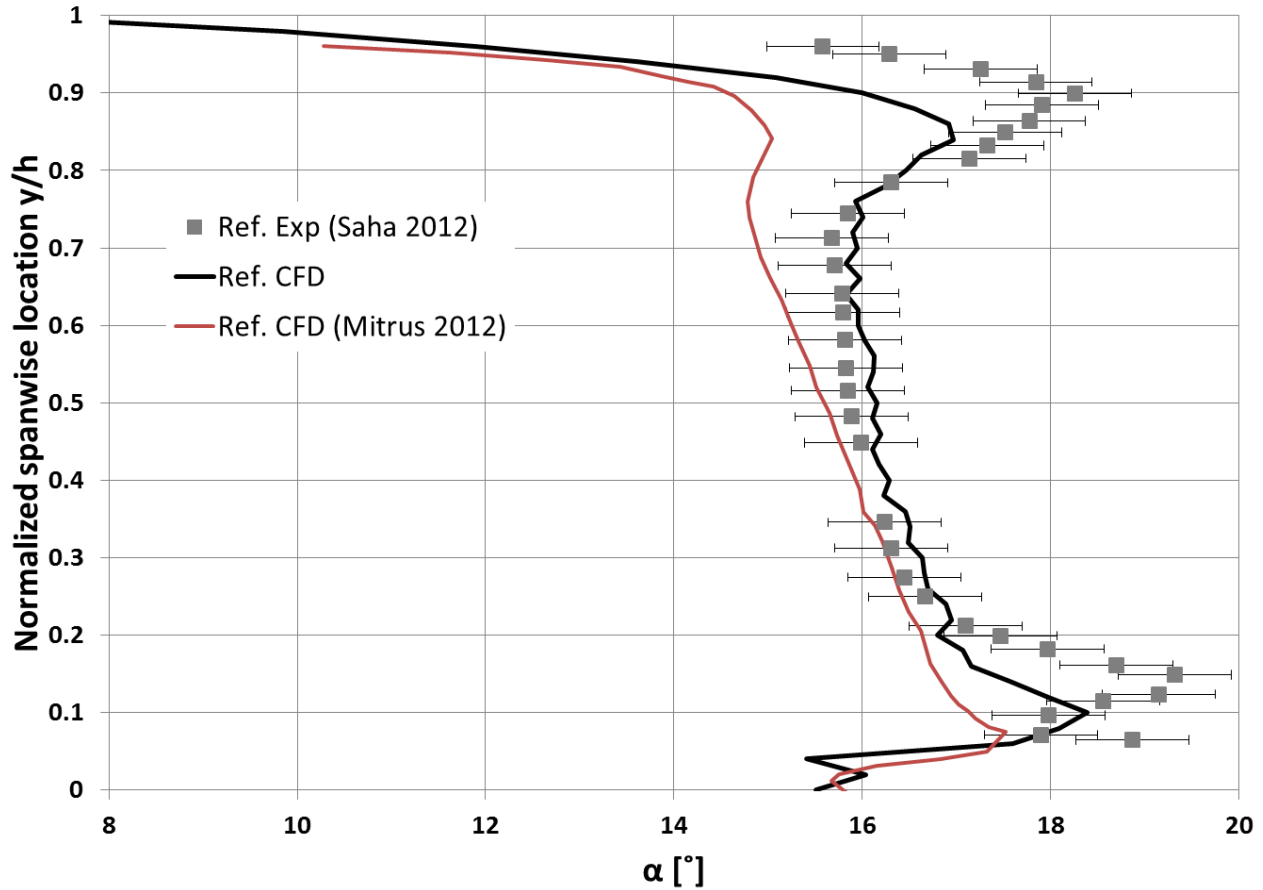


Figure 4-3 Uncooled (Reference) vane exit flow angle

Figure 4-3 shows exit flow angle experimental measurements and CFD calculations of the author and that of Mitrus (2012). In her work Mitrus (2012) used the same geometry and boundary conditions as the author. The only difference in this work and that of Mitrus's is the numerical grid. The exit flow angle (x-axis) is plotted against normalized spanwise location (y-axis). The flow –driven by endwall flows- tends to turn less in the endwall regions with large deviation at the outer bounds of the BL region (around 15% spanwise location). The present CFD simulation was able to capture the experimental values well within the 0.6° measurements uncertainty except for some deviation near the endwalls (0-5% and 90-100% spanwise location). Endwalls are specially challenging for CFD simulation to model for the adverse pressure gradient of boundary layer at them.

4.1.4. Vorticity and total pressure distribution

One very distinctive flow phenomena associated with flow in vanes is vortices. The axial component of vorticity ω_x is calculated as:

$$\omega_x = \frac{\partial w}{\partial y} - \frac{\partial v}{\partial z} \quad \text{Eq. 4-2}$$

Figure 4-4 is a representation of the vortex structure at vane exit ($107.1\% C_{ax,hub}$). The CFD simulation (b) was able to capture the main features of the vortex structure measured in the experiment (a). The TE shed vortex extends from 15% to 90% normalized spanwise location. The

corner and passage vortices were located at the correct spanwise location although with much smaller value than the experimental. On the other hand, an over prediction of the horseshoe vortex is evident.

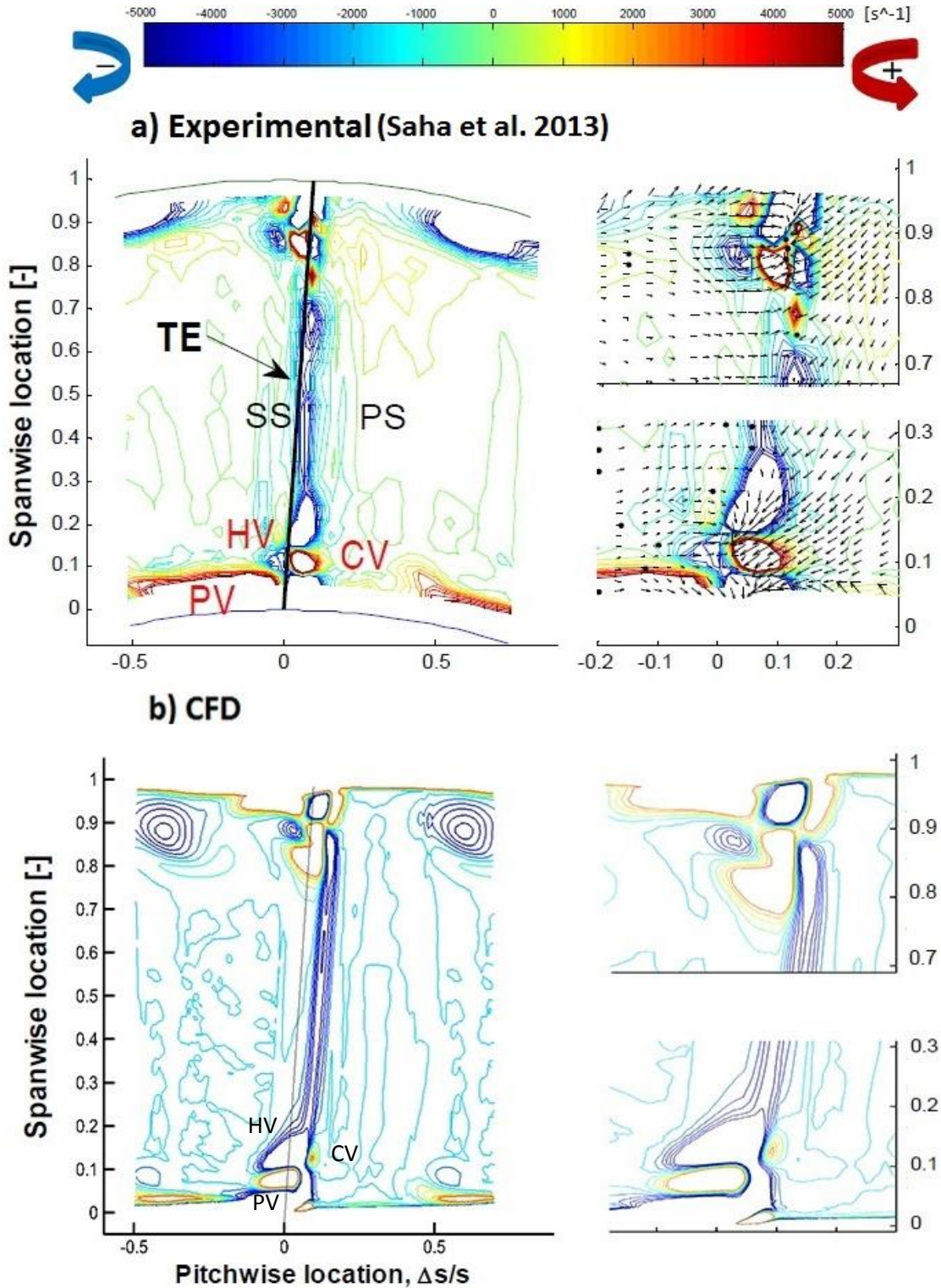


Figure 4-4 Ref. case vorticity at 107.1% $C_{ax,hub}$

To trace how the vortex structure at the TE is formed, a series of planes of the vortex are shown in Figure 4-5 at different stations in the passage. The vortex is scaled from -5000 s^{-1} (blue) to 5000 s^{-1} (red) just like Figure 4-4. The plots show how the flow starts to roll away from endwalls at passage entrance. Two opposing flows are colliding here, one is the endwall moving from pressure to suction side by mean of pressure gradient, while a flow separated at LE is impelling in the opposite direction on the suction side.

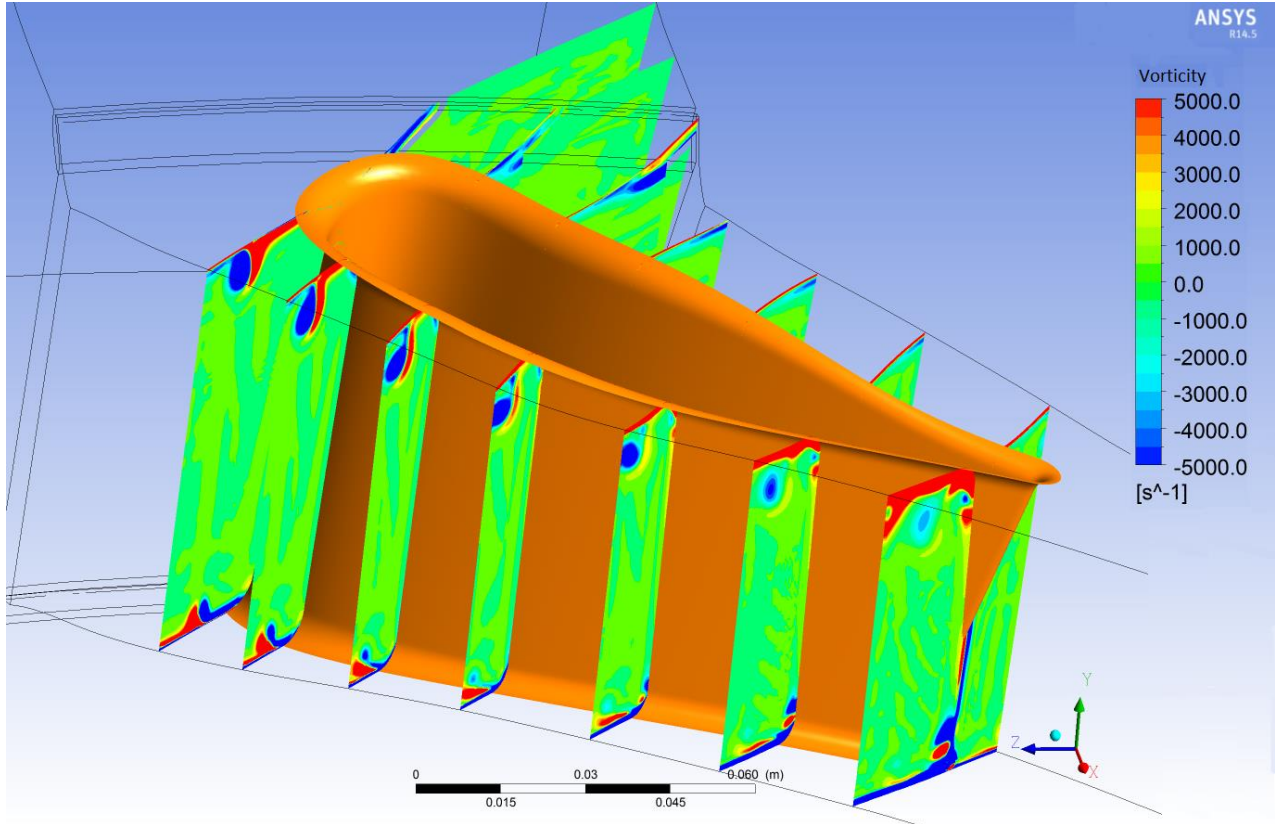


Figure 4-5 Vortex formation and evolution in vane passage

Figure 4-6 shows that opposing effect. Taken at LE, the separation (and springing of HS vortex) is dominant and can be seen clearly in the arrows repelled from blade SS. And it always flow away from endwalls and into profile, it has positive sense of rotation at casing and negative rotation at hub.

The previously mentioned opposing flows are better emphasized in Figure 4-7.

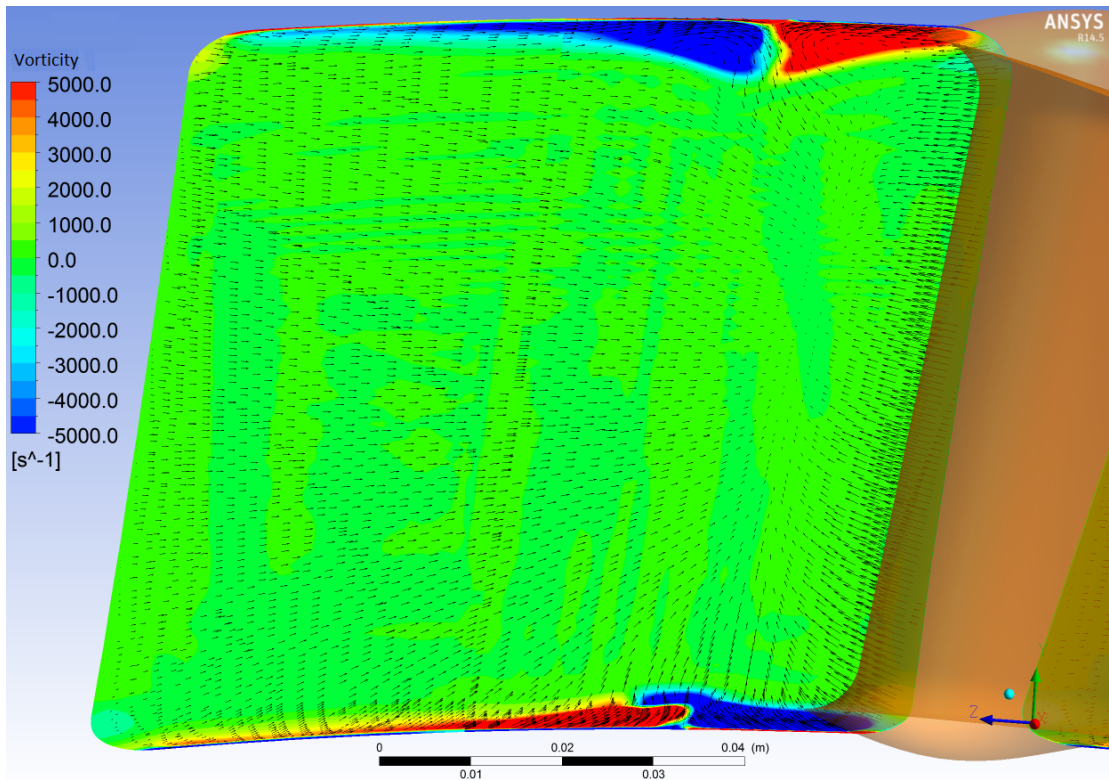


Figure 4-6 Vortex structure at LE

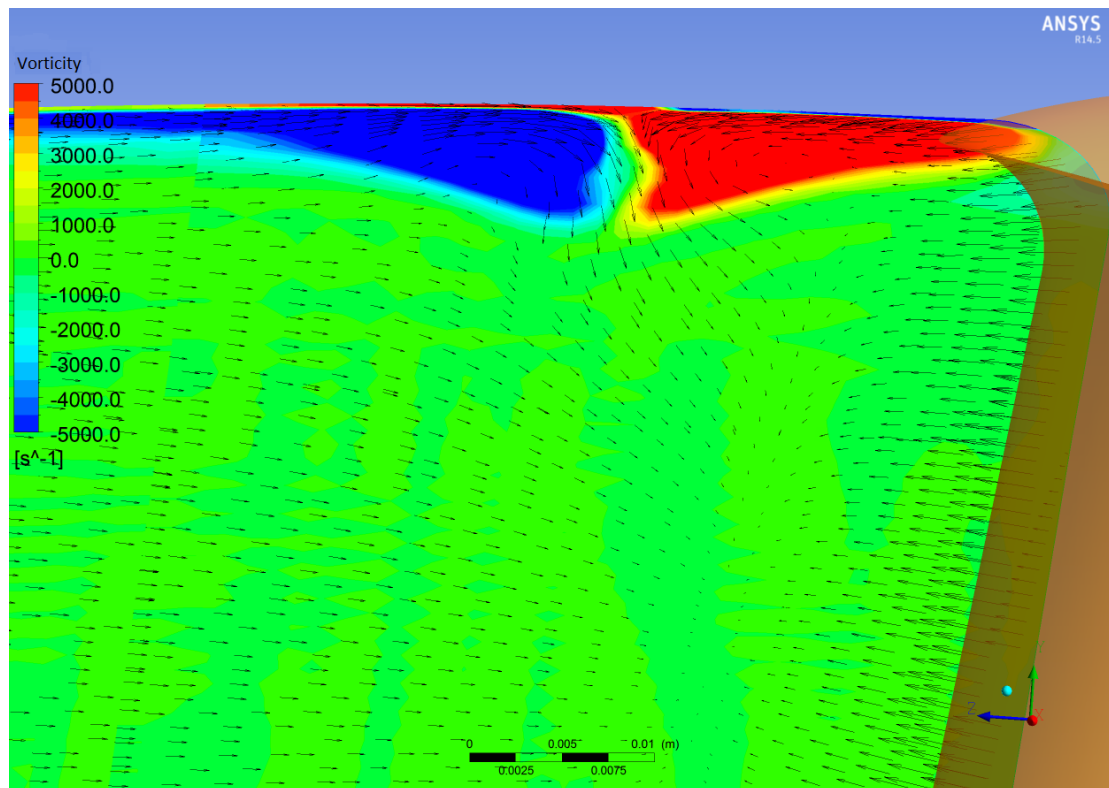


Figure 4-7 Vortex upstream at casing

A measure of the total pressure loss is the total pressure coefficient C_p which is defined as:

$$C_p = \frac{P_{1,mid} - P_2}{P_{1,mid}} \quad \text{Eq. 4-3}$$

The total pressure coefficient contours of the CFD simulation and experimental measurements show in Figure 4-8 highlights the agreement of the CFD simulation to the experimental measurements.

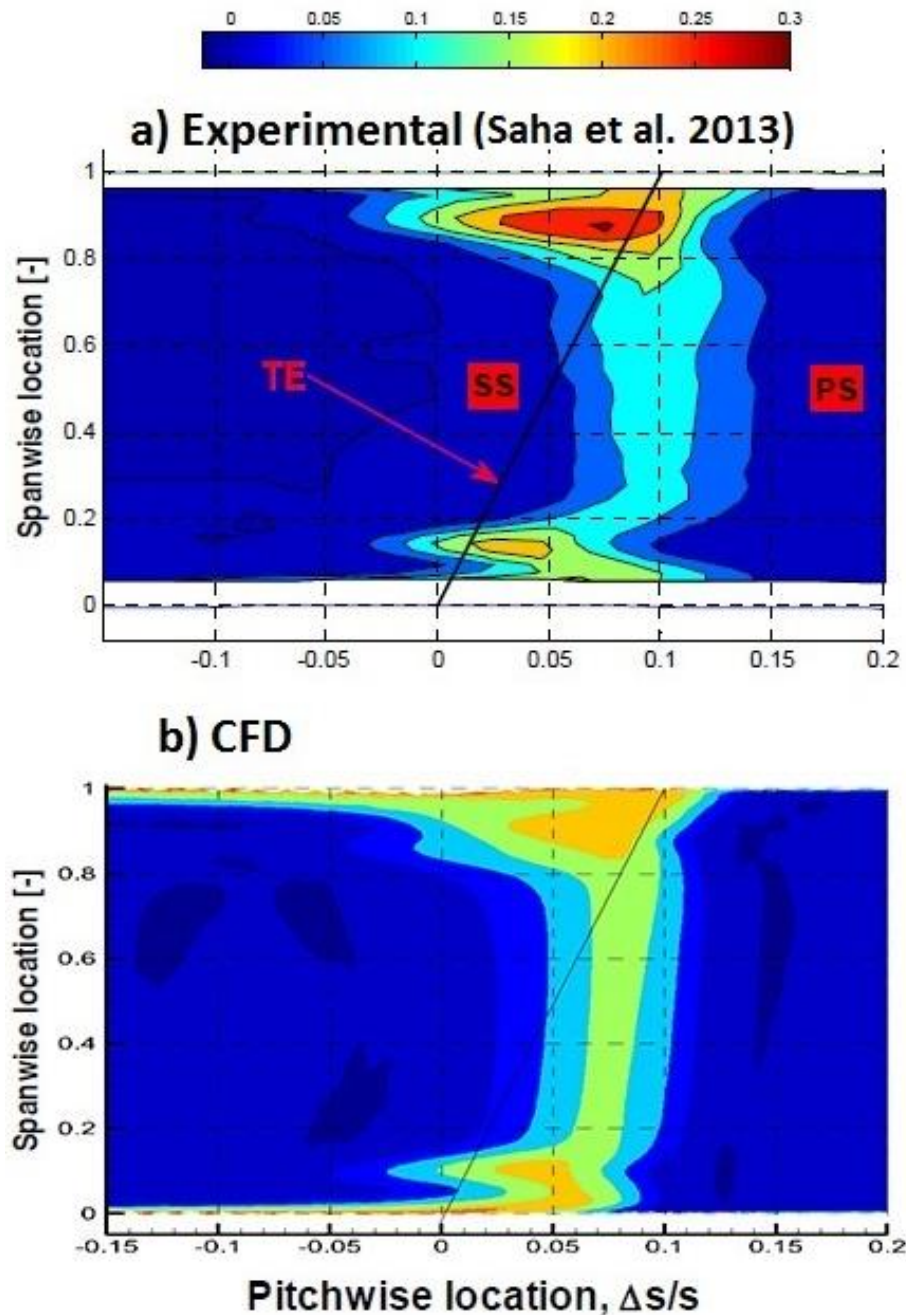


Figure 4-8 Total pressure coefficient

The total pressure coefficient shows correspondent behavior to the exit flow angle variation, as C_p increases with decrease of the total pressure downstream of the vane, an increase in the flow turning accompanies it indicating higher intensity evident of the of the passage vortex, and vice versa. It is obvious that virtually no pressure drop occurs in the vane passage, and the all of the loss can be seen between -0.05 and 0.15 normalized pitchwise locations, influenced by the trailing edge (TE) shed vortex downstream of the TE, with an increase of the loss value at endwalls specially at the casing, caused by the secondary flows.

4.1.5. Aerodynamic loss

The aerodynamic loss is the flow parameter that interprets all flow phenomena in the vane passages. The design criterion of vane profile is maximum lift (which is interpreted into work) at minimum drag (loss). The loss has many definitions; in this study a definition of the K.E. loss is chosen which is defined as:

$$\zeta = \frac{\text{Actual Exit K.E.}}{\text{Isentropic K.E. of mainstream}} \quad \text{Eq. 4-4}$$

$$\zeta = \frac{\left(\frac{P_{2s}}{P_2}\right)^{\frac{k-1}{k}} - \left(\frac{P_{2s}}{P_1}\right)^{\frac{k-1}{k}}}{1 - \left(\frac{P_{2s}}{P_1}\right)^{\frac{k-1}{k}}} \quad \text{Eq. 4-5}$$

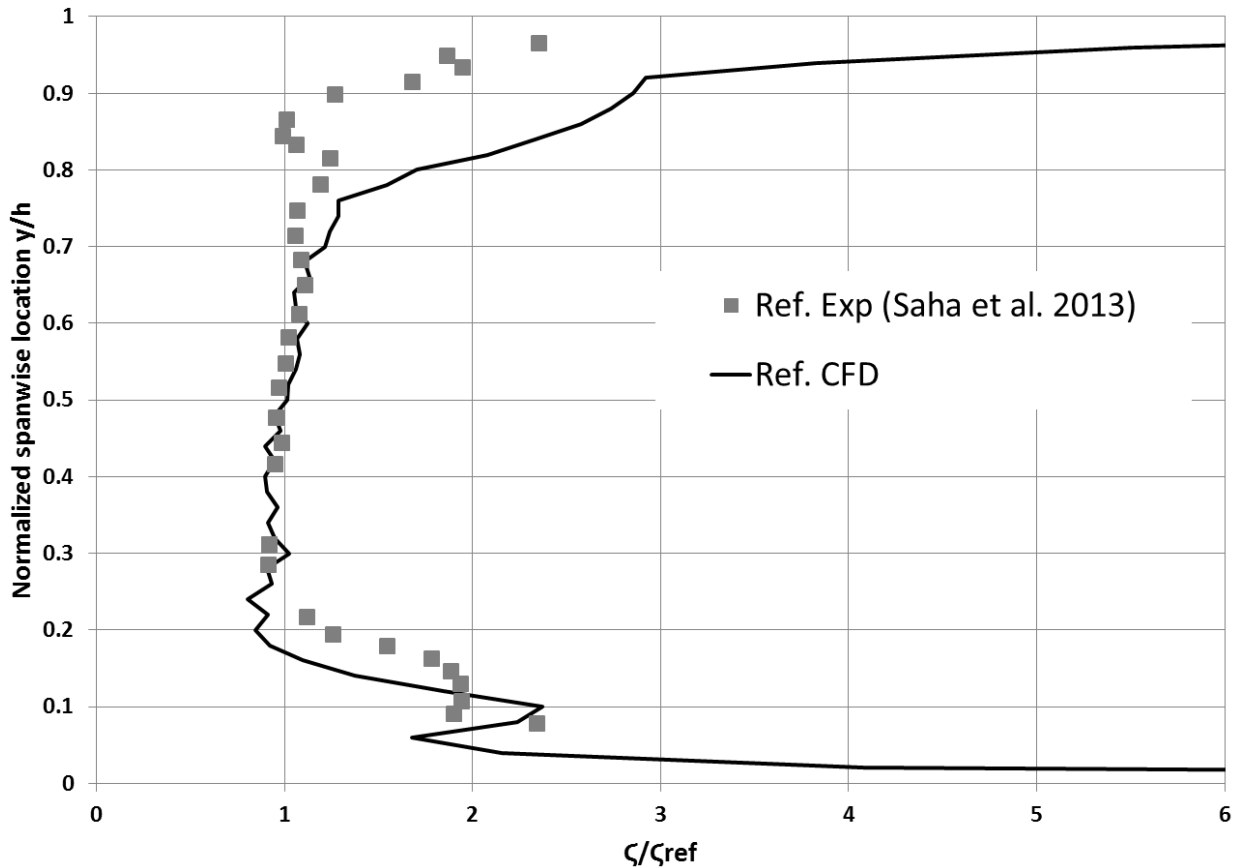


Figure 4-9 Normalized mass averaged kinetic energy loss at 107.1% $C_{ax,hub}$

The mass averaged normalized KE loss is shown in Figure 4-9 at different spanwise location and is showing good agreement of the CFD simulation with the experimental measurements. The value is normalized by the KE loss average at midspan (40:60% normalized spanwise location). It is evident that the KE loss curve is asymmetric around midspan, i.e. showing different behavior at hub and casing. From the KE loss equation (Eq. 4-5) the driving variable is the static pressure, looking at the average static pressure distribution in the spanwise location This is due difference in the static pressure is higher at casing than hub as it can be seen in Figure 4-10.

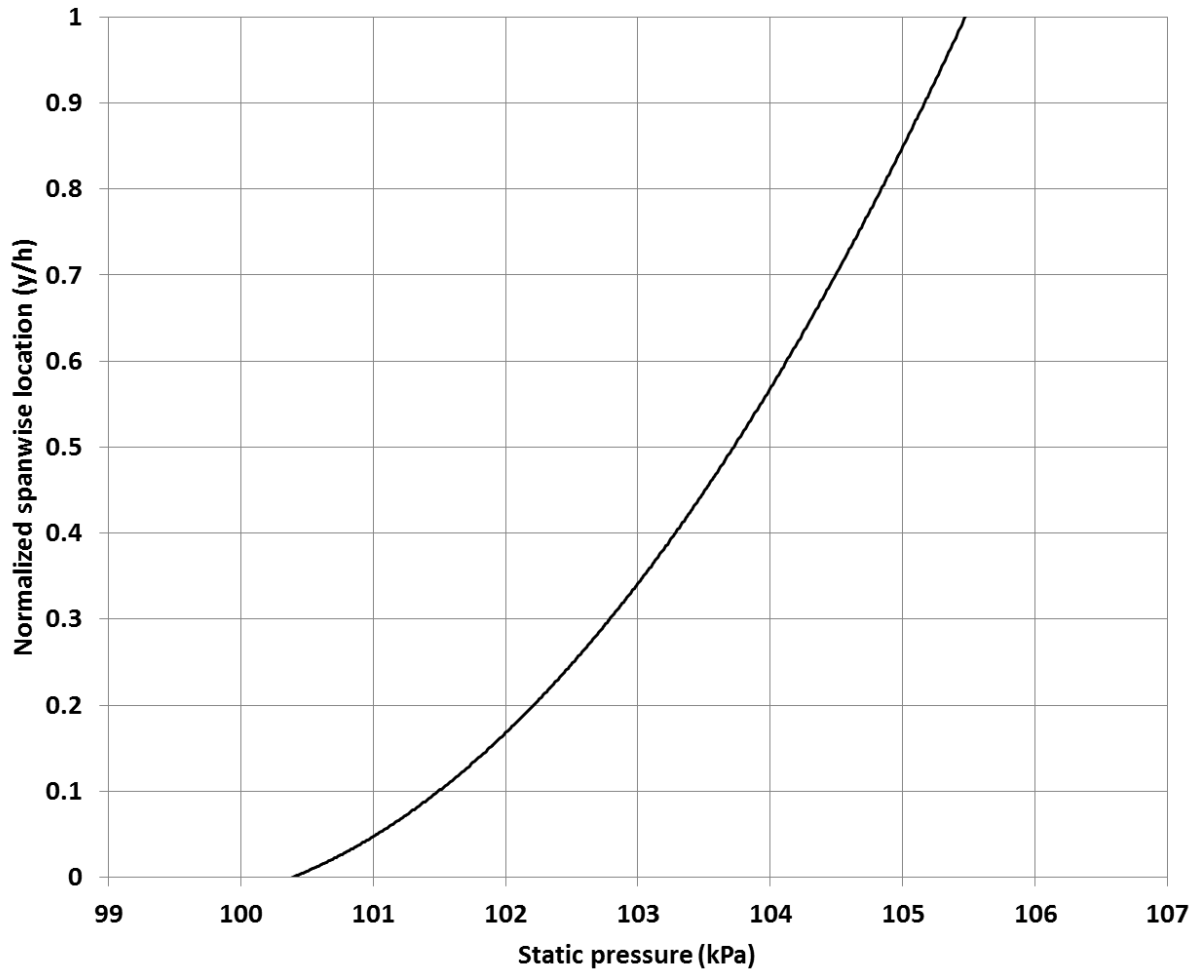


Figure 4-10 Mass averaged static pressure trend line at 107.1% $C_{ax,hub}$

This occurrence is explained by the equation:

$$\frac{dP}{dr} = \rho \frac{v^2}{r} \quad \text{Eq. 4-6}$$

It elaborates how the flow in a between two curves surfaces tends to move away from the convex and towards the concave surface. Due to lower flow velocity at the larger radius of curvature surface (casing in this case) results in a higher pressure at the location and the opposite goes for the smaller radius of curvature surface (hub).

Povey et al. (2007) have shown that effect in their work, Figure 4-11 is their illustration of the flow development through vane passage.

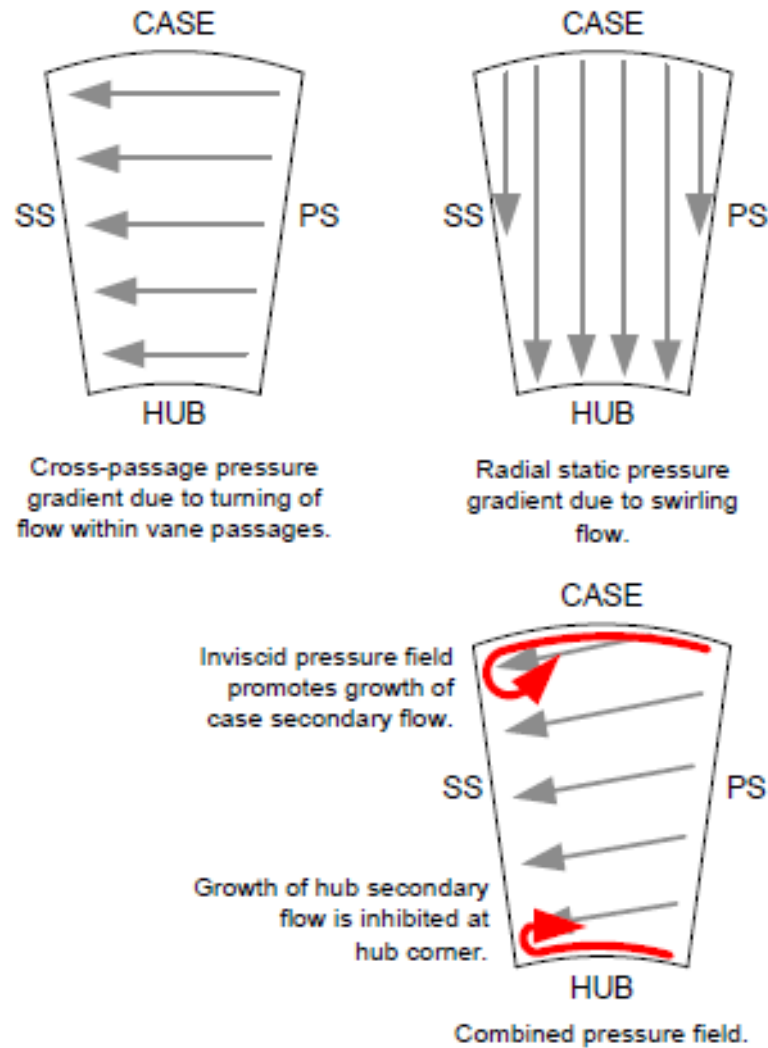


Figure 4-11 Flow development in vane passage (Povey et al. 2007)

The CFD simulation of the uncooled (reference) vane has shown consistent agreement with the experimental measurements, supporting its validity for use in latter stages of the research – cooled vane-. However, before proceeding with the cooled vane, a simplified analogues problem will be solved. The next section will discuss the results of CFD simulation of flat plate film cooling and compare it to experimental measurements from El-Gabry et al. (2011) and Thurman et al. (2011).

4.2. Flat plate film cooling

This work is objected towards validating a new approach in modeling film cooling for gas turbines analysis applications. As a step towards that, a simple problem is addressed to make a preliminary assessment of the used technique. Flat plate film cooling is a famous problem in the literature used to simulate the jet in cross flow situation. Experimental data from El-Gabry et al. (2011) and Thurman et al. (2011) was used to validate the new modeling technique.

4.2.1. Normalized flow velocity

For both CFD-tube and truncated, two runs were made, one for high blowing ratio ($BR = 2$) and one for low blowing ratio ($BR = 1$). Mainstream velocity is 9.1 m/s and constant speed (oriented at 30° with the flat plate) was applied at the hole. Figure 4-12 is the flow velocity in the mainstream direction (u) normalized by the mainstream velocity (9.1 m/s) for $BR = 1$ and $BR = 2$. Both the horizontal and vertical axes are normalized by the cooling hole diameter.

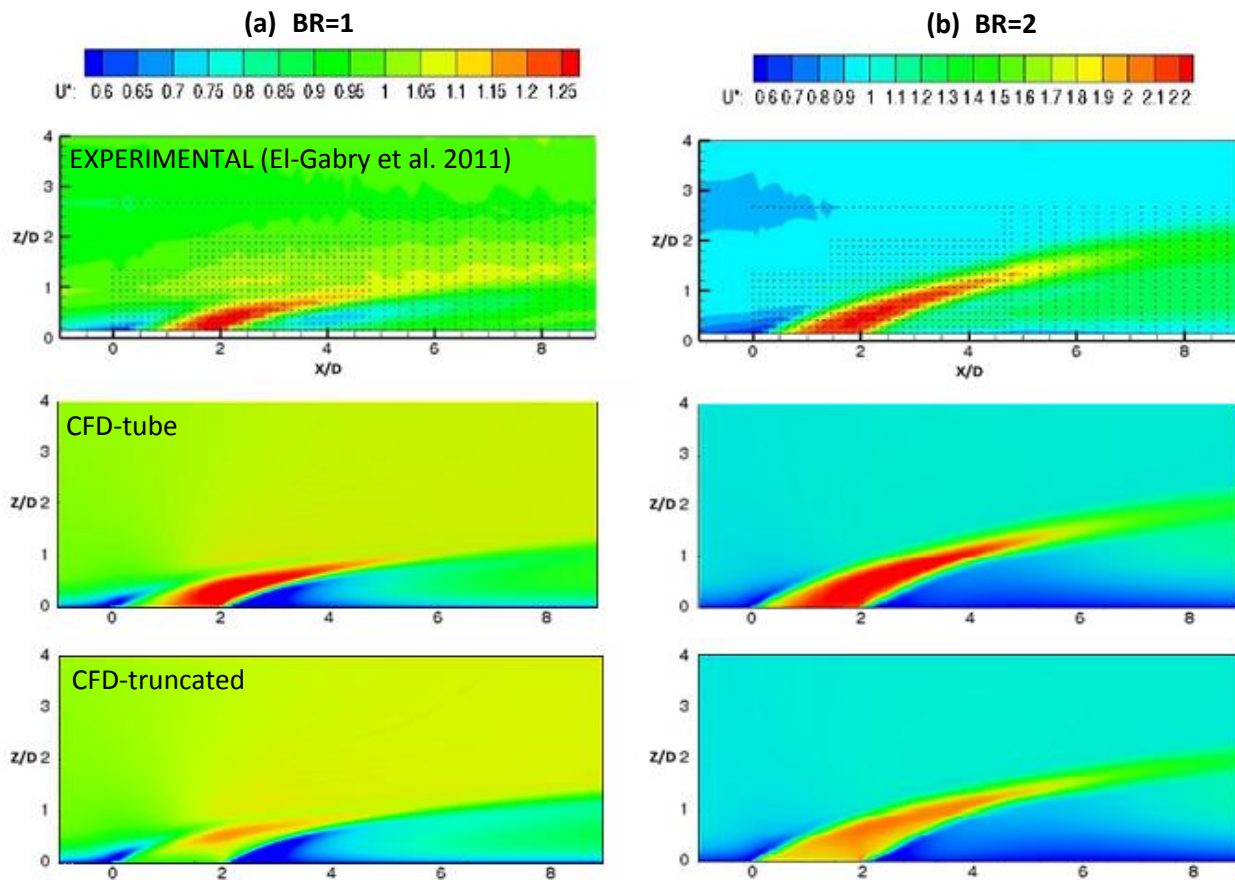


Figure 4-12 u -velocity normalized contours ($BR=1$ and $BR=2$)

The CFD run with coolant tube looks more similar to the experimental measurements; a distinctive coherence of the coolant flow is obvious, especially at its wake, on the contrary, in the run with no tube, the coolant flow loses intensity near the wake and showing more diffusive behavior than experiment. And the same trend is observed for the high blowing ratio ($BR=2$).

Figure 4-13 is a representation of the normalized temperature (theta) contours for BR=1 and 2, where theta is calculated as:

$$\theta = \frac{T_{\infty} - T}{T_{\infty} - T_c} \quad \text{Eq. 4-7}$$

Where:

T_{∞} : Mainstream temperature = 295 K

T: Temperature

T_c : Coolant temperature at hole exit = 273 K

4.2.2. Flow field temperature along centerline

Qualitatively, both CFD tube and truncated are within the measured experimental values of θ for both BR=1 and BR=2. With one major difference in the low BR, that is, the thermal bound of the coolant seem to be higher than experimental. In the experiments, the coolant effect on the mainstream temperature barely touches $Z/D = 1.5$. While in the CFD simulation (both case1 and case2) the coolant effect can be well observed beyond the $Z/D = 1.5$ limit. However the same is not true for the higher BR. In which calculated θ from CFD is at $Z/D = 2.5$ just like experimental measurements. Yet on the other hand, an over prediction of the coherence of θ is evident for both case1 and case2. Suggesting more penetration of the coolant jet, causing the jet to be more detached from the surface than experiments. As a direct result of the previous, the mainstream entrainment in the wake of the jet occurred.

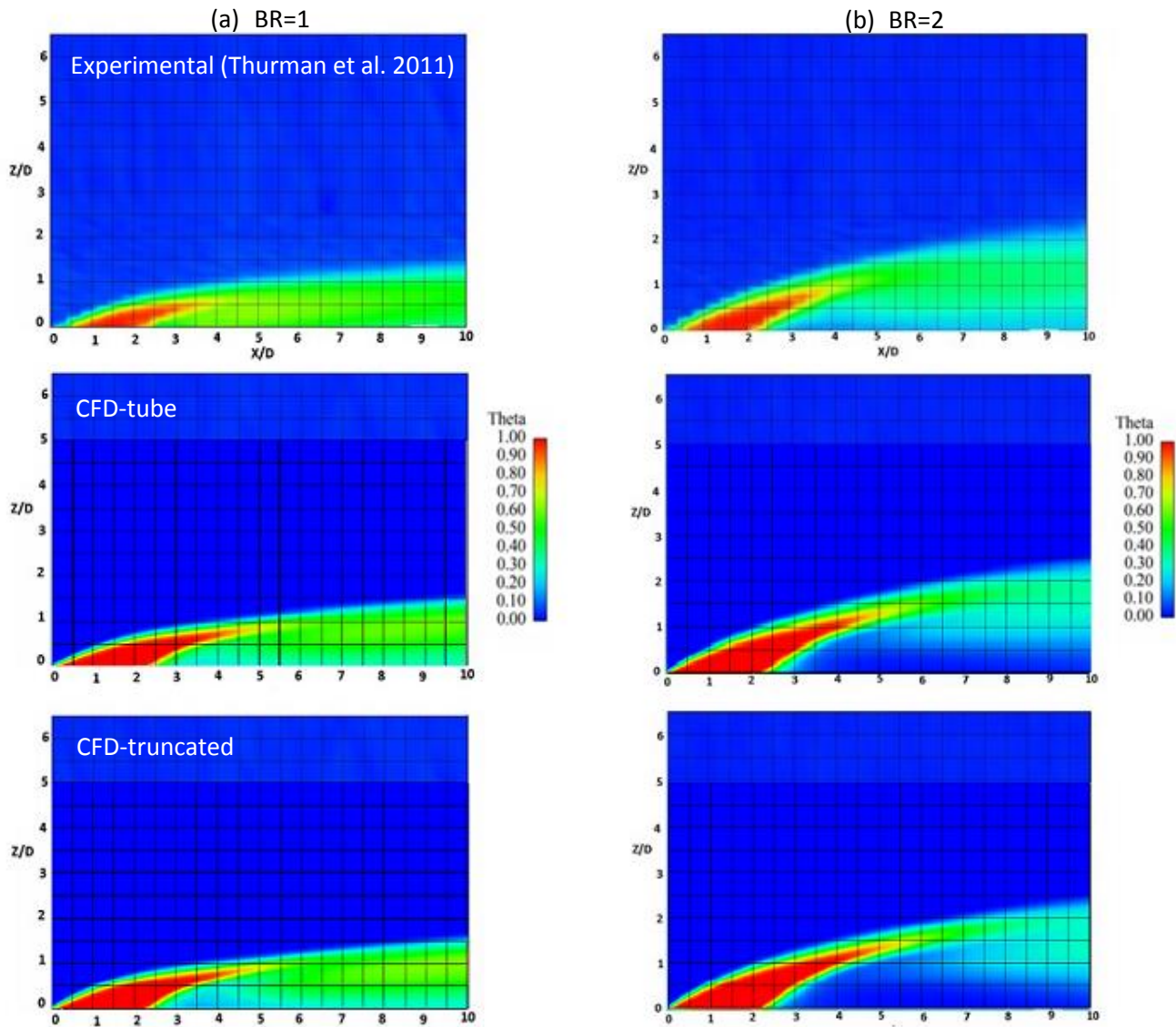


Figure 4-13 Theta contours (BR=1 and BR=2)

The contours of θ for BR=1 shown in Figure 4-14 highlight both the previously noted higher excessive penetration and mainstream entrainment in the jet wake. The excessive penetration is evident in the traversed contour levels, while the higher value contour level (0.7) in the jet wake is caused by mainstream penetration of the coolant jet. While deviated from the experimental measurements, both case1 and case2 remain similar, suggesting no merit of solving the flow in the coolant pipe. An isometric view of the '0.7' contour level is shown in Figure 4-15 showing how the mainstream penetrates through the coolant jet.

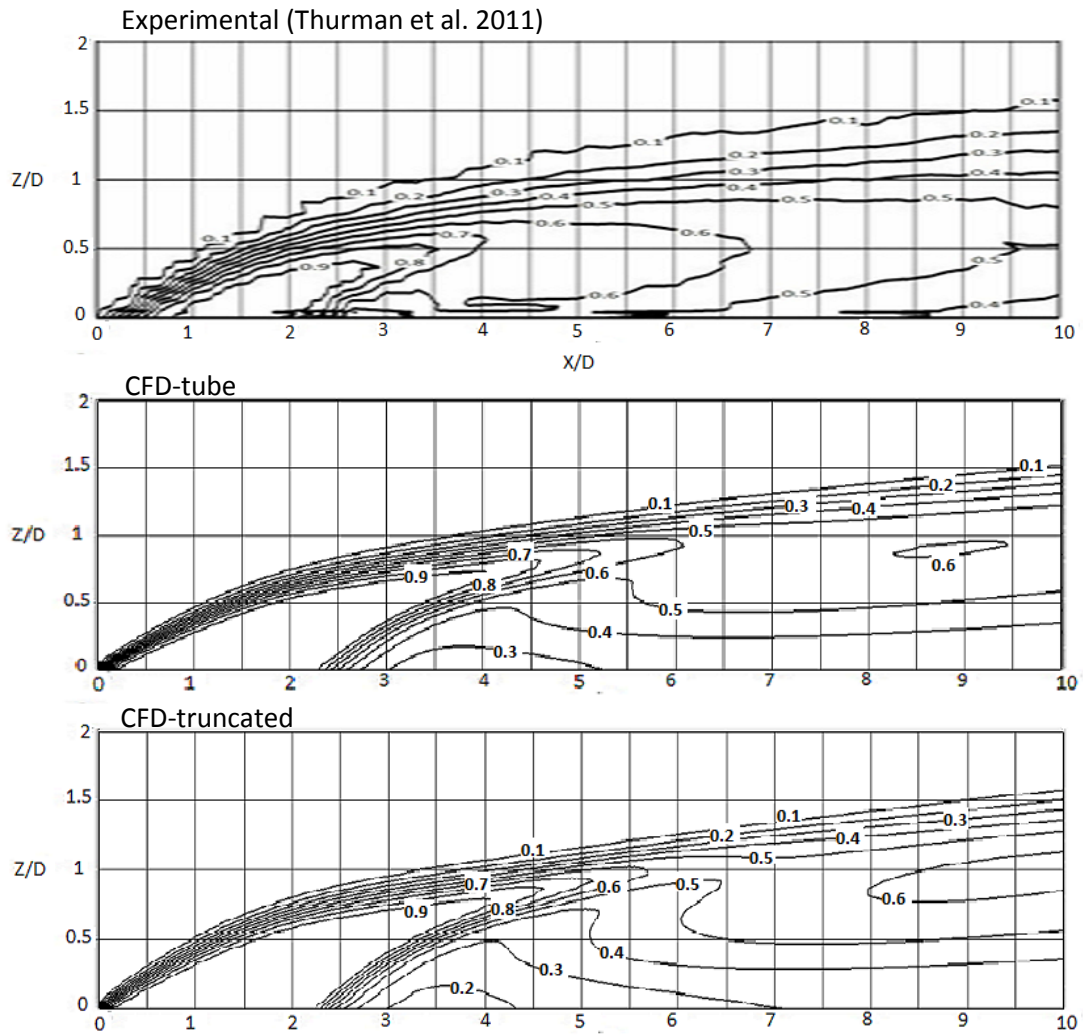


Figure 4-14 Theta contours (BR=1)

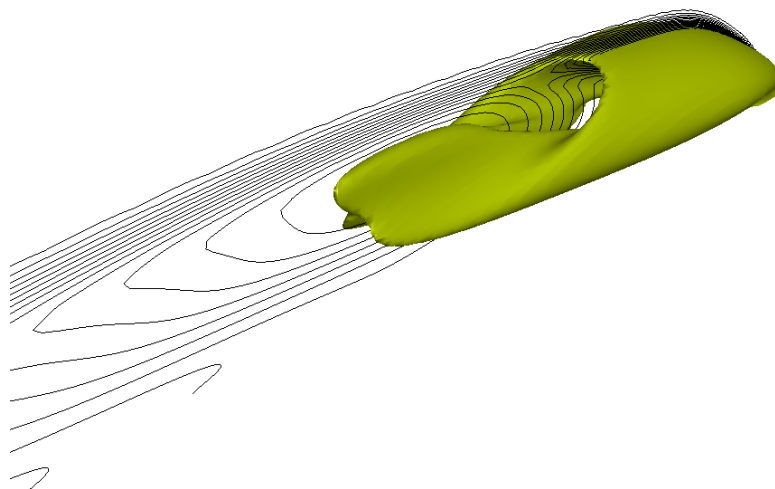


Figure 4-15 Mainstream entrainment in the coolant jet wake

The higher BR cases behave similar to the lower BR cases. With the excessive coolant penetration present while the mainstream penetration in the coolant jet wake was absent in the CFD-tube.

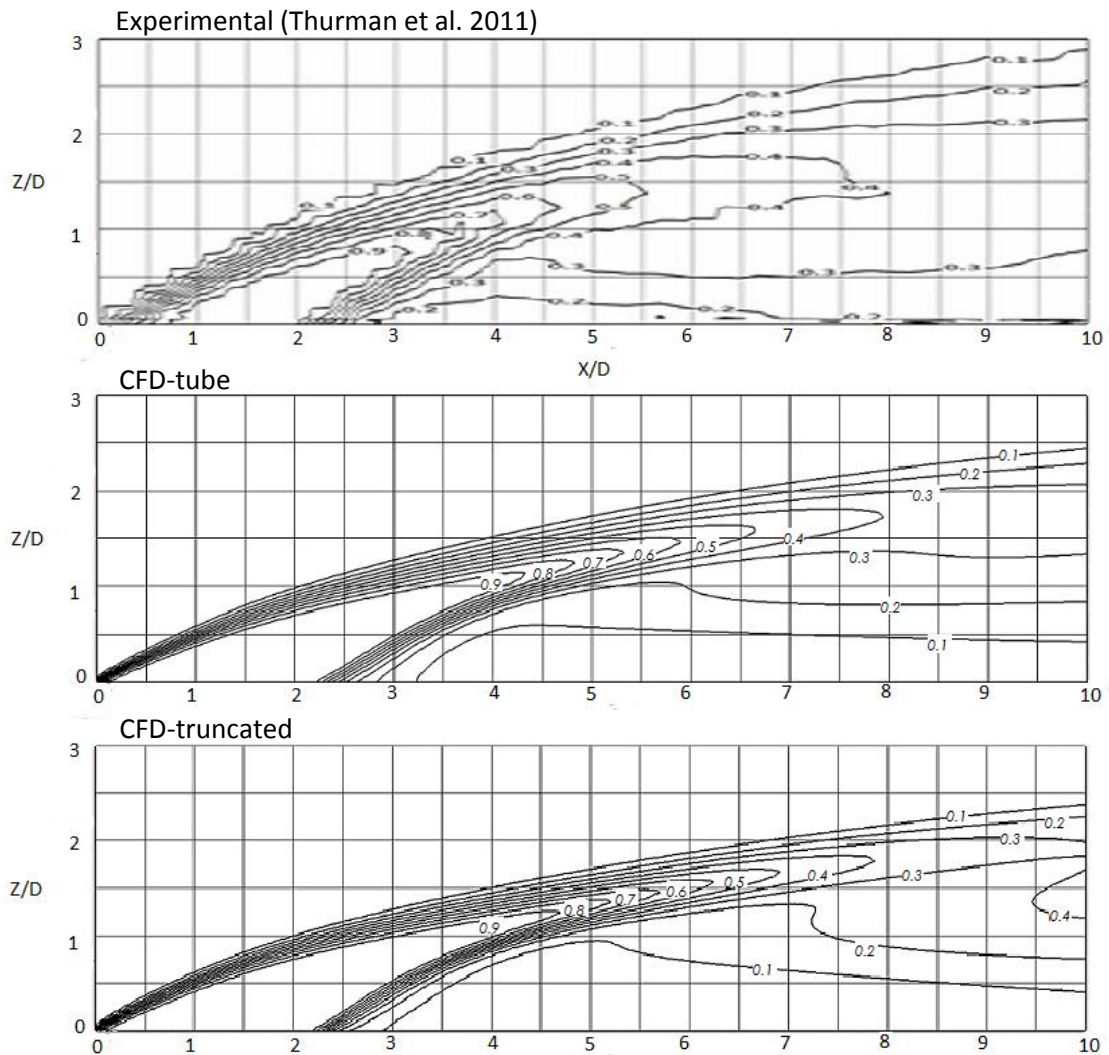


Figure 4-16 Theta contours (BR=2)

4.2.3. Film cooling effectiveness

Film cooling effectiveness (η) is (as the name suggests) a parameter used to judge on the effectiveness of applying film cooling on a surface. Where:

$$\eta = \frac{T_{\infty} - T_{aw}}{T_{\infty} - T_c} \quad \text{Eq. 4-8}$$

It provides quantitatively an assessment of the effect of film cooling on reducing the temperature of the targeted wall. While heat transfer between fluid and the cooled surface is out of the scope of this work. One finds it appropriate to mention all the findings of the analysis at each phase of research.

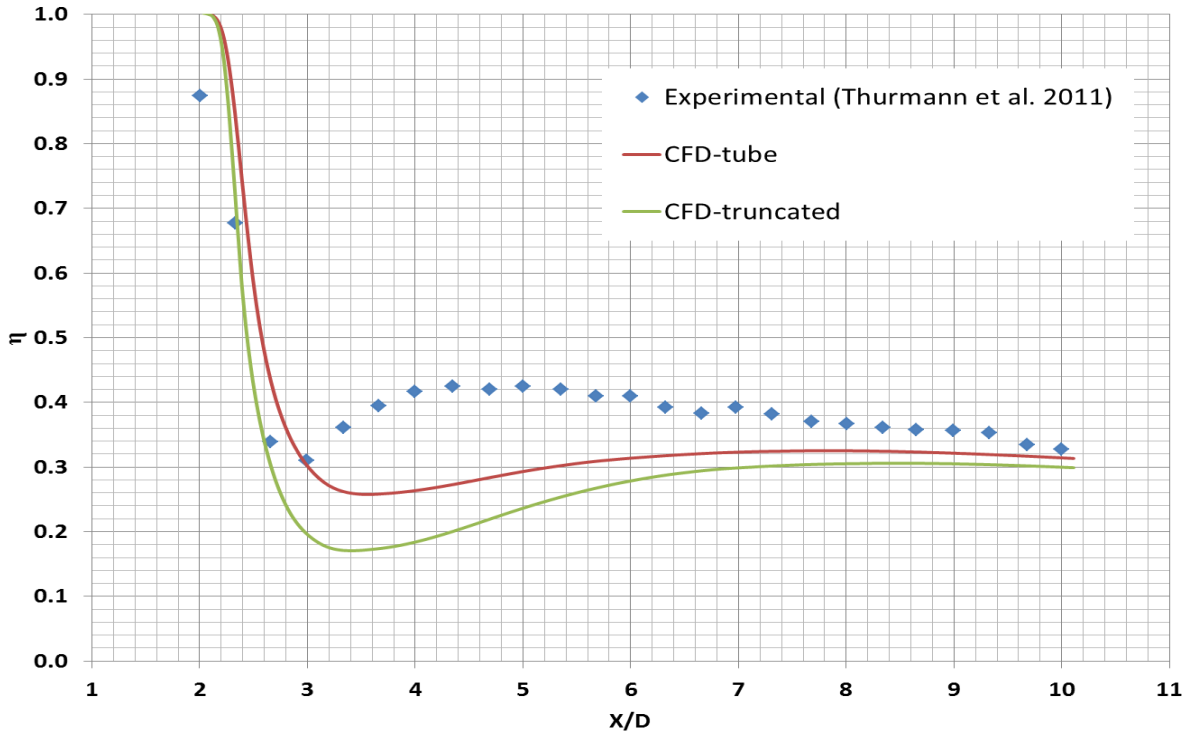


Figure 4-17 η at centerline downstream of the coolant hole (BR=1)

In the η chart (Figure 4-17) at centerline of the cooling hole and downstream of it for experimental and CFD tube and truncated, a direct effect of the excessive calculation of coolant penetration is observed in the lowered value of η close to the hole exit. As the coolant moves further downstream, it reattaches to the plate surface increasing η and bringing the CFD simulation close to the experimental measurements.

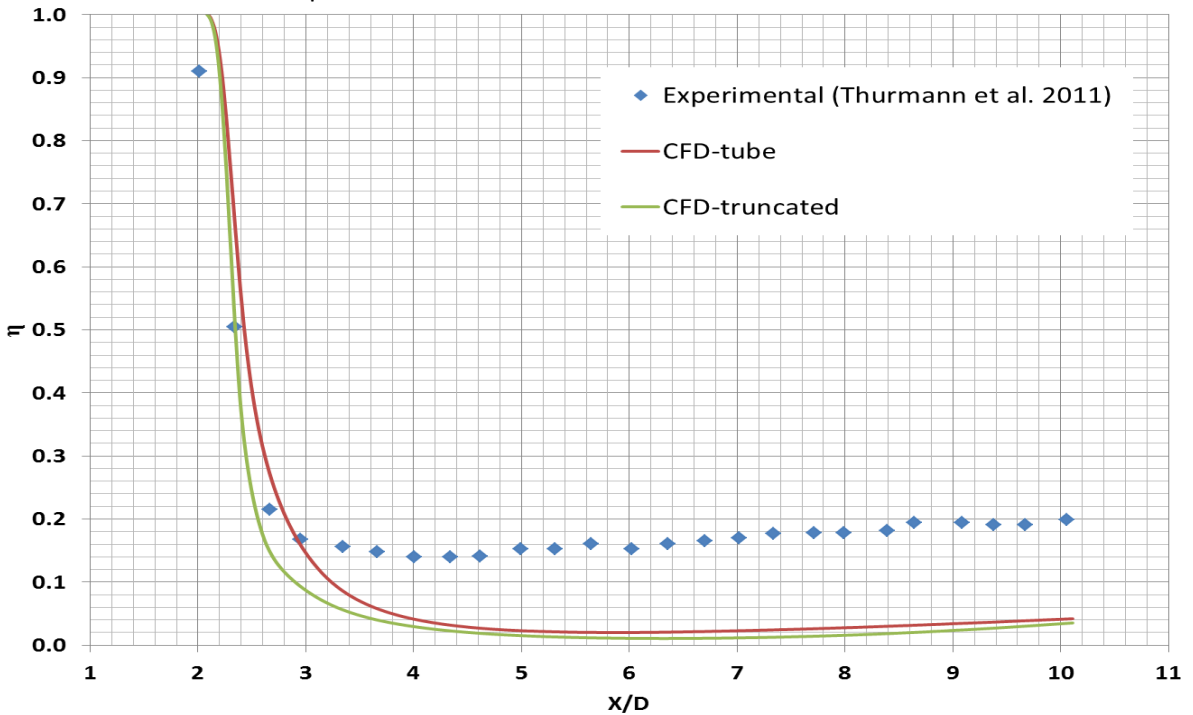


Figure 4-18 η at centerline downstream of the coolant hole (BR=2)

On the other hand for higher BR, the coolant jet doesn't reattach (Figure 4-18), leading to less accurate calculation of η all the way downstream. However, far downstream of the hole exit, both CFD cases coincide on each other. Supporting the previously reached conclusion that modeling the flow in the pipe doesn't provide any advantage over sparing it and applying a velocity BC directly at the hole surface.

To investigate that more in depth, looking at the jet from downstream (Figure 4-19) it is noted that starting at $X/D = 6$ both CFD-tube and CFD-truncated are similar with mere slight difference. Also it is noted that both CFD approaches did capture the famous kidney vortex associated with jet in cross flow injection formed downstream of the cooling hole.

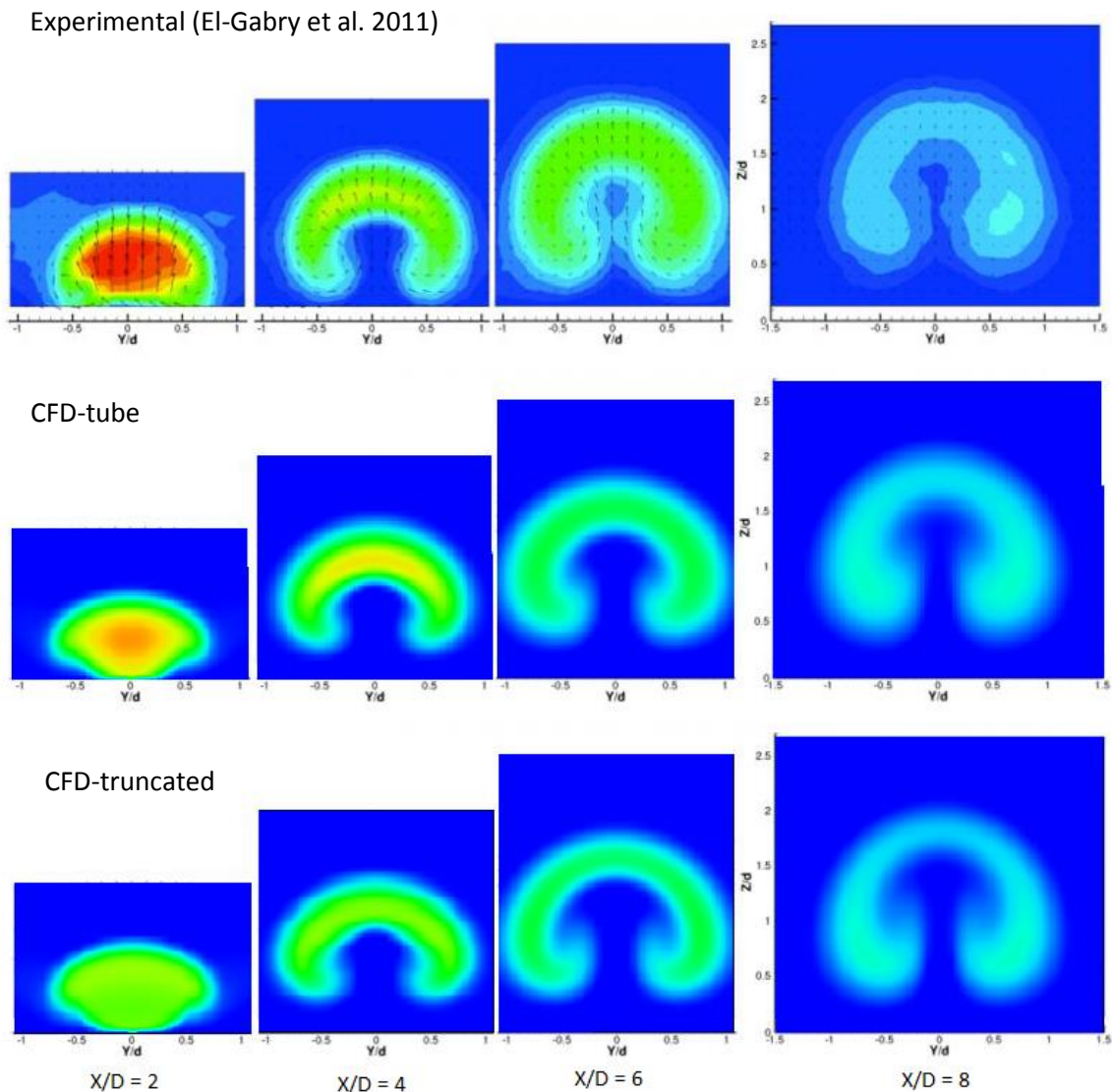


Figure 4-19 Normalized u-velocity downstream cooling hole

4.3. Cooled vane

The cooled vane numerical simulation is presented for two configurations. Configuration 1 is at 3 different locations, 2 on the suction side and one on the pressure side, with one of the suction side location and pressure side are analyzed at 3 different BR. Configuration 2 is showerhead cooling for 2 BR cases.

4.3.1. Configuration 1 (Pressure side and suction side)

The third phase of this work is the numerical simulation of partially cooled vane. The same vane geometry from section 4.1 was used and coolant flow was applied at three different locations as highlighted in Figure 4-20.

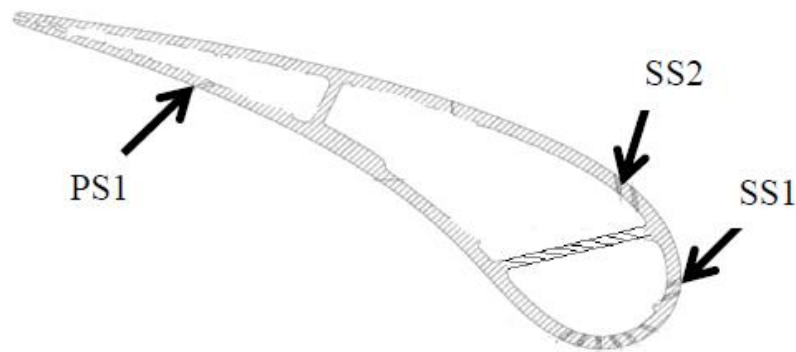


Figure 4-20 Film cooling holes locations (Saha et al. 2013)

Two of the cooling locations are on the suction side (SS1 and SS2) and one on the pressure side (PS1). Both SS1 and SS2 locations has two rows of cooling holes, while PS1 has only one row. The correspondent specifications of the cooling holes are listed in Table 4-1. The holes angles are measured from tangent to the vane surface at the hole exit.

Table 4-1 Cooling holes geometrical information (Saha et al. 2013)

Row	X/C _{ax}	Angle [°]	No. of holes
PS1	77%	142.8	23
SS1	19%, 23%	50.9, 59.3	24 and 23
SS2	50%, 52%	42.3, 38.9	23 and 22

The same approach previously described in introducing the coolant flow into the domain for the flat plate was used. Figure 4-21 shows coolant holes connection to the vane surface.

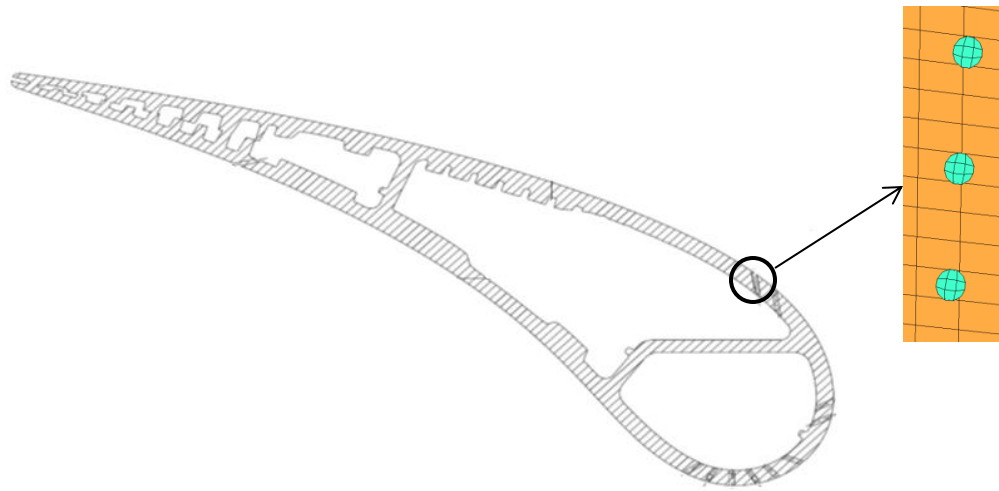


Figure 4-21 Film cooling holes

A set of runs for different BR for both PS1 and SS1 cooling locations were conducted according to Table 4-2. One is nominal mass flux ratio (Y), one low and one high. While for SS2 cooling location only one nominal case was run.

Table 4-2 Cooled (configuration 1) runs matrix

	Mass-flux ratio (Y)	Blowing Ratio (BR)	Pressure ratio (P_m/P_c)
Ref. (uncooled)	0	-	-
PS1	$Y_{nom} = 0.35\%$	0.96	1.02
	$Y_{low} = 0.29\%$	0.8	1.04
	$Y_{high} = 0.91\%$	2.5	0.806
SS1	$Y_{nom} = 1.04\%$	1.4	0.86
	$Y_{low} = 0.59\%$	0.8	1.02
	$Y_{high} = 1.85\%$	2.5	0.61
SS2	$Y_{nom} = 0.81\%$	0.8	0.95

The film cooling is parameterized by blowing ratio (BR) which is defined as:

$$BR = \frac{\rho_c u_c}{\rho_m u_m} \quad \text{Eq. 4-9}$$

Whereas in this analysis both coolant and mainstream flows have same density, the blowing ratio becomes:

$$BR = \frac{u_c}{u_m} \quad \text{Eq. 4-10}$$

In the experiments, it is hard to measure accurately the flow velocity at the hole exits for both mainstream and coolant flows, hence a different parameter was used to identify different runs. Mass-flux ratio or ' Y ' is calculated from the mass flow ratio between coolant and mainstream, hence from equation 4-9:

$$BR = \frac{\rho_c u_c}{\rho_m u_m} = \frac{A_m}{A_c} \frac{m_c}{m_m} = \frac{A_m}{A_c} Y \quad \text{Eq. 4-11}$$

The same parameters used to validate the uncooled vane CFD simulation will be used for the cooled cases, namely, exit flow angle, vorticity, total pressure distribution and aerodynamic loss. A new definition of aerodynamic loss will be introduced that accounts for the KE added due to cooling application.

4.3.1.1. Exit flow angle distribution

Exit flow angle is ideally determined by the blade orientation angle (16.05° for this vane). Although that's the case is for ideal flow, in face, flow in vane passage is far from being perfect. The plots in Figure 4-22 are the data at TE plane, the vertical axes is the normalized spanwise location while the horizontal axes is the exit pitch-averaged exit flow angle. It can be seen that in region 30-70% spanwise location, the exit flow angle is roughly equal to the reference angle (16.05°), yet in the endwall regions, the flow tends to turn driven by endwall and secondary flows.

It can be concluded from the plots that introducing the cooling for all the cases (PS1, SS1 and SS2) didn't have significant effect on the flow. This is due to the relatively low flow rate of coolant compared to mainstream. Coolant mass flow rate ranges from 0.29% to 1.85% of the mainstream flow.

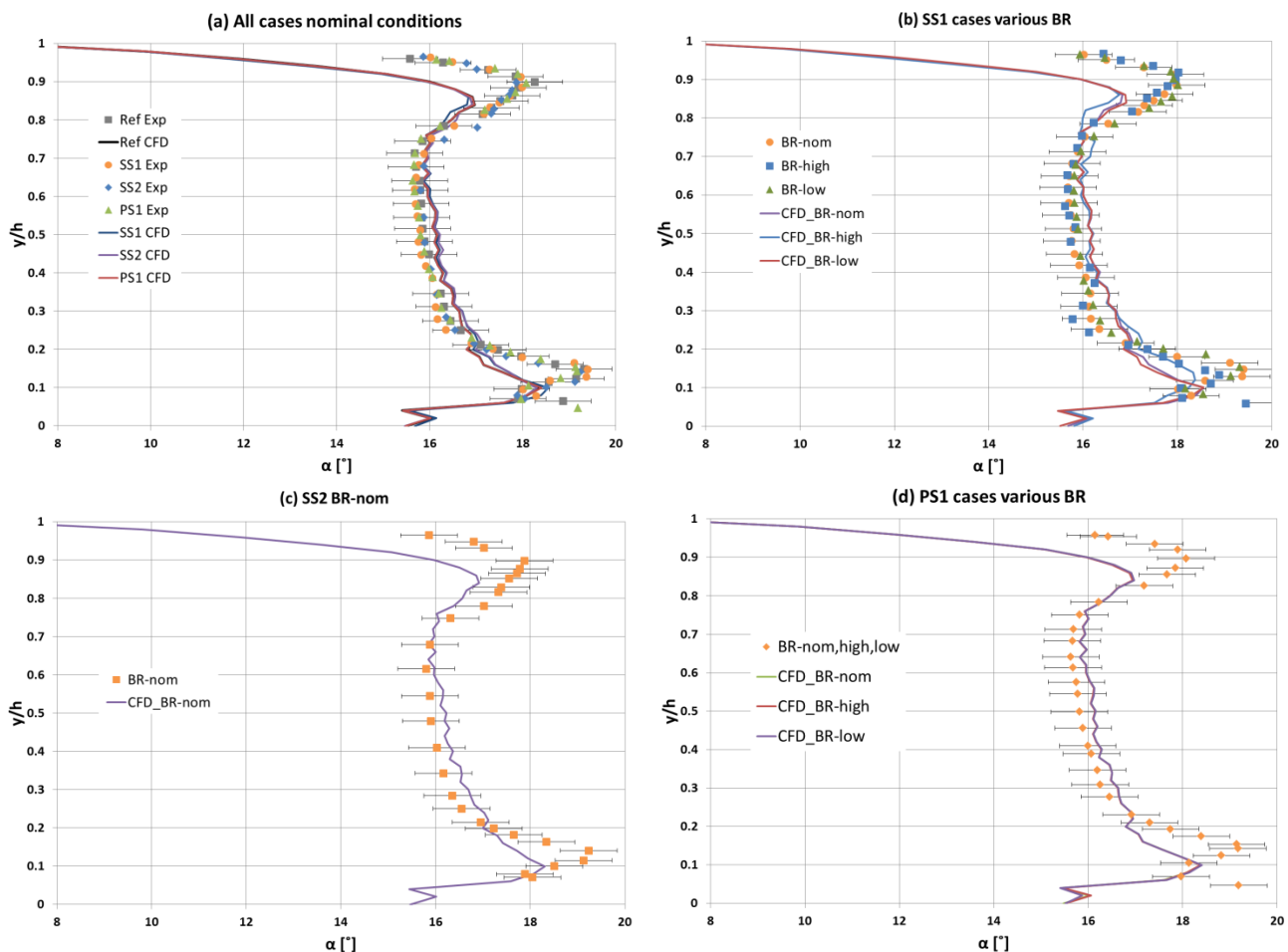


Figure 4-22 Pitch-averaged exit flow angle (Experimental data from Saha et al. 2013)

The CFD calculation of the exit flow angles was able to capture the measured experimental values accurately for all the cases (within the measurement uncertainty of 0.6°) especially outside the endwalls regions.

4.3.1.2. Vorticity and total pressure distribution

Same definition of vorticity mentioned before was used (Eq. 4-2). It can be noted from Figure 4-23 the interruption in the TE shed vortex at 28% span location compared to uncooled case (Figure 4-4) due to application of coolant, while same main structure of the vortex remain intact, namely, HS, PV and CV.

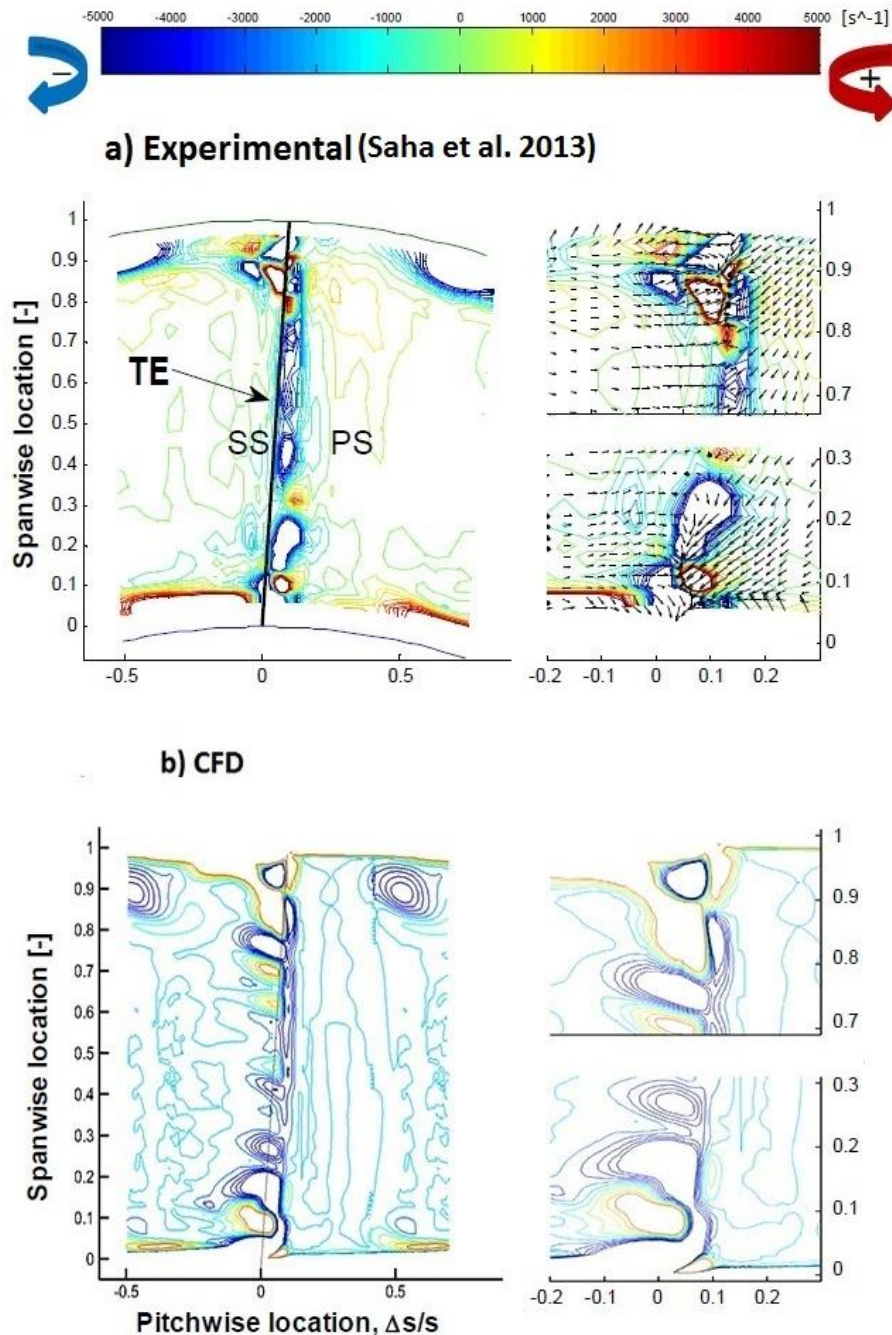


Figure 4-23 SS1 high BR case vorticity at 107.1% $C_{ax,hub}$ downstream

Total pressure coefficient (C_p) offers a good estimate of the overall loss through the passage by comparing change in total pressure at exit from the total inlet pressure.

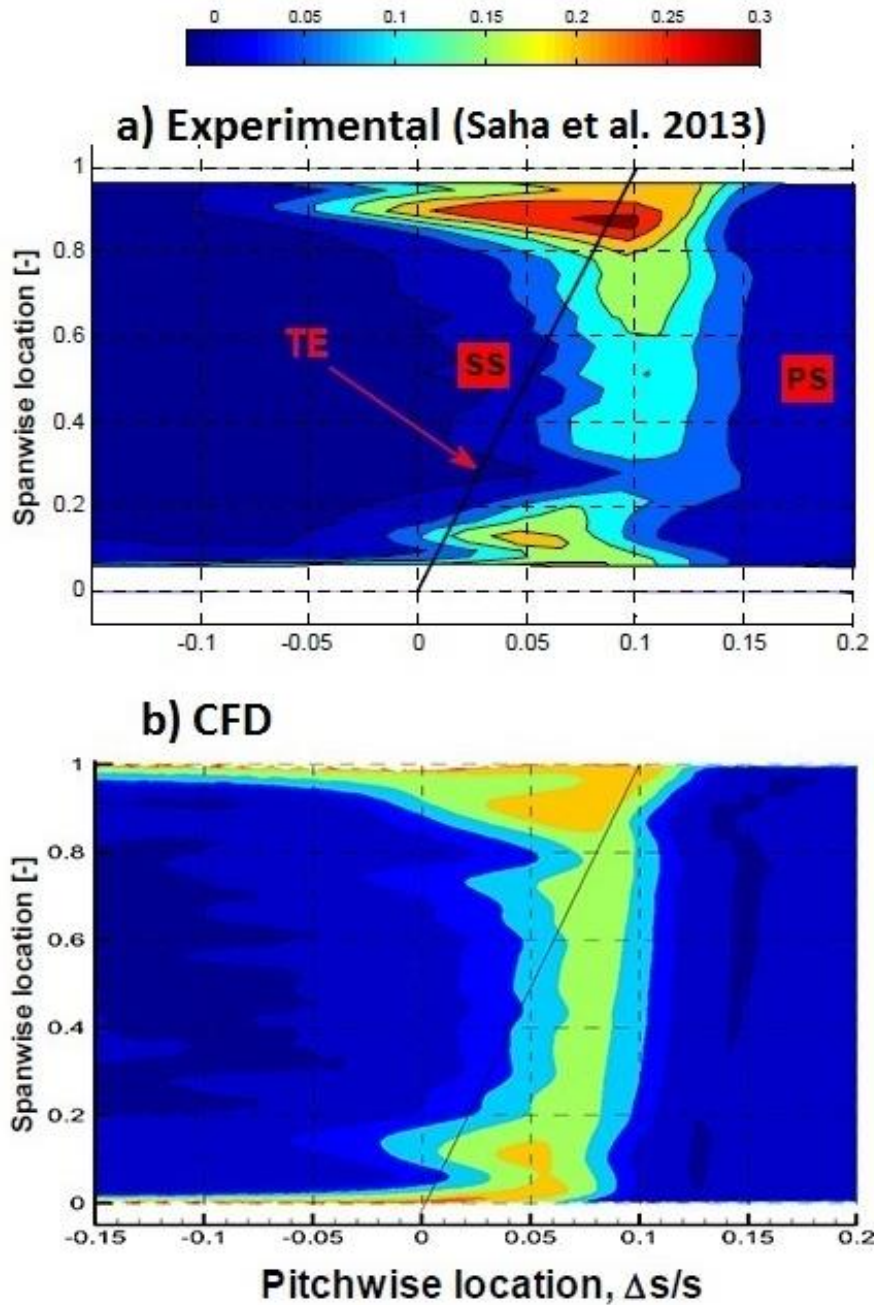


Figure 4-24 Total pressure distribution, SS1 Y_{high} case

Contours of the total pressure coefficient at 107.1% $C_{ax,hub}$ for SS1 high BR cases comparing experimental and CFD results is shown in Figure 4-24. The uncooled case has the highest C_p values near the endwalls and the wake of the TE. The same goes for the SS1 high BR case, however, a strong decrease at 28% span location is noted influenced by the counter rotating vortex mentioned before. The CFD is showing similar interruption but at much less value and

also under predicting the loss at endwalls. This might be caused by under estimation of mixedness of coolant flow with mainstream. Hypothetically, an unmixed coolant flow would increase the total pressure of the mainstream flow leading to decrease in the C_p loss and maybe even gain in total pressure (negative loss) in some extreme cases. Hence another measure of the loss that is formulated with the account for coolant flow is used in the next section to assess aerodynamic loss.

4.3.1.3. Aerodynamic loss

The KE loss coefficient used in section 4.1.1 is used here and a new one with some modifications is introduced. The previous definition will be referred to here as primary (subscript pr) while the new proposed coefficient will be pointed out as just ζ and is defined as:

$$\zeta = 1 - \frac{\text{Actual Exit K.E.}}{\text{Isentropic K.E. of mainstream} + \text{Isentropic KE of coolant}}$$

This translates into:

$$\zeta = 1 - \frac{(1+Y) \times \left[1 - \left(\frac{P_{2s}}{P_2} \right)^{\frac{k-1}{k}} \right]}{\left[1 - \left(\frac{P_{2s}}{P_1} \right)^{\frac{k-1}{k}} \right] + Y \times \left[1 - \left(\frac{P_{2s}}{P_c} \right)^{\frac{k-1}{k}} \right]} \quad \text{Eq. 4-12}$$

Figure 4-25 (a) is the value for the mass normalized mass averaged primary loss for all the cases at nominal BR (on the horizontal axis) plotted against normalized span location (the vertical axis). The primary loss is averaged with the loss between 40-60% of the reference case. Analogous to the exit flow angle, KE loss shows only a small variation from the reference case –if any-. In Figure 4-25 (b) though, SS1 high BR have strong local variation at 28% span, corresponding to the previously observed vortex at the location. The CFD results show the correct trends and reasonable values for all the cases. With the same previous observation of the deviation at the casing, and the author believe it is due to the same reason.

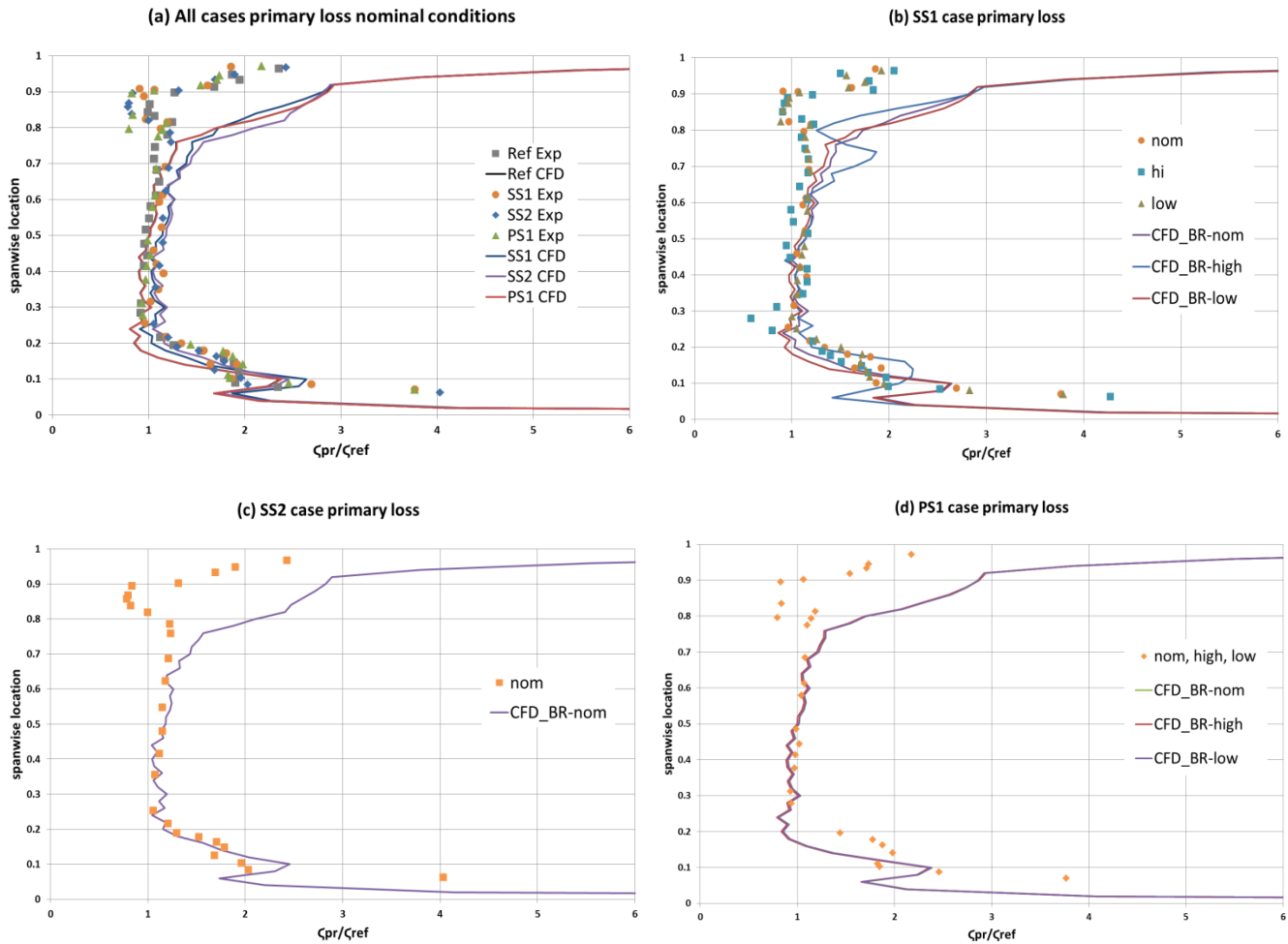


Figure 4-25 Normalized reference primary loss, different cooled cases (Experimental data from Saha et al. 2013)

The normalized KE loss in Figure 4-26 has the same trend of the primary loss, and the CFD simulation is showing agreement with the experimental measurements for all the cases (again, except for the casing endwall region). The suction side cooling is showing more loss penalty than the pressure side cooling (Figure 4-26 (a)). Also the effect of increasing BR on the loss is clearer in the SS1 case (Figure 4-26 (b)). Its significance increase for that case –more than PS1 case for instance- probably due to the higher mass flux ratio. This highlights the fact that the role played on the aerodynamic loss by film cooling parameters is not exclusive to BR, but also Y plays a role.

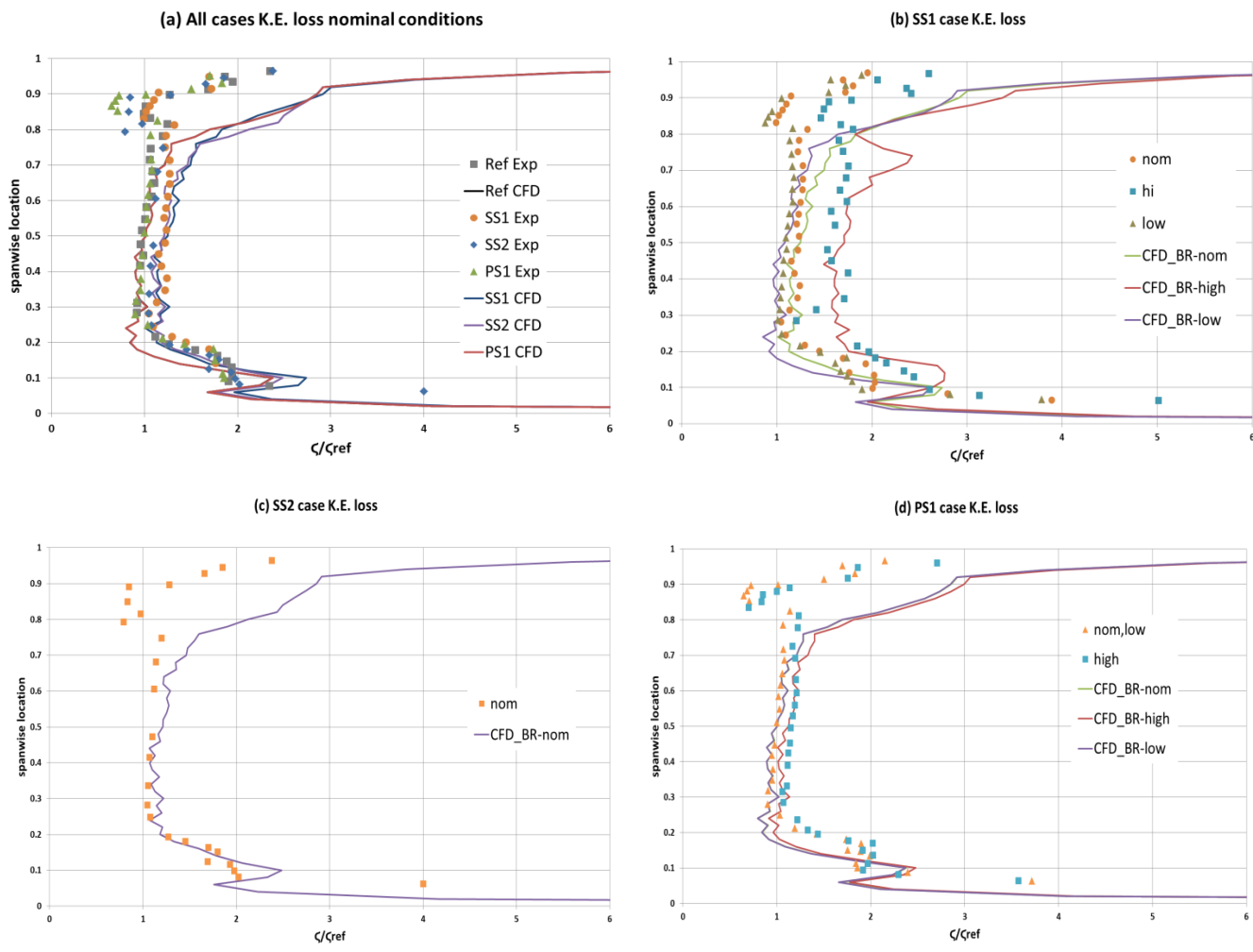


Figure 4-26 Normalized KE loss, different cooled cases (Experimental data from Saha et al. 2013)

4.3.2. Configuration 2 (Showerhead)

Leading edge is the part subjected to highest thermal loads caused by highest heat transfer coefficients as an effect of the stagnant flow on it. Hence, sufficient cooling is required at the LE to account for this higher than usual thermal loads. Showerhead cooling is achieved by introducing closely positioned rows of cooling holes. This close arrangement of the holes is expected to cause more interaction between different holes flow and tends to show more influence on the mainstream flow than suction and pressure side cooling.

The shape of the surface where the coolant is being injected plays a significant role on the film cooling performance. For instance, in case of injection on a convex surface (such as the leading edge), if the jet has less momentum than the mainstream, its radius of curvature would be less than that of the surface, which is translated into the jet is being pushed towards the surface improving η . And the opposite is true, if the momentum of the injected flow is higher than that of the mainstream, the injected flow would have larger radius of curvature detaching it from the surface and resulting in less η .

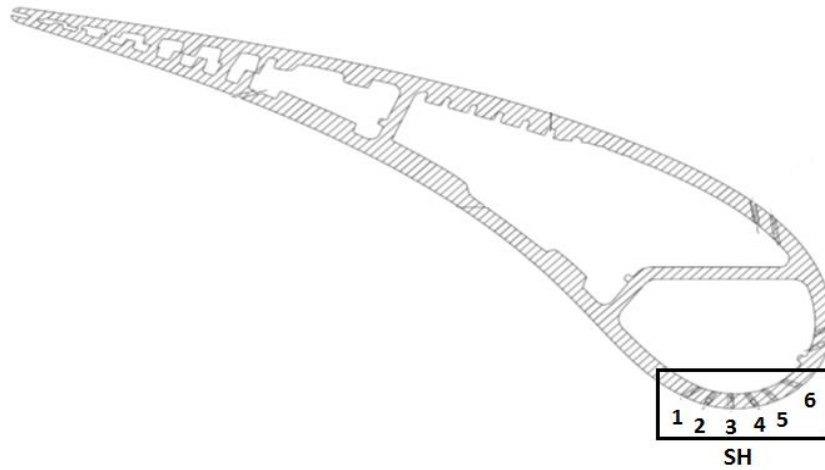


Figure 4-27 Showerhead cooling locations

Showerhead film cooling was analyzed for two different BR in this section. Figure 4-27 shows the location and arrangement of the 6 rows of coolant holes and Table 4-3 shows the correspondent geometrical features. Again the hole angles were measured from a tangent to the surface at hole exit.

Table 4-3 Showerhead cooling holes geometrical features

Row	x/cax	Angle [°]	No. of holes
SH1	3.30%	123.3	26
SH2	0.89%	105.4	25
SH3	0%	80.4	26
SH4	0.77%	66.9	26
SH5	3.40%	53	25
SH6	9.10%	46.33	11

Two runs were made, one at low Y and one at high Y according to Table 4-4. As expected, the BR varied for each row at the same Y because, this is due to the fact that the mainstream velocity is different at local locations of rows. For instance, for Y_{nom} row1 has BR = 5.84, while row2 has BR = 8.42. A change of 44% for the row in its vicinity, highlighting the severe change of flow conditions around the cylindrical blunt body the LE represents for the flow. The rest of the BR values for different rows are as follows: row3 = 4.4, row4 = 3.05, row5 = 2.3 and row6 = 1.98.

Table 4-4 Showerhead cooling flow conditions

Mass-flux ratio (Y)	Pressure ratio (P_m/P_c)
$Y_{nom} = 1.88\%$	0.93
$Y_{high} = 2.35\%$	0.89

The CFD calculations are compared to experimental measurements from Saha et al. (2014)

4.3.2.1. Exit flow angle distribution

The exit flow angle for SH cooled vane for the two BR is shown in Figure 4-28. The same behavior noted before of strong deviation of the flow direction occurs in the endwalls regions. Another important note is that in face applying cooling virtually didn't change the exit flow angle for any of the investigated cases (PS1, SS1, SS2 and LE) and at any BR. This is due to the minor effect of film cooling application on the big bulk of the flow, i.e. the low mass-flux of the coolant compared to the mainstream merely promulgate any change in the flow direction compared to for instance the noted severe deviation caused by endwall flow in the endwalls regions.

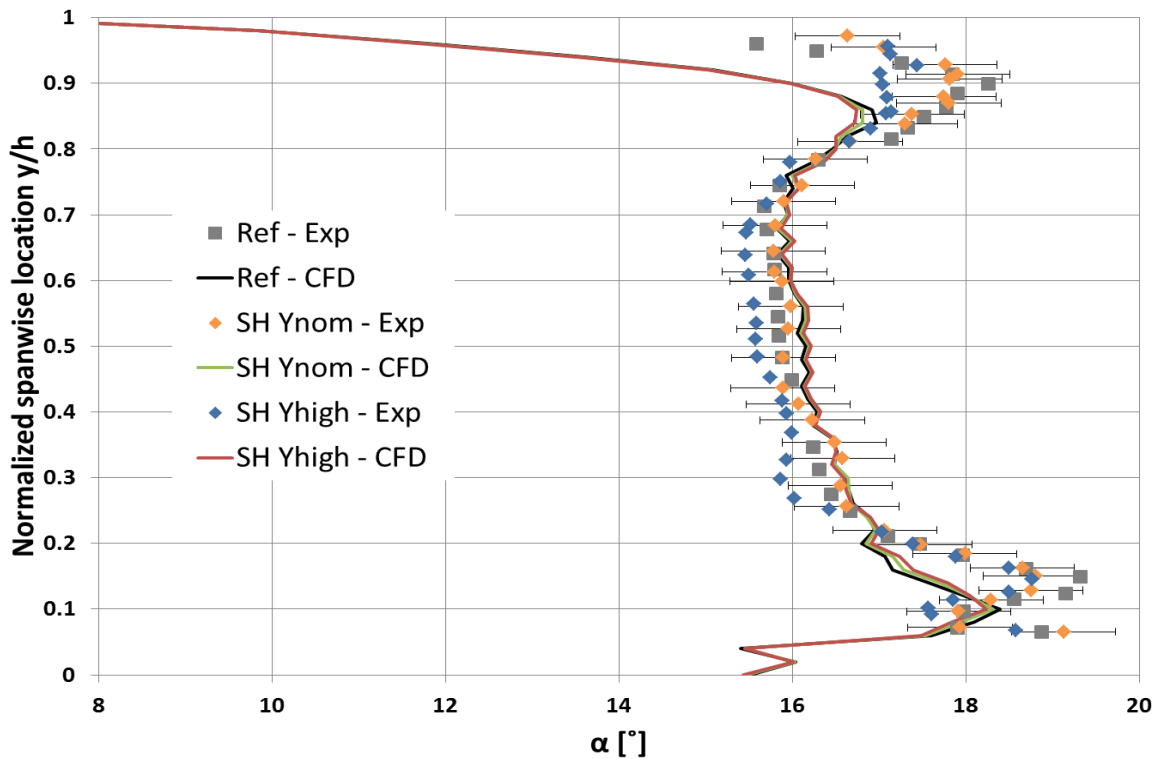


Figure 4-28 α for SH cooling at various Y, 107.1% $C_{ax, hub}$ (Experimental data from Saha et al. 2014)

4.3.2.2. Vorticity and total pressure distribution

A new definition of the total pressure coefficient (C_p) was used at this stage of the analysis, that is:

$$C_p = \frac{P_2}{P_{1,mid}} \quad \text{Eq. 4-13}$$

The total pressure downstream of the vane for the SH cooled case (Figure 4-30) looks fairly similar to the uncooled case (Figure 4-29). This supports what was previously mentioned about the total pressure coefficient probability of being a deciding parameter for loss assessment.

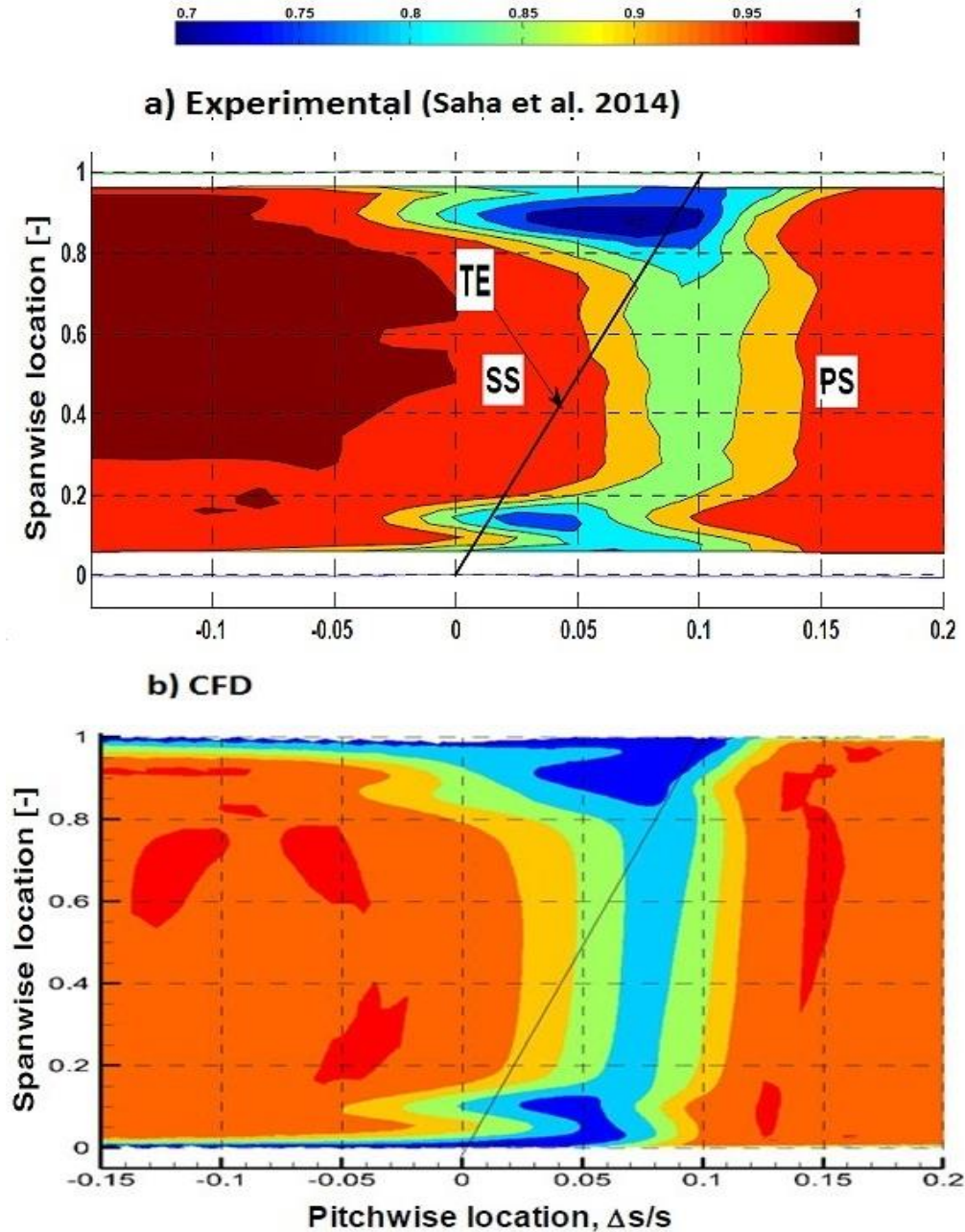


Figure 4-29 Total pressure coefficient reference case, 107.1% $C_{ax,hub}$

The unmixedness of coolant in CFD simulation is clear in this case as well. The casing endwall region is showing much less loss in total pressure, as the unmixed coolant flow doesn't impose a penalty on the total pressure and hence less drop than what's actually occurring can be seen in it.

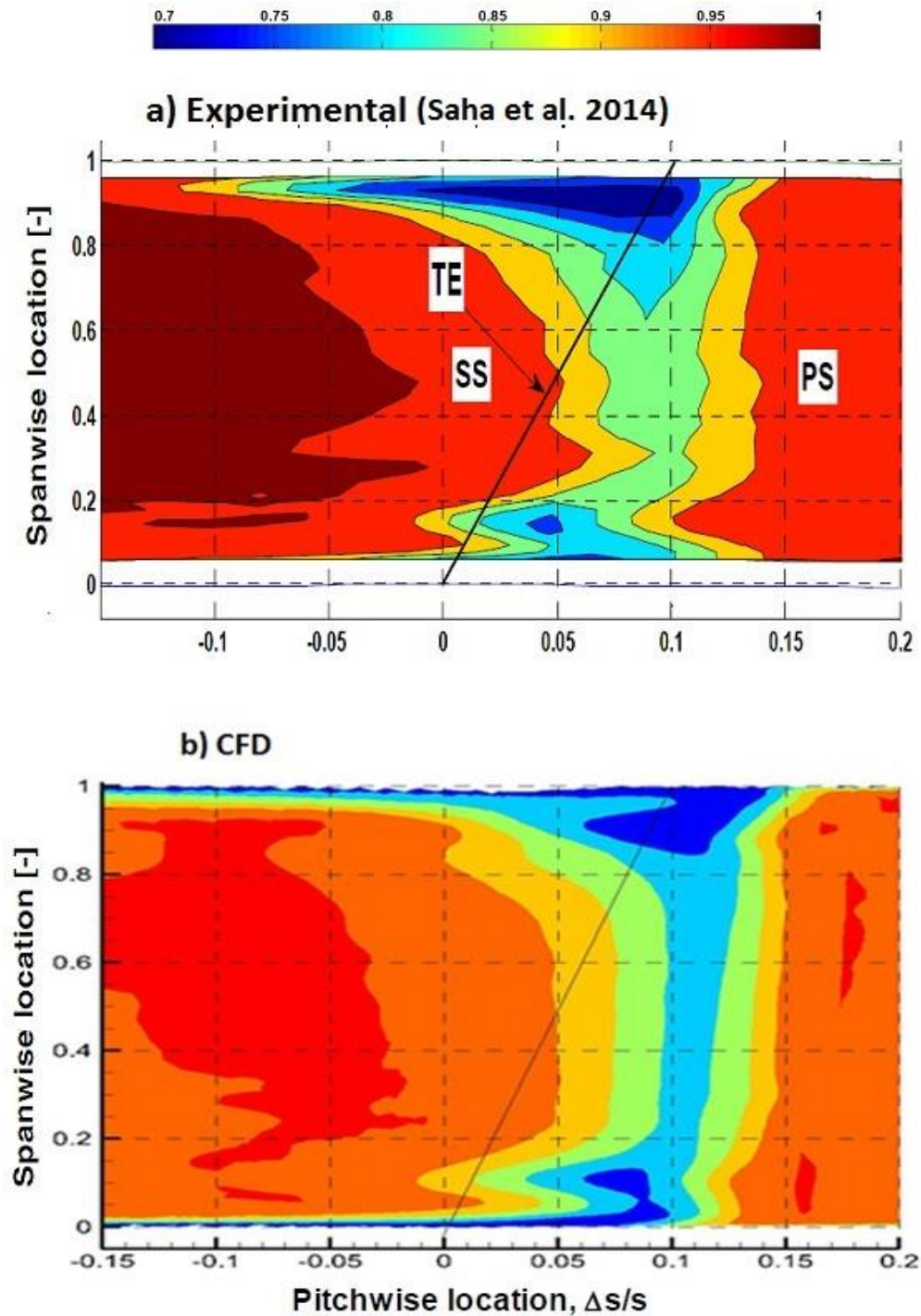


Figure 4-30 Total pressure coefficient SH cooled case Y_{high} , 107.1% $C_{ax,hub}$

The vorticity downstream of the vane for the SH cooled case at Y_{high} is shown in Figure 4-31 and an interruption of the TE shed vortex can be seen around 30% spanwise location, caused by film cooling injection unlike the reference case (Figure 4-4) where the shed vortex is continuous throughout the span.

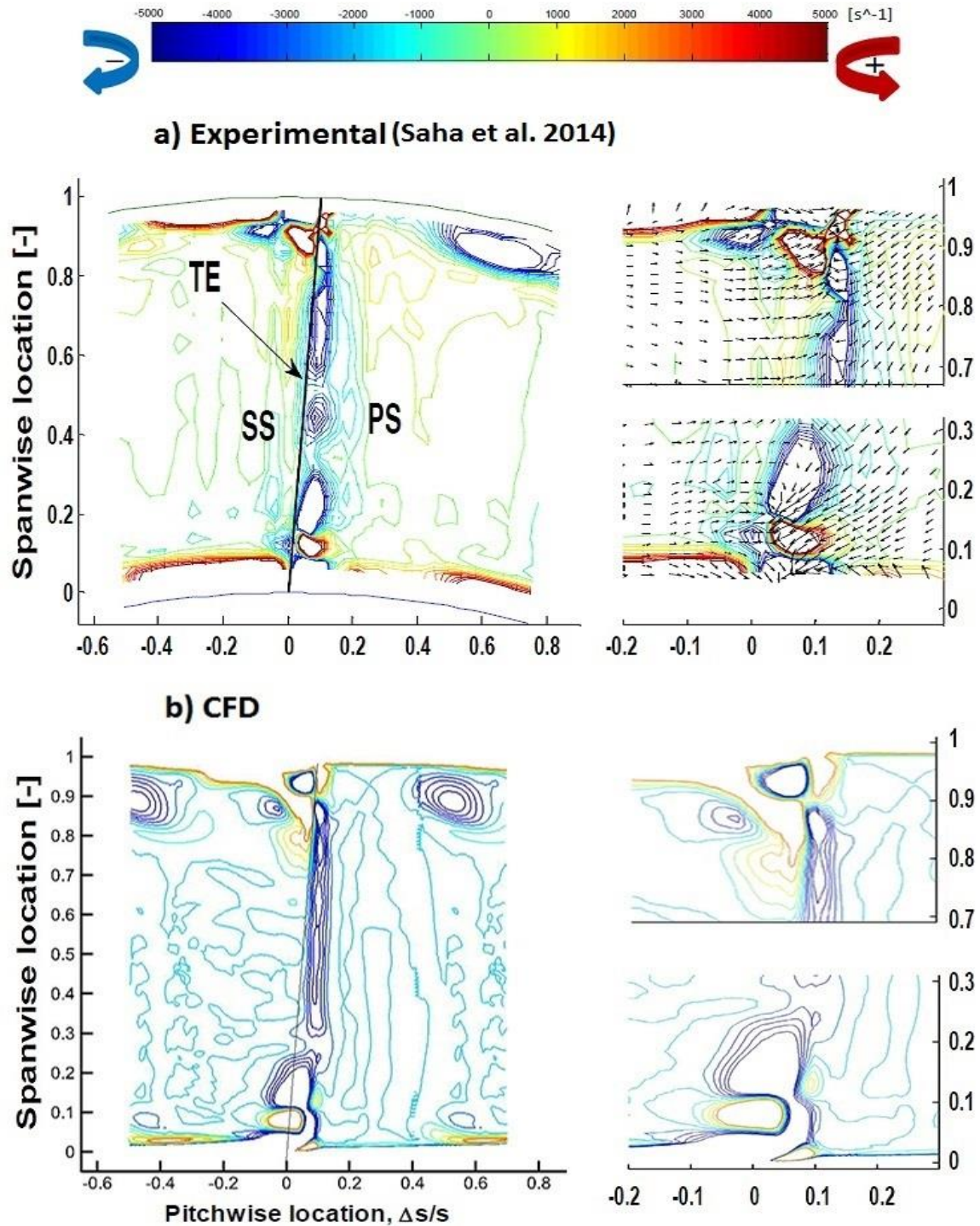


Figure 4-31 Vorticity at TE for SH cooled case at Y_{high}

The mentioned interruption can be traced all the way to its origin (coolant injected) in Figure 4-32. The origing and propagation of a clockwise rotating vortex can be seen in the black circles.

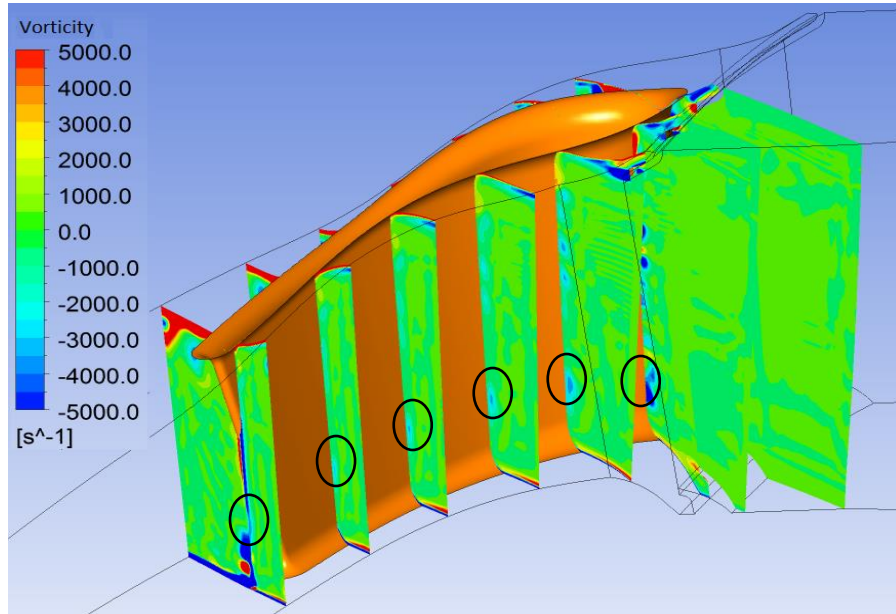


Figure 4-32 Showerhead Y_{high} PS vortex structure

Figure 4-33 shows similar formation of vortices of alternating sense of rotation, however, it mixes with the mainstream very fast and decay, leaving no trace in the flow domain downstream.

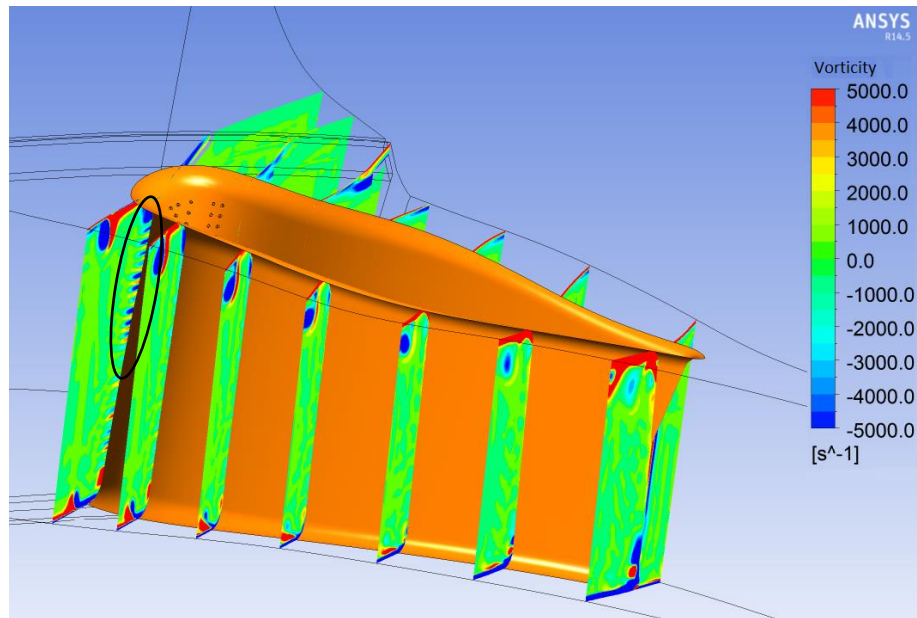


Figure 4-33 Showerhead Y_{high} SS vortex structure

4.3.2.3. Aerodynamic loss

In the primary loss measured (Figure 4-34), the effect of film cooling injection is fairly small, mainly due to the definition of the primary loss that doesn't account for the coolant injection.

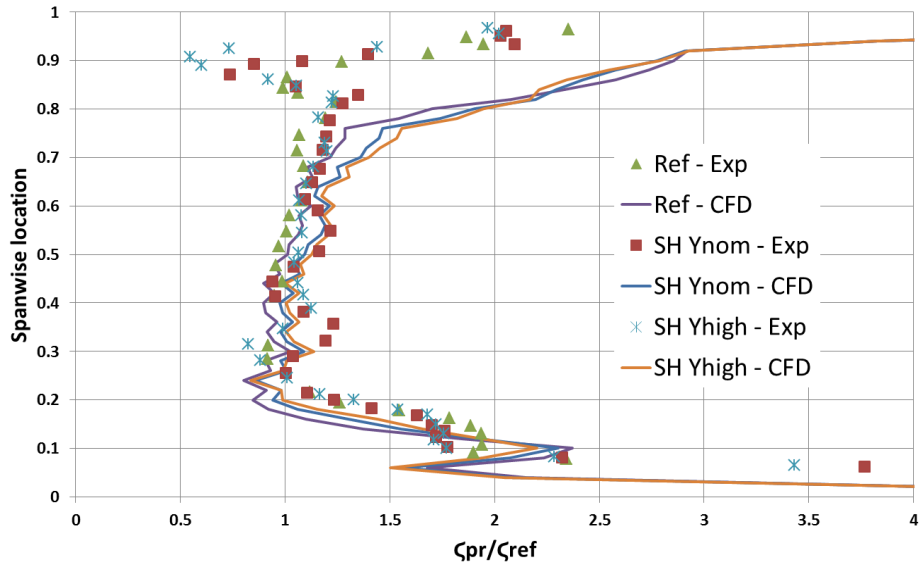


Figure 4-34 Normalized ζ_{pr} for SH cooling at various Y, 107.1% $C_{ax,hub}$ (Experimental data from Saha et al. 2014)

While a rise in the KE loss was promoted by SH film cooling for both BR investigated. Figure 4-34 shows an increase of about 25% in the loss. The KE loss in the plot is normalized by the KE loss of the reference case between 40-60% spanwise location. The higher Y case has more influence on the loss than the lower Y case as one would expect.

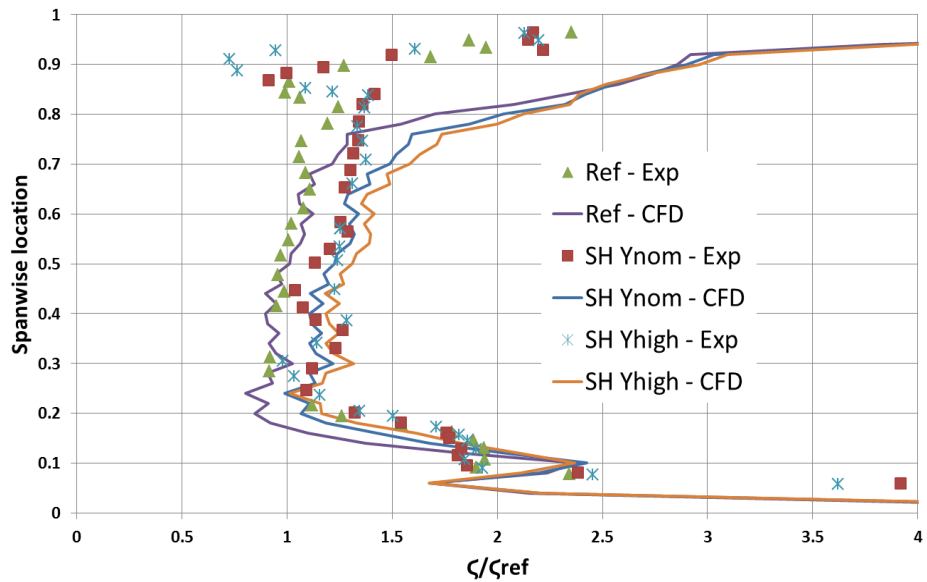


Figure 4-35 Normalized ζ for SH cooling at various Y, 107.1% $C_{ax,hub}$ (Experimental data from Saha et al. 2014)

5. Conclusion and future work

A CFD analysis of an annular sector cascade at an isentropic Mach number of 0.89 was carried out using ANSYS CFX solver. Preliminary, the simulation was performed on an uncooled vane. The CFD simulation was able to capture key features of the flow in the vane passage compared to experimental measurements, namely, exit flow angle, vortex formation, total pressure distribution and aerodynamic loss. Then a study case for film cooling was conducted on a flat plate and a new approach of introducing the coolant into the domain was used, eliminating the need to geometrically model the physical coolant plenum and tube. In this approach, the coolant is applied as boundary condition at the hole location directly at the surface. CFD results were compared to experimental measurements; the simulation obtained the correct trends of the centerline film cooling effectiveness and was able to predict flow field velocities and temperatures with considerable success for both approaches (full domain and coolant tube removed domain). The new approach was then implemented into the vane to mimic several film cooled vane experimental cases. Coolant was introduced at suction side, pressure side and showerhead cooling holes at different blowing ratios. Comparisons are made for the same flow features as the uncooled case: exit flow angle, vorticity, total pressure distribution and aerodynamic loss. The new approach showed results comparable to experimental measurements for most conditions.

The new approach was found to achieve 20% reduction in grid size in the flat plate –single hole- film cooling and when implemented for the cooled vane cascade, it kept the grid size almost equal to the uncooled vane (2.4 million nodes) versus a grid size of 6.8 million nodes when the coolant holes were modeled discretely (180% saving in grid size), resulting in saving of 300% in computing time (when run on a 16GB RAM, 6MB cache Intel i7 core® processor computer).

A recommendation for the next steps is to carry out heat transfer experiments for the cooled vane, using different temperatures for the mainstream and the coolant to study the thermal performance as well as the aero. This will help conclude on the validity of the new approach of film cooling application in film cooling design in real engines. Additional data on the surface of the vane would also be a useful next step in order to compare adiabatic film effectiveness and heat transfer coefficient resulting from the film cooling.

Appendices

Appendix A

SST turbulence model

In CFD analysis, and for turbulent flows, turbulent is modeled rather than solved, i.e. due to the very complicated flow features of turbulence, caused by its spatial and time variation. It is not feasible to actually solve for turbulence. The turbulence model used for numerical simulation throughout this work is Menter (1994) SST model. It is a modification of Wilcox (1988) k- ω model.

The model implements a blending factor (F) to calculate constants based on k- ω and k- ϵ models, the new constants are calculated as:

$$\varphi = F_1\varphi_1 + (1 - F_1)\varphi_2$$

Where

φ_1 is any constant in the k- ω model

φ_2 is any constant in the k- ϵ model

And φ is the constant in the new modified model

The blended constants are

$$\sigma_{k1} = 0.85, \sigma_{\omega1} = 0.5, \beta_1 = 0.075, \alpha_1 = 0.31$$

$$\beta^* = 0.09, k = 0.41, \gamma_1 = \beta_1/\beta^* - \sigma_{\omega1}k^2/\sqrt{\beta^*}$$

Where

$$\gamma_t = \frac{\alpha_1 k}{\max(\alpha_a \omega \Omega F_2)}$$

Ω is the absolute value of the vorticity, $F_2 = \tanh(\arg_2^2)$

$$\arg_2 = \max\left(2 \frac{\sqrt{k}}{0.09\omega y}; \frac{500\nu}{y^2\omega}\right)$$

Bibliography

Andreini, A., Da Soghe, R., Facchini, B., Mazzei, L., Colantuoni, S. and Turrini, F. "LOCAL SOURCE BASED CFD MODELING OF EFFUSION COOLING HOLES:." ASME Turbo Expo. San Antonio, Texas, USA, 2013. GT2013-94874.

Andreopoulos, J. and Rodi, W. "Experimental Investigation of Jets in a Crossflow." *Journal of Fluid Mechanics*, 1984: vol.138, pp. 93-127.

ANSYS 1, Release 13.0. "ANSYS CFX Technical Specifications." 2010

ANSYS 1, Version 12.1. "CFX-Solver Modeling Guide." 2009

Bartl, J. *Loss Measurements and Endwall Flow Investigations on an Annular Sector Cascade*. Study Project Work, Stockholm, Sweden: Department of Energy Technology, Division of Heat and Power Technology, KTH, 2010.

Blair, M. F. "An Experimental Study of Heat Transfer and Film Cooling on Large-Scale Turbine Endwalls." *ASME Journal of Heat Transfer*, 1974: 524-529.

Bohn, Dieter E. and Kusterer, Karsten A., "Aerothermal Investigations of Mixing Flow Phenomena in Case of Radially Inclined Ejection Holes at the Leading Edge." *Journal of Turbomachinery*, 1999: 122(2), 334-339.

Boyce, Meherwan P. *Gas Turbine Engineering Handbook, 2nd Edition*. Gulf Professional Publishing, 2001.

Day, C. R. B., Oldfield, M. L. G. and Lock, G. D. "The Influence of Film Cooling on the Efficiency of an Annular Nozzle Guide Vane Cascade." *Journal of Turbomachinery*, 1999: 121(1), 145-151.

Denton, J. D. "Loss Mechanisms in Turbomachines." *ASME Journal of Turbomachinery*, 1993: Vol. 115(4):621-656.

Eckerle, Wayne Alan. *Horseshoe Vortex Formation around A Cylinder*. University of Connecticut, 1985.

El-Gabry, Lamyaa A., Thurman, Douglas R., Poinsette, Philip E. and Heidmann, James D. "Turbulence and Heat Transfer Measurements in an Inclined Large Scale Film Cooling Array – Part I, Velocity and Turbulence Measurements." *ASME Turbo Expo*. 2011.

El-Gabry, L., Saha, R., Fridh, J. and Fransson, T. "Measurements Of Hub Flow Interaction On Film Cooled Nozzle Guide Vane In Transonic Annular Cascade." *ASME Turbo Expo*. 2012.

Fearn, R.L. and Weston, R.P. "Vorticity Associated with a Jet in a Cross Flow." *AIAA Journal*, 1974: vol. 12, No. 12, pp. 1666-1671.

- Fric, T.F. "Structure in the Near Field of the Transverse Jet." CalTech, 1990.
- Gafurov, Tokhir. *Numerical Calculation and Validation of an Annular Sector Cascade for Experimental Aerodynamic Testing*. MSc Thesis, Stockholm, Sweden: KTH Royal Institute of Technology, 2008.
- Garg, Vijay K. and Rigby, David L. "Heat transfer on a film-cooled blade - effect of hole physics." *International Journal of Heat and Fluid Flow*, 1999: 10-25.
- Giampaolo, Anthony. *Gas turbine handbook principles and practices*. Lilburn, GA: The Fairmont Press, Inc., 2006.
- Gregory-Smith, D. G., and Graves, C. P. *Secondary Flows and Losses in a Turbine Cascade*. DURHAM UNIV (England) DEPT OF ENGINEERING., 1983.
- Gritsch, M., Schulz, A., and Wittig, S. "Adiabatic Wall Effectiveness Measurements of Film-Cooling Holes with Expanded Exits." *Journal of Turbomachinery*, 1998: Vol. 120, pp. 549–556.
- Heidmann, J. D., and Hunter, S.D. *Coarse Grid Modeling of Turbine Film Cooling Flows Using Volumetric Source Terms*. Cleveland, Ohio: National Aeronautics and Space Administration, Glenn Research Center, 2001.
- Hildebrandt, Th., Ettrich, J., Kluge, M., Swoboda, M., Keskin, A., Haselbach, F. and Schiffer, H.P. "UNSTEADY 3D NAVIER-STOKES CALCULATION OF A FILM-COOLED TURBINE STAGE WITH DISCRETE COOLING HOLE." In *UNSTEADY AERODYNAMICS, AEROACOUSTICS AND AEROELASTICITY OF TURBOMACHINES*, pp 533-549. Springer Netherlands, 2006.
- Hill, P. and Peterson, C. *Mechanics and Thermodynamics of Propulsion, Second Edition*. Addison-Wesley Publishing, 1992.
- Klein, A. *Untersuchungen iiber den Einfluss der Zustrb'm-grenzschicht auf die Sekundarstrb'mung in den Beschau felungen von Axialturbinen (English translation: Investigation of the Entry Boundary Layer on the Secondary Flows in the Blading of Axial Turbines)*. British Hydromechanics Research Association, 1966.
- Lalzel,Gildas, Sultan, Qaiser, Fenot, Matthieu and Dorignac, Eva, "Experimental convective heat transfer characterization of pulsating jet in cross flow: in influence of Strouhal number excitation on film cooling effectiveness." *6th European Thermal Sciences Conference (Eurotherm 2012)*. Journal of Physics: Conference Series 395, 2012.
- Langston, L. S. "Crossflows in a Turbine Cascade Passage." *ASME Journal of Eng. For Power*, 1980: Vol. 102: 866–874.
- Langston, L.S. "Secondary Flows in Axial Turbines—A Review." *Annals of the New York Academy of Sciences*, 2001.

- Langston, L. S., Hooper, R. M. and Nice, M. L. "Three-Dimensional Flow within a Turbine Cascade Passage." *ASME Journal of Engineering for Power*, 1977: Vol. 99:21-28.
- Law, C.K., Makino, A. Lu, T.F. "On the off-stoichiometric peaking of adiabatic flame temperature." *Combustion and Flame*, June 2006: 808-819.
- Mahmood, G. I., Gustafson, R. and Acharya, S. "Experimental Investigation of Flow Structure and Nusselt Number in a Low-Speed Linear Blade Passage With and Without Leading-Edge Fillets." *J. Heat Transfer (J. Heat Transfer.)* 127, no. 5 (2005): 127(5):499-512.
- Mamaev, B. I. Internal Communication, Siemens LLC Energy Oil & Gas Design Department, 2011.
- Marchal, P., and Sieverding, C. H. "Secondary Flows Within Turbomachinery Bladings." *AGARD CP 214*. 1977.
- Marek, Cecil J. and Tacina, Robert R. "Effect of Free-Stream Turbulence on Film Cooling." *Journal of Turbomachinery*, 2003: 125(1), 65-73.
- Menter, F. R. "Two-Equation Eddy-Viscosity Turbulence Models for Engineering Applications." *AIAA Journal*, 1994: pp. 1598-1605.
- Menter, F. R., Kuntz, M. and Langtry, R. *Ten Years of Industrial Experience with the SST Turbulence model*. Begell House, Inc., 2003.
- Mitrus, A., "Numerical Investigation of Blade Leading Edge Contouring By Fillet and Baseline Case of a Turbine Vane - A Comparative Study of the Effect on Secondary Flow", M.Sc. Thesis EGI-2012-045MSC EKV894, Division of Heat and Power Technology, KTH, 2012.
- Moore, J., and Smith, B. L. "Flow in a Turbine Cascade. Part 2: Measurement of Flow Trajectories by Ethylene Detection." *J. Eng. Gas Turbines Power (ASME)*, 1984: 409-413.
- Moussa, Z. M., Trischka, J.W. and Eskinazi, S. "The Near Field in the Mixing of a Round Jet with a Cross-Stream." *Journal of Fluid Mechanics*, 1977: vol. 80, pp. 49-80.
- Nicklas, Martin. "Film-Cooled Turbine Endwall in a Transonic Flow Field - Part II-Heat Transfer and Film Cooling Effectiveness." *Journal of Turbomachinery*, 2001: 123(4), 720-729.
- Nicklas, Martin and Kost, Friedrich. "Film-Cooled Turbine Endwall in a Transonic Flow Field - Part I-Aerodynamic Measurements." *Journal of Turbomachinery*, 2001: 123(4), 709-719.
- Povey, T., Jones, T.V., Oldfield, M.L.G., "On a Novel Annular Sector Cascade Technique", *Journal of Turbomachinery*, Vol.129, pp. 175-183, 2007.
- PwC Aerospace & defense report "2012 year in review and 2013 forecast"
- Roshko, T. F. and Fric, A. "Vortical structure in the wake of a transverse jet." *Journal of Fluid Mechanics*, 1994: 279, pp 1-47.

- Roux, J. *Experimental Investigation of Nozzle guide Vanes in a Sector of an Annular Cascade*. Licentiate Thesis, Stockholm, Sweden: TRITA KRV 2004-3, ISSN 1100-7990, ISRN KTH-KRV-R-04-3-SE, ISBN 91-7283-672-5, 2004.
- Saha, R. "Aerodynamic Investigations of a High Pressure Turbine Vane with Leading Edge Contouring at Endwall in a Transonic Annular Sector Cascade." Licentiate Thesis, Division of Heat and Power Technology, KTH, ISBN 978-91-7501-293-3, 2012.
- Saha, R., Fridh, J., Fransson, T., Mamaev, B. I. and Annerfeldt, M., "SUCTION AND PRESSURE SIDE FILM COOLING INFLUENCE ON VANE AERO PERFORMANCE IN A TRANSONIC ANNULAR CASCADE", ASME Turbo Expo 2013. Paper No. GT2013-94319.
- Saha, R., Fridh, J., Fransson, T., Mamaev, B. I., Annerfeldt, M. and Utriainen, E. "SHOWER HEAD AND TRAILING EDGE COOLING INFLUENCE ON TRANSONIC VANE AERO PERFORMANCE", ASME Turbo Expo 2014. Paper No. GT2014-25613 (draft paper accepted).
- Schlichting, H. *Boundary-layer theory*. New York: McGraw-Hill, 1955.
- Scorer, R. S. *Natural Aerodynamics*. Pergamon Press, 1958.
- Shalash, K.M., El-Gabry, L.A., and Abo El-Azm, M.M. "Numerical Modeling Of Slot Film Cooling Using A Wall Function." *ASME paper GT2013-94127*. San Antonio: ASME Turbo Expo, 2013.
- Sharma, O.P. and Butler, T.L. "Predictions of Endwall Losses and Secondary Flows in Axial Flow Turbine Cascades." *ASME Journal of Turbomachinery*, 1987: Vol. 109: 229-236.
- Sieverding, C. H. "Recent Progress in the Understanding of Basic Aspects of Secondary Flows in Turbine Blade Passages." *ASME Journal of Turbomachinery*, 1985: Vol. 107: 248-257.
- Sieverding, C. H. and van den Bosche, P. "The use of coloured smoke to visualize secondary flows in a turbine-blade cascade." *Journal of Turbomachinery*, 1983: Vol. 134: 85-89.
- Sugiyama, Y. "A Calculation of Penetration of the Jet Issuing Normally into a Cross Flow Across a Wall Boundary Layer." *International Pacific Air and Space Technology Conference and 29th Aircraft Symposium*. Gifu, Japan: SAE Technical Paper Series 912029, 1991.
- Sugiyama, Y. "Pressure Distribution on and Around an Exit Plane of a Jet Normal to a Cross-Flow." *International Gas Turbine Congress*. Yokohama, Japan, 1995. vol. 11:375-382.
- Sykes, R.I., Lewellen, W.S., and Parker, S.F. "On the Vorticity Dynamics of a Turbulent Jet in a Crossflow." *Journal of Fluid Mechanics*, 1986: vol. 168, pp. 393-413.
- Takeishi, K., Matsuura, M., Aoki, S. and Sato, T. "An Experimental Study of Heat Transfer and Film Cooling on Low Aspect Ratio Turbine Nozzles." *Journal of Turbomachinery*, 1990: 112(3), 488-496.

- Thole, D. G. and Bogard, K. A. "Gas Turbine Film Cooling." *Journal of Propulsion and Power*, 2006: Vol. 22, No. 2, pp. 249-270.
- Thurman, Douglas R., El-Gabry, Lamyaa A., Poinsatte, Philip E. and Heidmann, James D. "Turbulence and Heat Transfer Measurements in an Inclined Large Scale Film Cooling Array – Part II, Temperature and Heat Transfer Measurements" *ASME Turbo Expo*. 2011.
- Wiclox, D.C. "Reassessment of the Scale-Determining Equation for Advanced Turbulence Models." *AIAA Journal*, Vol. 26, No. 11, 1988: 1299-1310.